ADDIS ABABA SCIENCE AND TECHNOLOGY UNIVERSITY

ASSESSMENT OF POST-FIRE PERFORMANCE OF GFRP STAY IN PLACE FORMWORK FOR CONCRETE BRIDGE DECKS

A MASTER'S THESIS

By

BODENA SIRNA NEGEO

DEPARTMENT OF CIVIL ENGINEERING

COLLEGE OF ARCHITECTURE AND CIVIL ENGINEERING

FEBRUARY 2022

ADDIS ABABA SCIENCE AND TECHNOLOGY UNIVERSITY

ASSESSMENT OF POST-FIRE PERFORMANCE OF GFRP STAY IN PLACE FORMWORK FOR CONCRETE BRIDGE DECKS

By

BODENA SIRNA NEGEO

A Thesis Submitted as a Partial Fulfillment for the Degree of Master of Science in Civil Engineering (Structural Engineering)

To

DEPARTMENT OF CIVIL ENGINEERING

COLLEGE OF ARCHITECTURE AND CIVIL ENGINEERING

FEBRUARY 2022

Declaration

Declaration

I hereby declare that this thesis entitled"**Assessment of Post Fire Performance of GFRP Stay in Place Formwork for Concrete Bridge Decks"** was prepared by me, with the guidance of my advisor. The work contained herein is my own except where explicitly stated otherwise in the text, and that this work has not been submitted, in whole or in part, for any other degree or professional qualification.

Author: Signature, Date:

Bodena Sirna Negeo 18/02/2022

Witnessed by:

Name of student advisor: Signature, Date:

Dr.Ing. Nigatu Chaffo 18/02/22

Approval page

APPROVAL PAGE

This is to certify that the thesis prepared by **Mr. Bodena Sirna Negeo** entitled **"Assessment of Post Fire Performance of GFRP stay in place formwork for Concrete Bridge Decks"** and submitted in fulfillment of the requirements for the Degree of Master of Science complies with the regulations of the University and meets the accepted standards with respect to originality and quality.

Singed by Examining Board

	Signature	Date
Advisor: Dr. Negeo C		18/02/22
External Examiner: Dr. Kabtamu Getachew		16/02/2022
Internal Examiner: Dr. Tesfaye Alemu		16/2/22
Chairperson: Simret T. (Ph.D.)		17/02/202
DGC Chairperson: Abeneyer T.		24/02/22
Collage Dean/Associate Dean for GP:		24/02/22

Dedication

I dedicate this Thesis to God almighty for granting me wisdom, knowledge, strength, and inspiration in my MSc program.

Abstract

In highway bridge building, concrete decks are widespread, forming the driving surface and serving as the superstructure of the bridge. Bridge decks are exposed to direct contact from traffic, humidity, and chlorides which are liable to corrosion. For this cause, in bridge construction, FRP stay-in-place (SIP) formwork has been suggested. However, when bridge fire occurs due to the collisions or crushing of the cars and burning of fuels in the proximity of the bridge the behavior of FRP at elevated temperatures is a major concern. Therefore, this study investigated numerically the post-fire performance of concrete bridge decks by simultaneous heating and loading. This sequence of structural loading is employed in three-dimensional (3-D) FEM with the program ABAQUS using a sequentially coupled thermal displacement analysis. The FEM is validated against an experimental test based on the load-deflection, cracking failure, and predicted temperature evolution. The FEM successfully agreed with the experimental result. Various parameters influencing the fire performance of a concrete bridge deck were investigated in this study. The findings indicate that aggregate types have little influence on the fire performance of concrete decks. The concrete deck subjected to 1-hour standard and hydrocarbon fire had a reduction of 13.9 and 17.7% of ultimate strength compared with the undamaged concrete deck while for 1hour and 2-hour standard fire had 15 and 19% respectively. The Effect of sustained load did not have an impact on predicted temperature but had a significant impact on concrete bridge deck deformation. The finite element analysis verifies an approximate linear scaling of the ultimate carrying capacity with the member width of the fire-damaged concrete bridge deck. The fire-damaged concrete deck strengthened reinstate up to 50.6% of ultimate strength by extending further the GFRP base plate to support. Finally bout 9.09 and 14.65 % of ultimate strength was enhanced by increasing GFRP base plate thickness from 10 to 20 mm compared with an undamaged concrete deck, and 3.56 and 21 % of ultimate load of the fire-damaged concrete bridge decks with cooling phase were enhanced compared with the control specimen C1 and without cooling phase respectively.

Keywords: Bridge deck, Concrete bridge deck, FRP stay-in-place formwork; Post-fire performance.

Acknowledgment

First, I would like to praise the almighty God, who is worthy to be praised for his grace and endless blessing. My deepest gratitude goes to my advisor Dr. Ing Nigatu Chaffo for his unreserved assistance, useful suggestions, and timely comments at all stages of my work, And Dr. Temsgen Wondimu for his assistance and encouragement overall pass of this research; particularly on software.

I would like to express my heartfelt appreciation to Dr. Tesfaye Alemu for this assistance and commenting starting from the selection of a title for this study to the final draft of the proposal and Dr. Kabtamu Getachew for sharing his crucial knowledge on the bridge engineering course.

I would like to express my gratitude to Addis Ababa Science and Technology University for accepting me to attend my degree of Master of Science in civil engineering (structural engineering) and Ambo University for sponsoring the tuition fees in collaboration with the minister of science and higher education.

Last but not least, I would like to thank my family and friends for their constructive opinions and support.

Bodena Sirna

February 2022

Table of content

List of tables

List of figures

Symbols and abbreviations

AASHTO	American Association of State Highway Officials
ASTM	American Standard Testing Material
ACI	American Concrete Institute
CFRP	Carbon Fiber Reinforced polymer
CSA	Canadian Standards Association
CDP	Concrete Damage Plasticity
EBCS	Ethiopian Building Code of Standard
ERA	Ethiopian Road Authority
EN	European Norm
FD	Fire Damaged beam
FE	Finite Element
FEM	Finite Element Model
GFRP	Glass Fiber Reinforced Polymer
IC	Intermediate Crack-induced
LITS	Load-Induced Thermal Straining Effects
RC	Reinforced Concrete
SIP	Stay in Place
Tg	Glass transition temperature
NSC	Normal Strength Concrete
NWC	Normal Weight Concrete
2D	Two dimensional
3D	Three dimensional
^{o}C	Degree of Celsius
Φ	Diameter
$\varrho_{c,\theta}$	The density of concrete at the specified temperature
λc	Thermal conductivity of concrete
C_c	Specific heat of concrete
ψ	Dilation angle
μ	Viscosity parameter
K_C	the shape factor of the yield surface
d_c	Damage variable in compression
d_t	Damage variable in tension
W_t	Tension stiffness recovery factor
W_c	Compression stiffness recovery factor
σ_{cu}	Ultimate stress
$f_{c'}$	Peak compressive strength of normal concrete
ε_t	Concrete tensile strain
ε_{cr}	Cracking strain of normal concrete
E1	Modulus of elasticity in x-direction
E2	Modulus of elasticity in y-direction
E3	Modulus of elasticity in z-direction
G12	Shear modulus in xy- direction
G13	Shear modulus in xz- direction
G23	Shear modulus in yz- direction
NU12	Poison’s ratio in xy-direction
NU13	Poison’s ratio in xz-direction
NU23	Poison’s ratio in yz-direction

CHAPTER ONE
INTRODUCTION

1.1 Background of the study

In highway bridge building, concrete decks are widespread, forming the driving surface and often sometimes serving as a structural part of the superstructure of the bridge. Bridge decks are exposed to direct contact from traffic, humidity, and sometimes chlorides, rendering them more susceptible to corrosion and degradation than the rest of the bridge construction(M. Nelson & Fam, 2014). For this cause, in bridge construction, fiber-reinforced polymer (FRP) composites have been gaining acceptance and popularity. For concrete decks, FRP stay-in-place (SIP) formwork has been suggested due to it minimizing labor costs, reducing construction time, and function as bottom flexural reinforcement(M. Nelson & Fam, 2013; M. S. Nelson et al., 2014). However, still there is a limited implementation of FRP SIP forms. Bridge also exposed to fire when the collisions or crushing of the cars and burning of fuels in the proximity of the bridge which leads to permanent damage or collapse of the bridge, economic and public losses (Garlock et al., 2012). Bridge fire mostly damaged and made a harmful accident due to fire caused by tanker trucks those transport gasoline or flammable liquids, since fuel amounts transported in the tankers approximately 30-35 m^3. When the flames and hot gases come into direct contact with the structures high damage levels will occur as the fire in material stored under the bridge, tanker catches fire under or top of the bridge(Peris-Sayol et al., 2017). Therefore, bridge fires have become a problem.

However, most design codes cannot consider fire in bridge design, European code part 1-2 is only considered for building structures. Information on fire for building elements might not be directly applicable to bridge girders due to different fire scenarios, loading, boundary condition, failure limit states, and sectional properties that are present in bridges(Aziz & Kodur, 2013). There is also a limited study on fire performance of Glass fiber reinforced polymer stays in place formwork (SIP). Uncertainties on strength of GFRP reinforcing bars due to lack of knowledge on the assessment of the post-fire performance of GFRP at elevated temperatures(Hajiloo & Green, 2018b, 2018a). This study aims to fill an important gap regarding bridge decks with FRP SIP forms with T-shaped ribs protruding upwards, properly referred to as T-Up, particularly looking at their post-fire performance and the impact of sustained loading on their load-induced

thermal strain effects (LITS). In the current study, various variables that influence the fire performance of GFRP concrete bridge decks were further investigated.

1.2 Statement of the problems

Recently, the use of composite material such as Glass fiber reinforced polymers (GFRP) is one of the innovative materials in the use of stay in place (SIP) permanent formwork for concrete bridge decks and it has a high strength-to-weight ratio, resistance to corrosion, availability in a wide variety of shapes and sizes, and reduced construction time. The structural performance of the Glass Fiber Reinforced polymer stays in place formwork in concrete bridge decks has been studied in the Past by researchers and investigated its mode of failure, the effect of form splicing, behavioral mechanics, and impact of freeze-thaw cycles (Boles et al., 2015; M. Nelson & Fam, 2014). However, there is no large- or small-scale testing has been conducted to express structural performance and strengthening of fire-damaged GFRP stay in place formwork for concrete bridge decks. Concurrent heating and loading of concrete GFRP formwork systems for the identification of load-induced thermal strain effects (LITS) are identified as possible areas for future work(Nicoletta et al., 2019).

In many countries including Ethiopia where the GFRP is marketed, but no specific fire requirements in bridge design standards (ERA, Europe code part 2, and AASHTO/CSA) for GFRP stay in place formwork for concrete bridge decks. This is a well-presented issue that has been addressed by several researchers(Garlock et al., 2012; Peris-Sayol et al., 2017). Because of the above, further research was needed.

Therefore, this study numerically investigates to assess the post-fire performance of the Glass Fiber Reinforced Polymer stay in formwork for concrete bridge decks and further parametric studies on fire exposure time, fire types, sustained service loading (in addition to bridge deck self-weight), length of GFRP plate, the thickness of GFRP plate, aggregate types, span to depth ration, deck width, and cooling and heating phase.

1.3 The objective of the study

1.3.1 General objective

The main objective of this study is to investigate the post-fire performance of Glass Fiber Reinforced Polymer (GFRP) concrete bridge decks at elevated temperature by simultaneous heating and loading of concrete GFRP formwork systems.

1.3.2 Specific objective

- To determine the performance and behavior of GFRP materials under standard and hydrocarbon fire.
- To investigate the effect of sustained service loading during fire exposure on the thermal and load-deflection response of GFRP concrete bridge at the elevated temperature.
- To investigate the effect of sustained service loading on the post-fire flexural response of GFRP concrete bridge deck after cooling.
- To assess the effectiveness of the GFRP strengthening on the flexural response (the load-deflection relationships, GFRP strain deflection relationships, and failure mode) of GFRP strengthened fire-damaged GFRP concrete bridge deck.
- To perform parametric studies to determine the influence of various main parameters on fire resistance of concrete bridge decks.

1.4 Research questions

- How to study the performance and behavior of GFRP materials under standard and hydrocarbon fire?
- Can sustain service loading affects the performance of concrete bridge at elevated temperature?
- Can sustain loading affects the performance of concrete bridge after cooling?
- Are effective in strengthening flexural areas of fire-damaged GFRP concrete bridge decks by GFRP plate?
- How to perform parametric studies that affect the fire resistance of concrete bridge decks?

1.5 Significance of the study

In particular, the corrosion resistance and ease of fabrication make GFRP stay-in-place (SIP) formwork unique in bridge deck construction where harsh environmental conditions. Therefore, the result of this study helps the engineers in design provisions and recommendation on fire-damaged Glass Fiber Reinforced Polymer (GFRP) bridge decks and support the current Ethiopian, European, and American/Canadian Bridge design standards (ERA, Euro code 1 Part 2 and AASHTO/CSA) respectively in the development of standards and design provisions for fire-damaged Glass Fiber Reinforced Polymer (GFRP) bridge decks and the result of this study extended to (EBCS EN 1992-

1-1:2013, ACI 440.2R-17)guide for the design and construction of externally bonded GFRP Systems for strengthening fire-damaged RC structures. The results and conclusions are drawn recommend the Glass fiber reinforced polymer as fire-resistant material in concrete bridge decks for future structural engineering purposes.

1.6 Scope and Limitations of the study

Commercially available finite element software ABAQUS is used to perform an investigation on the post-fire performance of GFRP SIP formwork for concrete bridge decks. The limitation of the study is part of the literature review since there is a limited study on the performance of GFRP SIP formwork concrete bridge decks at elevated temperature and no code of standard that addresses the thermal and mechanical properties of GFRP at elevated temperature. The thermal and mechanical properties of GFRP at elevated temperature were extracted using data extractor software from previously conducted research for his study. Another limitation of the study is the selection of experimental programs for verifying the models for further parametric study. As there is no full-scale experimental study, small-scale testing which cannot fully represent bridge decks in existing structures, which are always subject to vehicular live loads and heavy sustained loads were selected.

1.7 Thesis layout

This thesis consists of five sections. The content of each section is described as follows.

Chapter one: presents the background of the study, statement of the problem, objective, significance of the study, scope, and limitations of the study.

Chapter two: concerned with a literature review of previous studies on fire performance of fiber-reinforced polymer at elevated temperature, as well as the constitutive material models of concrete and GFRP at elevated temperature.

Chapter three: deals with the methodology to be followed to reach the result and conclusion including a description of material and model geometry, a brief introduction to ABAQUS software, constitutive material model of concrete and GFRP at elevated temperature, mechanical and thermal contact at interfaces, element attributes, meshing, loading and boundary condition, the procedure of finite element analysis, types of analysis and calibration of finite element analysis.

Chapter four: introduces the result and discussion drawn by nonlinear finite element analysis including the validation of the finite element model against the thermal and structural test of concrete bridge deck subjected to fire. Based on the finite element model validation further parametric studies were carried out and more detailed information on time-temperature evolution, load-displacement response, crack pattern, and damage are presented.

The final chapter, chapter five, presents the conclusion based on the result obtained from this study and gives a direction for future work as a recommendation.

CHAPTER TWO
LITERATURE REVIEW

2.1 General

This is a literature review of a previous study carried out by other researchers on the post-fire performance of GFRP stay in place formwork concrete bridge decks at elevated temperature is presented based on numerical and experimental research conducted on GFRP reinforced concrete structural members. However, most numerical research work carried out has been for reinforced concrete beams and columns. This section is organized into several topics including fire, fire requirement of structures, design of structural fire, development of fire, thermal action for analysis of temperature distribution, performance and behavior of GFRP at elevated temperature, the effect of sustained service loading on thermal and creep deflection of GFRP, the effect of sustained service loading on the post-fire performance of GFRP after cooling, the effectiveness of the GFRP strengthening method on flexural response and parameters that affect the fire resistance of GFRP concrete bridge decks.

2.2 Fire

Fire is the chemical reaction that occurs when certain compounds react with oxygen in the air, producing brilliant light, heat, and smoke. In other terms, fire is the process that is formed when combustible fuel or material is burned if they are ignited and oxygen has interacted. Fire is used for cooking domestically, while in industrial for material processing, power, and thermal energy (Dougal Drysdale, 2011). Fire bridges mostly were occurred while a tanker truck that transports fuels or flammable liquids traveling under a specific type of bridge that consists of arches, piers, or columns supporting along elevated railways or roads are failing. Bridge structures were severely damaged in the majority of cases, requiring a high cost of repair. The majority of the bridge damaged by fire is not collapsed but, in some cases, the major structural parts collapsed necessitating the bridges to demolition. Even in the case where only minor structural damage occurred, high costs were incurred as a result of the bridge's temporary closure and inconvenience to traffic to be faced. Taking this into consideration, it's necessary to consider the fire safety design to bridge structures during the design period. Especially, consideration of a fire load case in the form of a localized hydrocarbon fire appears particularly appropriate for viaducts and overpasses, which are frequently subjected to tanker truck fires(Giuliani et al., 2012). Fire, if not properly controlled in the event of

an accident, can result in the loss of lives and property damage. As a result, it is necessary to provide a guide against the improper use of fire, which can result in fire disasters. This necessarily requires that fire resistance and safety be considered when designing a structure.

2.3 Fire requirements of structures.

The structure exposed to fire must be designed and built in such a way that its stability, strength, and integrity are maintained under fire for a reasonable time in the event of a fire. The strength and stiffness of concrete and steel are reduced with increasing temperature. This reduction is only functional between 400^{o} C and 700^{o}C. During this time, the structure is expected to withstand the additional loads and stresses imposed on it as a result of the fire and elevated temperature while the firemen attempt to extinguish the fire(EN 1992-1-2, 2011; Lennon et al., 2007). In other term, the North American building code of standards states that the fire resistance of structures is the capacity of the structure to handle the exposed fire without loss of load-bearing capacity in terms of length of time. This length of time is the measure of the performance of the components to resist factors that affect the fire resistance of structures. The fire resistance of structures depends on factors such as type of fire loads (standard fire or actual fire), building function, height, area, material properties, and the dimension of openings(ASCE, 1992).

2.4 Design of structural fire

As per (EN 1991-1-2, 2011), the design of a structural fire engineering system involves four stages; The first stage is, the selection of appropriate fire design scenarios considering various fire compartments of structures on basis of fire risk assessment and overall safety. This will determine the best way for design purposes. The selected design fire scenario will determine the corresponding design fire which is the second stage of the design of the fire structure. The design fire, in a fire compartment, in each fire scenario, can be estimated according to section 2.6 of this document. The national authorities specify the design fire of the structures as standard fire, if not it must be specified in the design. The third stage of the fire design of the structure is the determination of temperature distribution within the structural members. In case of thermal analysis of the structure, the location of the design fire must be in consideration concerning the structural member and based on fire design selected according to section 2.6 of this

study following separate procedures for temperature distribution of structural analysis; that is, a design fire with nominal temperature-time curve follow a specified period in absences of decreasing of the temperature or cooling phase while a design fire with fire model follows a full time of the fire in addition to cooling phase. Finally, the mechanical behavior of the structural members after exposure to fire is determined depending on thermal action and thermal effects on the material constitute model.

2.5 Development of fire.

Normally, a fire does not start in the right way but it takes some stages. The development of fire, in a fire scenario, consists of a round of six main stages until the occurrence of extinction, those are incipient, fire growth (pre-flash over), flashover, fully developed (post-flash over), decay, and extinction stages as shown in figure 2.1. The incipient stage is a stage at which the cell started to heat. In the growth stage, the development of fire is started with small and localized smoke then the fire will grow larger and emit more gases and smoke. In the event of a flashover, the radiation from the burning flame and the hot smoke layer may cause the instant ignition of unburned combustible materials in the vicinity. The fire enters a fully developed stage after the flashover, with the rate of heat release reaching its maximum which is the most dangerous stage, as structural damage and fire spread are possible. The fire enters into the decay stage as the rate of burning is slow and the combustible material is consumed. Finally, it reaches the extinction stage where there is total a combustible material is consumed and no more energy is generated (Jurgen Garche and Klaus Brandt, 2018).

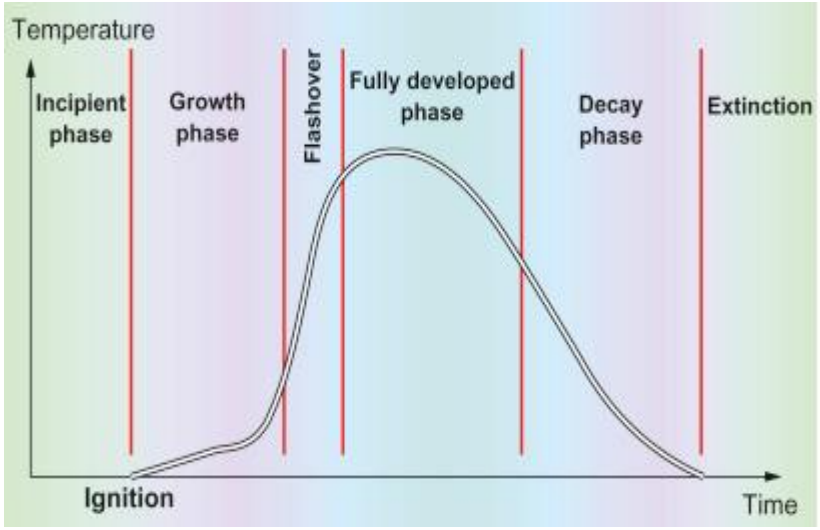

Figure 2.1: Schematic overview of the development and extinction of fire (Jurgen Garche and Klaus Brandt, 2018).

Fires are represented using a temperature-time curve that is roughly similar to the temperature increment in fire scenarios for ease of analysis and design. The fire growth stage is ignored because the fire is still in the act of beginning. A standard fires model, a hydrocarbon fires model, and a parametric design fires model can all be used to represent the fire. According to(EN 1991-1-2, 2011) it is further explained below.

2.5.1 Standard temperature-time curve

The standard fire nominal temperature-time curve captures fires with low heating rates, which are most common in residential buildings, offices, and other structures. The nominal temperature-time curve of a standard fire proposed in(EN 1991-1-2, 2011) is visualized in figure 2.2 and expressed by equation 2.1. One of the draws back of the Eurocode about the nominal temperature-time cure it does not consider the decreasing branch (cooling phase) which affect structural performance especially when there is high thermal strain. As a result, a structural member can be exposed to standard fire conditions by exposing it to elevated temperature in a furnace with the temperature gradient controlled to achieve the standard fire curve.

$$T_g = 20 + 345log_{10}(8t + 1) \quad (2.1)$$

Where,T_g is the gas temperature in the fire compartment (^{o}C); and t is the time (min)

2.5.2 External fire curve

The external fire curve is also one of the temperature-time curves representing the fire condition and appropriate to the structural members that are the most visible side of the main structures. The external fire curve is expressed by the following equation 2.2 according to (EN 1991-1-2, 2011).

$$T_g = 660(1 - 0.687e^{-0.32t} - 0.313e^{-3.8t}) + 20 \quad (2.2)$$

$Where, T_g \; and \; t \; are \; as \; defined \; above$

Also, EN 1991-1-2:2002 develop a temperature-time curve for the cooling phase to evaluate the temperature decrement of the fire in the decay stage. This relationship can be expressed by equation 2.2

$$T_g = \begin{bmatrix} T_{max} - 625(t^* - t^*_{max}) & for\ t^*_{max} \le 30min \\ T_{max} - 250(3 - t^*_{max})(t^* - t^*_{max}) & for\ t^*_{max} < 120min \\ T_{max} - 250(t^* - t^*_{max}) & for t^*_{max} \ge 120min \end{bmatrix} \quad (2.3)$$

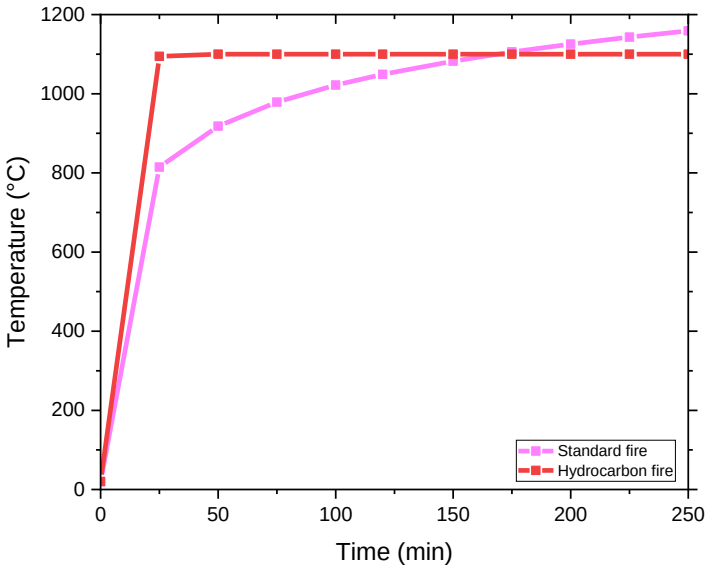

Figure 2.2: Nominal temperature-time curve for standard and hydrocarbon fires used in this study (EN 1991- 1-2:2002, 2011)

2.6 Thermal action for analysis of temperature distribution as per Eurocode

According to (EN 1991-1-2, 2011) the thermal action is given to the surface of the member by net heat flux;$h_{net}\left[\frac{W}{m^2}\right]$ and for a surface exposed to fire the net heat flux can be determined by sum of the net heat flux due to convection and radiation which is expressed by equations 2.4 to 2.5.

$$h_{net} = h_{net,c} + h_{net,r} \tag{2.4}$$

The net heat flux component due to convective; $h_{net,c}$ is given by

$$h_{net,c} = \alpha_c\left(T_g - T_m\right) \tag{2.5}$$

Where, T_g, is the gas temperature of fire exposed member[℃]; T_m is the surface temperature of a member[℃];α_c is coefficient of heat transfer by convection which is dependent on the nominal temperature-time curves:

- For standard time temperature, $\alpha_c = 25\frac{W}{m^2K}$
- For external fire curves, $\alpha_c = 25\frac{W}{m^2K}$
- For hydrocarbon fire, $\alpha_c = 50\frac{W}{m^2K}$
- For a simple fire model, $\alpha_c = 35\frac{W}{m^2K}$

And when the heat transfer by radiation is considered the coefficient of heat transfer by convection;α_c is $9\frac{W}{m^2K}$ for unexposed part of the member

$$h_{net,r} = \emptyset * \varepsilon_m * \epsilon_f * \sigma((T_r + 273)^4 - (T_m + 273)^4); \left[\frac{W}{m^2}\right] \quad (2.6)$$

Where $\emptyset$ is the configuration factor;ε_m is the surface emissivity of the member which is specified depending on material properties, if not its take as 0.8; ε_f is the emissivity of fire usually taken as a unity; σ is the Stephan Boltzmann constant which is equal to $5.67*10^{-8}$ $\frac{W}{m^2K^4}$; T_r is the effective radiation temperature of the fire[℃]; T_m is the surface temperature of the member[℃].

2.7 Production of Pultruded Fiber Reinforced Polymer composite

One of the most essential methods in cost and labor to manufacture the composite material is through the pultrusion process. Pultrusion is a continuous way of manufacturing fiber composite material that has a uniform cross-sectional profile (Sandberg et al., 2020). The FRP composite material manufactured through the pultrusion process can get acceptance in many fields of engineering application such as in the construction sector, aerospace, and automotive. The word pultrusion is combined from two terms that is pull and extrusion. The extrusion can be defined as the pulling of FRP composite material like glass fiber and resin via the molding die. During the pultrusion process to form the profile FRP composite different resin types such as polyester, polyurethane, and vinyl ester epoxy resins can be used(Annu & Ahmed, 2021).

The process of manufacturing the pultruded GFRP composite involves the following stages(Sandberg et al., 2020) and is illustrated in figure 2.3

- The layup of the raw material that made up of rovings, mats, and fabrics drawn from the fiber creels.
- The fiber material is guided through the molds that shape and organize the layup to form the profile. Based on the required application, before entering into the pultrusion die the fiber material is preheated to accelerate the curing process.
- After passing through the guides; the fiber composite material is saturated with a resin. Before entering the pultrusion tool, the resin is saturated in a resin bath. The active and/or passive heating or cooling of the die and composite part was

performed. The process of heating and cooling is to limit the curing of the thermosets (polymerization) and the solidification of thermoplastic (crystallization) throughout the die.

- The fiber profile is pulled through the pultrusion tool, and it is cut depending on the required lengths of the fiber composite profile.

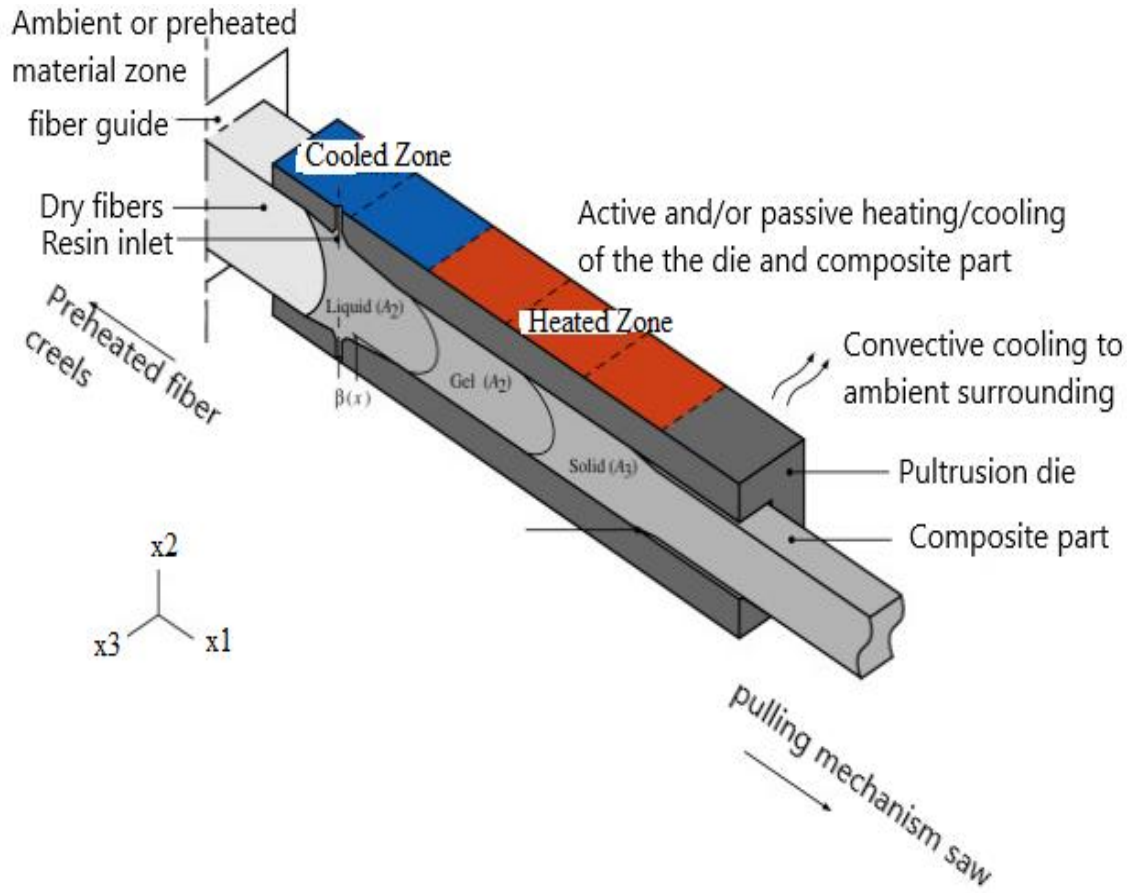

Figure 2.3: The pultrusion process [source: (Sandberg et al., 2020)]

2.8 Hashin damage in fiber-reinforced materials

In the case of the analysis of fiber-reinforced composite materials, the damage has a vital role (Lapczyk & Hurtado, 2007). Fiber composite material shows elastic-brittle failure; sudden failure of the material under load without showing a significant plastic deformation and why the plasticity can be neglected when modeling the behavior of the fiber-reinforced polymer.

2.8.1 Damage initiation

Damage initiation refers to the onset of degradation at a material point. For this damage model, the initiation criteria are based on Hashin's theory (Z. Hashin, 2016) in which the failure surface is expressed in the effective stress space. These criteria consider four

different damage initiation mechanisms: fiber tension, fiber compression, matrix tension, and matrix compression. Hashin's criteria are widely used in the industry, even though numerous studies have shown that they may not predict the onset of failure accurately, especially in matrix and fiber compression modes. The initiation criteria have the following general forms:

Fiber tension ($\sigma_{11} \geq 0$):

$$F_{ft} = \left(\frac{\sigma_{11}}{X^T}\right)^2 + \alpha\left(\frac{\sigma_{12}}{S^L}\right)^2 = 1 \tag{2.7}$$

Fiber compression ($\sigma_{11} < 0$):

$$F_{fc} = \left(\frac{\sigma_{11}}{X^C}\right)^2 = 1 \tag{2.8}$$

Matrix tension ($\sigma_{22} \geq 0$):

$$F_{mt} = \left(\frac{\sigma_{22}}{Y^T}\right)^2 + \left(\frac{\sigma_{12}}{S^L}\right)^2 = 1 \tag{2.9}$$

Matrix compression ($\sigma_{22} < 0$):

$$F_{mt} = \left(\frac{\sigma_{22}}{2S^T}\right)^2 + \left[\left(\frac{Y^C}{2S^T}\right)^2 - 1\right]\left(\frac{\sigma_{22}}{Y^C}\right)^2 + \left(\frac{\sigma_{12}}{S^L}\right)^2 = 1 \tag{2.10}$$

Where, in the above equation σ_{ij} are the components of the effective stress tensor,X_T and X_C represents the tensile and the compressive strength in direction of the fiber, Y_T and Y_C denotes tensile and compressive strength in direction of the matrix while $S_L and$ S_T represents the shear strength of fiber along with the longitudinal and transverse directions. The coefficient α in Eq. (2.7) determines the contribution of the shear stress to the fiber tensile initiation criterion. Based on Hashin proposed by (Z. Hashin, 2016) it is equal to unity.

2.8.2 Damage evolution

Once a damage initiation criterion is satisfied, further loading will cause degradation of material stiffness coefficients. The reduction of the stiffness coefficients is controlled by damage variables that might assume values between zero (undamaged state) and one (fully damage state for the mode corresponding to this damage variable) (Lapczyk & Hurtado, 2007). The evolution law of the damage variable in the post-damage initiation phase is based on the fracture energy dissipated during the damage process *Gc*.

The evolution of each damage variable is governed by an equivalent displacement, δ_{eq}. The equivalent displacement for each mode is expressed in terms of the components corresponding to the effective stress components used in the initiation criterion for each damage mode(Barbero et al., 2013). The equivalent displacement and stress for each of the four damage modes are defined as follows:

Fiber tension ($\sigma_{11} \geq 0$)

$$\delta^{ft}{}_{eq} = L^C * \sqrt{(\langle\varepsilon_{11}\rangle^2 + \alpha\varepsilon_{12}{}^*\varepsilon_{12})} \tag{2.11}$$

$$\delta^{ft}{}_{eq} = \frac{\langle\sigma_{11}\rangle\langle\varepsilon_{11}\rangle + \alpha\sigma_{12}\varepsilon_{12}}{\delta^{ft}{}_{eq}/L^C} \tag{2.12}$$

Fiber compression ($\sigma_{11} < 0$)

$$\delta^{fc}{}_{eq} = L^C\langle-\varepsilon_{11}\rangle \tag{2.13}$$

$$\delta^{fc}{}_{eq} = \frac{\langle-\sigma_{11}\rangle\langle-\varepsilon_{11}\rangle}{\delta^{fc}{}_{eq}/L^C} \tag{2.14}$$

Matrix tension and shear ($\sigma_{22} \geq 0$)

$$\delta^{mt}{}_{eq} = L^C * \sqrt{(\langle\varepsilon_{11}\rangle^2 + \alpha\varepsilon_{12}{}^*\varepsilon_{12})} \tag{2.15}$$

$$\delta^{mt}{}_{eq} = \frac{\langle\sigma_{22}\rangle\langle\varepsilon_{22}\rangle + \sigma_{12}\varepsilon_{12}}{\delta^{mt}{}_{eq}/L^C} \tag{2.16}$$

Matrix compression ($\sigma_{22} < 0$)

$$\delta^{mt}{}_{eq} = L^C * \sqrt{(\langle-\varepsilon_{22}\rangle^2 + \alpha\varepsilon_{12}{}^*\varepsilon_{12})} \tag{2.17}$$

$$\delta^{mt}{}_{eq} = \frac{\langle-\sigma_{22}\rangle\langle-\varepsilon_{22}\rangle + \sigma_{12}\varepsilon_{12}}{\delta^{mc}{}_{eq}/L^C} \tag{2.18}$$

Where$<>$ in the above equation, represents the Macaulay operator which is defined as $\langle\eta\rangle$=0.5(η+|η|) for every real number.

2.8.3 Viscous regularization

Material models showing softening behavior and reduction in stiffness have a problem of converging difficulties in the finite element model. To overcome the convergence difficulties the viscous regulation scheme is taken into account(Ayman et al., 2017; Xin et al., 2017). The viscous regulation in the ABAQUS standard is expressed by the evaluation equation 2.19.

$$d^{v}{}_{l}{}' = \frac{1}{\eta_l}(d_l - d^{v}{}_{l}) \tag{2.19}$$

Where η_l is viscosity coefficient representing the relaxation time of the viscous system and $d^{v}{}_{l}$ is represents regularized damage variable for mode.

2.9 ABAQUS Concrete Damage Plasticity (CDP) model

Concrete is consisted of qualitatively and quantitatively various types of materials. These materials show different characteristics in terms of compression and tension behavior. To determine the concrete damage is difficult since it exhibits the non-linear stress-strain relation of concrete under applied stress conditions and strain hardening/softening(Raza et al., 2019). But, through constitutive models of the materials using the concrete damaged plasticity model, it's possible to represent the non-linear behavior of the concrete under loading which follows the theory of plasticity and damage mechanics. ABAQUS software can allow two ways for simulating the damage in concrete that is concrete damage plasticity (CDP) model and smeared crack concrete model. In this study, CDP models were used by providing plasticity behavior, compressive behavior (inelastic behavior of the concrete in compression), and tension softening of the concrete with their respective damage parameters. This model assumes two main failure mechanisms tensile cracking and compressive crushing of the concrete material(ABAQUS, 2020).

a) Plasticity behavior of concrete

The parameters required to define the plasticity model of concrete are dilation angle (ψ), the plastic potential eccentricity of concrete (ε), the ratio of compressive stress in the biaxial state to the compressive stress in the uniaxial state ($\frac{\sigma_{bo}}{\sigma_{co}}$), the shape factor of the yielding surface in the deviatoric plane (K_c), and viscosity parameter. The default value of the CDP model permitted to use the yield surface, K_c and eccentricity,ϵ, equally to 0.667 and 0.1 respectively. The value of $\frac{\sigma_{bo}}{\sigma_{co}}$ recommended by the ABAQUS user manual(ABAQUS, 2020), is 1.16. Based on large statical data (Papanikolaou & Kappos, 2007) formulate the relationship between characteristic compressive strength of concrete with the stress ratio ($\frac{\sigma_{bo}}{\sigma_{co}}$) by using equation 2.20 below.

$$\frac{\sigma_{bo}}{\sigma_{co}} = 1.5(f'_c)^{-0.075} \tag{2.20}$$

Where: f'_c is the characteristic compressive strength of concrete N/mm^2

b) Compressive behavior of concrete

In concrete damage plasticity models, to define the compressive behavior of concrete, it is necessary to provide the plastic hardening strain in compression $\varepsilon_c{}^{pl,h}$

(V. Kodur, 2014a) and the plastic hardening plays a crucial role in the modeling of concrete in compression behavior to determine the relationship between the damage parameters and the characteristic compressive strength of concrete as illustrated in figure 2.4 and their relationships are represented by equation 2.23 (Hafezolghorani et al., 2017).

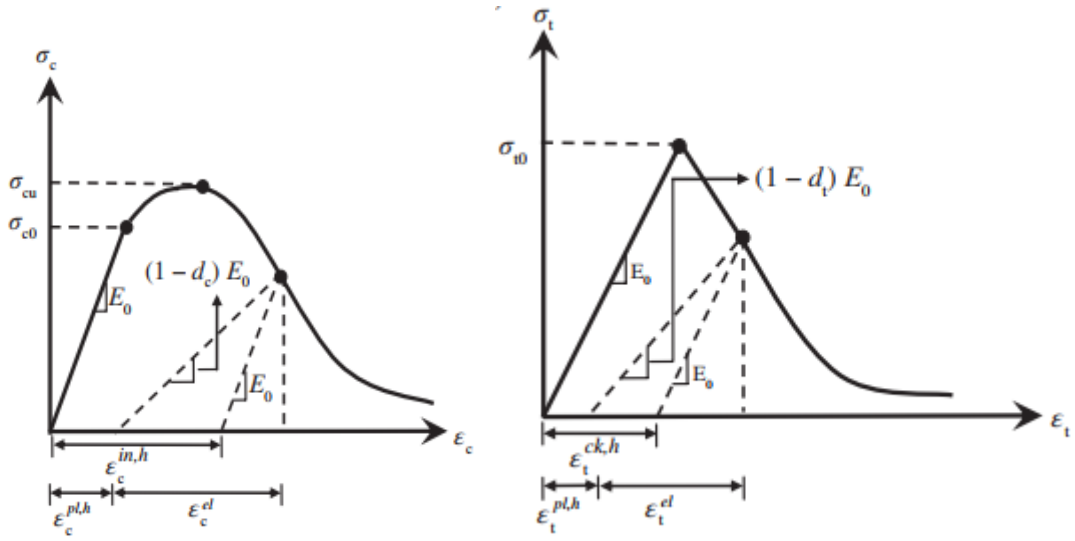

(a) (b)

Figure 2.4:Response of concrete to a uniaxial loading condition (a) in compression (b) in tension [source: (Hafezolghorani et al., 2017)]

All the parameters in figure 2.4a above can be evaluated using the following equations

$$\sigma_c = (1 - d_c)E_O(\varepsilon_C - \varepsilon_c{}^{pl,h}) \tag{2.21}$$

$$\begin{bmatrix} \varepsilon_c{}^{in,h} = \varepsilon_C - \dfrac{\sigma_c}{E_O} \\ \varepsilon_c{}^{pl,h} = \varepsilon_C - \dfrac{\sigma_c}{E_O}\left(\dfrac{1}{1 - d_c}\right) \end{bmatrix} \tag{2.22}$$

$$\varepsilon_c{}^{pl,h} = \varepsilon_c{}^{in,h} - \frac{d_c}{(1 - d_c)}\frac{\sigma_c}{E_O} \tag{2.23}$$

The concrete compression damage $d_{c\ \text{in}}$ the CDP model depends on the inelastic hardening strain of concrete in compression $\varepsilon_c{}^{pl,h}$, which managed the slope of the unloading curve. The compression damage d_c increased with increasing of the inelastic hardening strain in compression. It is expressed by equation 2.24

$$d_c = 1 - \frac{\sigma_c}{\sigma_{cu}} \tag{2.24}$$

From equation 2.24, the compression damage parameter was equal to 0 at the ultimate compressive strength of concrete, and after that, it starts to decrease up to the remaining strength of the concrete in ultimate strain. Generally, in absence of an experimental test on compressive stress-strain of concrete the existing constitutive models can be used. In this study, the modified Hognestad model used by many researchers was used to model the stress-strain relationship of concrete at room temperature (Helmi, 2019; Madandoust et al., 2017). As shown in figure 2.5 the shape of the stress-strain curve is parabolic up to the ultimate compressive strength of the concrete σ_{cu} and starts to linear decrease until 15% ultimate strength of the concrete. Analytical it is represented by equation 2.24.

$$\sigma_c = \sigma_{cu}\left[2\left(\frac{\varepsilon_c}{\varepsilon c'}\right) - \left(\frac{\varepsilon_c}{\varepsilon c'}\right)^2\right] \tag{2.25}$$

Where σ_{cu} and $\varepsilon c'$ were ultimate compressive strength and strain of the concrete respectively, and σ_c and ε_c were the nominal compressive strength and strain of the concrete respectively.

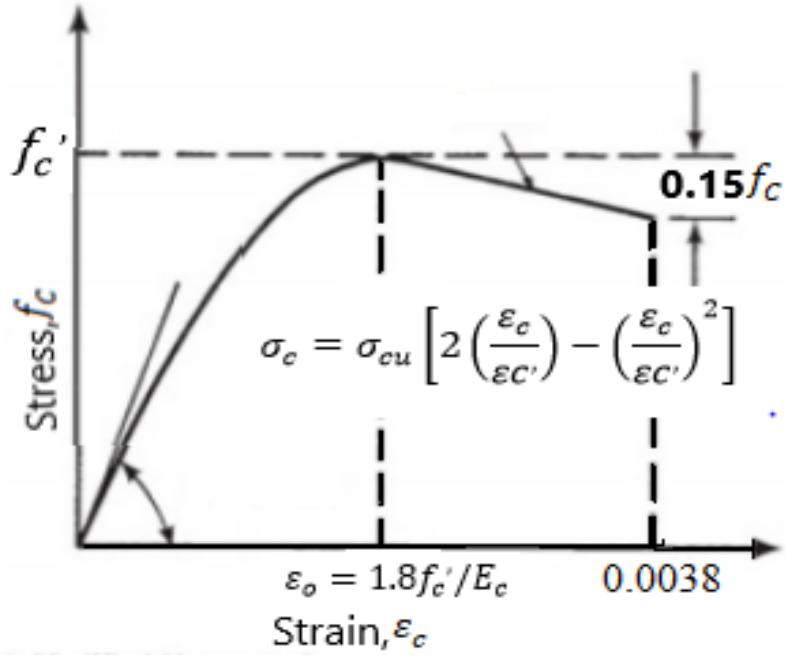

Figure 2.5: New modified Hognestad compressive stress-strain of concrete [source :(Madandoust et al., 2017)

c) Tensile behavior of concrete

The tensile characteristics of the reinforced concrete can be simulated completely in ABAQUS using the post-failure stress-strain relation similar to figure 2.4b. This relationship considers the tension stiffening, strain-softening, and the interaction between concrete and reinforcement rebar. In numerical model; the elastic modulus, (E_o), tensile stress (σ_t), cracking strain (${\varepsilon_t}^{ck,h}$), and damage parameter (d_t) for the specified grade of concrete strength must be provided into the FE software by the user. The cracking strain (${\varepsilon_t}^{ck,h}$) can be calculated from the total strain according to equation 2.27; where ε_t total strain. Then, the ABAQUS program(ABAQUS, 2020)check the accuracy of the damage curve using the plastic strain values as calculated by equation 2.29. The negative and /or the descending order of tensile plastic strain values cannot be permitted in ABAQUS and if it's the program exit the submitted job for analysis warning message as error.

$$\sigma_t = (1 - d_t)E_0\left(\varepsilon_t - {\varepsilon_t}^{pl,h}\right) \tag{2.26}$$

$${\varepsilon_t}^{ck,h} = \varepsilon_t - \frac{\sigma_t}{E_0} \tag{2.27}$$

$${\varepsilon_t}^{pl,h} = \varepsilon_t - \frac{\sigma_t}{E_0}\left(\frac{1}{1 - d_t}\right) \tag{2.28}$$

$${\varepsilon_t}^{pl,h} = {\varepsilon_t}^{ck,h} - \frac{\sigma_t}{E_0}\frac{d_t}{(1 - d_t)} \tag{2.29}$$

As illustrated in figure 2.4b the tensile damage parameter of the concrete (d_t) increase with the cracking strain(${\varepsilon_t}^{ck,h}$) further increase and can be analytically determined by equation 2.30.

$$d_t = 1 - \frac{\sigma_t}{\sigma_{to}} \tag{2.30}$$

There is various form of constitutive model that expresses the tension stiffening of the concrete as reviewed by (Nayal & Rasheed, 2006). In this study, the constitutive model established by (Nayal & Rasheed, 2006) was selected as applicable for both fiber and reinforced concrete structures with a few modifications as illustrated in figure 2.6b. Additionally, this constitutive model has similarities with the tension stiffening models required for the ABAQUS CDP model. This tension stiffening model is initially based on the work of (Gilbert and Warner, 1978) which considers tension softening, the effect of bond-slip, and tension stiffening. According to (Gilbert and Warner, 1978) two de-

scending parts of the tensile stress-strain of concrete can accurately capture the behavior of concrete at primary and secondary cracking stages. The tensile stress-strain of concrete according to (Nayal & Rasheed, 2006) presented in figure 2.6a, and the new modified tension stiffening model used in the current study were presented in figure 2.6b; which is taken directly from (Wahalathantri et al., 2021). At the peak cracking strain (ε_{cr}) the sudden drop from the peak tensile stress σ_{to} *to* 80% σ_{to} used by (Nayal & Rasheed, 2006) and slanted from (ε_{cr},σ_{to}) to ($1.25\varepsilon_{cr}$,σ_{to}) to prevent the run time error in ABAQUS constitutive material model(Gilbert and Warner, 1978). As presented in figure 2.6a and b, after this point the model follows the same pattern in both primary and secondary cracking stages of the concrete under tensile stresses but to avoid the run time error in ABAQUS CDP model the tensile stress-strain of the concrete continued only until (8.7 ε_{cr},10% σ_{to}).

The equation of cracking strain at room temperature and the elevated temperature was taken from (Liao & Huang, 2018; Martinez & Jeffers, 2018), and the analytical is expressed in Equations 2.31 and 2.32 respectively.

$$\varepsilon_{cr} = \frac{f_{ctm}}{E_C} \quad at\ room\ temperature \tag{2.31}$$

$$\varepsilon_{cr,T} = \frac{f_{ctm,T}}{E_{C,T}} \quad at\ eleveted\ \ temperature \tag{2.32}$$

Where, ε_{cr} is the cracking strain, f_{ctm} is the cracking stress of the concrete (peak tensile stress) which is determined by equation 2.33.

In the absence of experimental data, the mean value of tensile strength f_{ctm} in MPa may be estimated for normal weight concrete from the characteristic's compressive strength f_{ck}. In this study, the equation 2.33 of the international federation for structural concrete (fib, 2010) was used assuming($\sigma_t = f_{ctm}$).

$$f_{ctm} = 0.3(f_{ck})^{\frac{2}{3}}\ \ concrete\ grade\ \leq C50 \tag{2.33}$$

$$f_{ctm} = 2.12.\ ln(1 + 0.1 \times (f_{ck} + \Delta f))\ \ concrete\ grade\ \geq C50 \tag{2.34}$$

Where: f_{ctm} is the characteristics compressive strength in MPa,Δf which set to 8 MPa

The upper and lower limit value of the characteristic's tensile strength $f_{ctk,min}$ and $f_{ctk,max}$ can be estimated from the following equations 2.35 and 2.36.

$$f_{ctk,min} = 0.7 f_{ctm} \quad (2.35)$$

$$f_{ctk,max} = 1.3 f_{ctm} \quad (2.36)$$

d) Other parameters

The elastic modulus and Poisson's ratio of the concrete is another parameter that influences the behavior of concrete under loading. The elastic modulus (E_o) can be defined as the tangent modulus of elasticity at the origin of the stress-strain diagram of the concrete. It is equal to the slope of the secant of the unloading branch for rapid unloading and does not include the initial plastic deformation(fib, 2010).

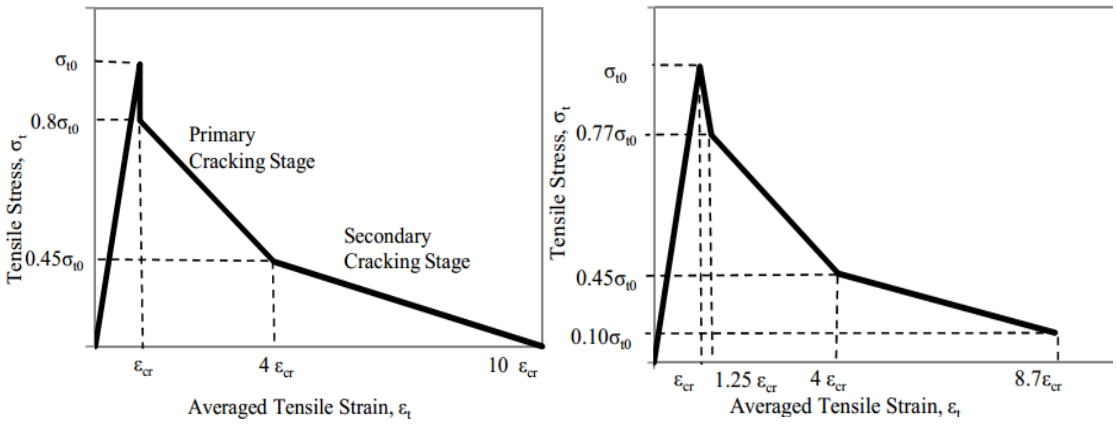

Figure 2.6: Tension stiffening model (a) Nayal and Rasheed (2006) and (b) Modified tension stiffening model for ABAQUS used in the current study[source: (Wahalathantri et al., 2021)]

There is the various constitutive model to determine the elastic modulus of concrete in absence of experimental data (ACI 318-95, 1995; EN 1992-1-1, 2011) In this study, the relationship of elastic modulus of concrete with the characteristic compressive strength of the concrete at 28 days according to American Concrete Institute (ACI 318-95, 1995) is used (see equation 2.37). For the range of the stress between -0.6 $f_{ck} < \sigma_c < 0.8$ f_{ck} the Poisson ratio of the concrete (V_c) for the design purpose, particularly at the ultimate limit state to consider the influence of crack formation, the Poisson ration 0.2 meets the required accuracy(fib, 2010).

$$E_O = 4700\sqrt{f_{C'}} \quad (2.37)$$

2.10 Previous studies on FRP under fire

In this section, the previous findings on the fire performance of FRP concrete structures are reviewed. But there are limited studies in the literature on fire performance of FRP

concrete decks and current design codes do not have any specification documents and design guidelines relating to the fire performance of FRP when exposed to elevated temperature. Some of the important studies relating to experimental and numerical work on fire resistance of FRP concrete structures are reviewed in the following.

2.10.1 Performance and behavior of FRP at elevated temperature

The use of fiber-reinforced polymer (FRP) composites getting acceptance in civil engineering owing to their lightweight, strength, and corrosion resistance than the traditional construction materials (Hollaway, 2010). Recently, the Pultruded Glass Fiber Reinforced Polymer has emerged as a new construction material in the construction of bridge decks and buildings. But, because of the combustible nature of their polymer matrix, there are well-founded concerns about how they will behave at high temperatures and in the presence of fire. These concerns are made difficult the widespread acceptance of GFRP profiles, particularly in buildings that must meet relatively severe fire reaction and fire resistance behavior requirements(Correia, Bai, & Keller, 2015).

Several authors investigate the behavior of GFRP at elevated temperature (Gooranorimi et al., 2018) performs an experimental investigation on GFRP reinforced concrete slab exposed to fire for 120 min according to ASTM E119 (ASTM, 2014) the maximum temperature recorded on GFRP surface extracted from the slab is 115 ^{o}C and also (Correia et al., 2015; Keller et al., 2005) obtain the glass transition temperature of GFRP 100 ^{o}C and 117 ^{o}C with the softening temperature (T_s) of E-glass about 830 ^{o}C accordingly.

The Glass Fibers Reinforced Polymers (GFRP) retains their thermal and mechanical properties at moderate to elevated temperatures. The E-glass fibers reinforced polymers composite have a glass transition temperature around 650 ^{o}C, at this temperature the thermophysical and mechanical properties of the polymer matrix are deteriorated, especially when tested near the glass transition temperature (Ou & Zhu, 2015). Above their glass transition temperature, the polymers lose their states and less in transferring loads to the fiber. At this viscoelastic stage, there is a dramatic reduction in the mechanical properties of the FRP composites. Because of this, the glass transition temperature is the main parameter that must be considered during the design of the fire resistance of FRP composites subjected to elevated temperature and fire(Goertzen & Kessler, 2007). Previous research has confirmed that GFRP systems perform poorly in high temperatures. (Gooranorimi et al., 2018) investigated the post-fire performance of GFRP RC

slab and mechanical behavior of GFRP exposed to fire for 120 min according to ASTM E119.The result indicates that the maximum temperature recorded at the mid location of GFRP is 115 ^{O}C which is located in the range the glass transition temperature 80 ^{o}C to 120 ^{o}C of GFRP and the slab reinforced with GFRP fine sand coated surface of helically wrapped fiber strands shows increases in average load capacity of 10% while slab reinforced with the GFRP ribbed deformed bar like steel rebar reduced in average load capacity because of the surface enhancement. Also, the residual strength (transverse shear strength and horizontal shear strength) of GFRP was investigated by extracting the GFRP rebar from the slab exposed to fire. The transverse shear strength of GFRP tested as per ASTM D7617 indicates that the GFRP fine sand coated and GFRP deformed bar had 5% and 11% reduction respectively while the horizontal shear strength tested according to ASTM D4475 had a reduction in 15% and 7% compared with unexposed rebar. (Ou & Zhu, 2015) also investigated the performance of GFRP at various temperatures ranging from -25 °C to 100 °C were used to assess the effects of temperature on mechanical properties. It was found that Young's modulus, tensile strength, and toughness all decreased with increasing temperature, while ultimate strain remained nearly constant from 25 °C to 50 °C and increased at higher temperatures. The modulus of elasticity, tensile strength, and stiffness all decreased by 28.9 %, 27.3 %, and 17.4 %, respectively, when heated to 100 °C.

Furthermore, some works in the literature address the effect of different temperatures on the mechanical properties of pultruded GFRP profile(Correia et al., 2013; Correia, Bai, & Keller, 2015; Sousa et al., 2014). For instance, (Correia et al., 2013)conducted an experimental study to investigate the mechanical response of pultruded GFRP specimens made of polyester resin under various ranges of temperatures from room temperature to higher than transition temperature (20 ^{o}C to 250 ^{o}C) at different heating rates (1 ^{o}C/min, 2 ^{o}C/min, 4 ^{o}C/min, 6 ^{o}C/min and 8 ^{o}C/min). At moderately high temperatures, i.e., values close to or slightly higher than the T_g of the polymer matrix, the mechanical behavior of GFRP rapidly deteriorated. It is much more vulnerable under shear and compression than under tension. Tensile strength is considerably reduced when the GFRP pultruded material is exposed to elevated temperature, but at 220 ^{o}C the material still retains about 54% of its ambient temperature strength. Shear and compressive strengths were significantly reduced for elevated temperatures, exhibiting strength retentions compared to ambient temperature of only 11% and 5%, respectively.(Correia,

Bai, Keller, et al., 2015)reviewed the thermal and mechanical properties of pultruded GFRP profiles at elevated temperatures. Before the decomposition of its polymer matrix, the density of a GFRP material remains constant and significantly reduced at higher temperatures. The decomposition temperature of GFRP is around 300 ^{o}C. The specific heat capacity of GFRP increases as temperature increases and the thermal conductivity of the fibers and the resin inside an FRP material can change when the temperature increases. More significantly, fibers may be deboned from the resin as decomposition occurs, and voids may be created because of the decomposed gases.

At the structural scale,(M. Nelson & Fam, 2013) conducted experimental testing on the performance of GFRP permanent forms replacing the bottom reinforcement layer with T-shaped. This study was concerned with the comparison of GFRP SIP formwork with the convectional steel based on their failure mode, performance under service load, and punching shear. The bridge decks reinforced with steel shows progressive punching shear failure while the bridge deck with GFRP SIP forms had 7.8% greater than conventional steel service load plus impact. The residual performance of GFRP after being exposed to fire has also been carried out(Alsayed et al., 2012; Ellis et al., 2018; Schmidt & d'Almeida, 2018). The residual tensile properties of GFRP with a vinyl ester matrix that had been exposed to various temperatures (100 ^{o}C, 200 ^{o}C, and 300 ^{o}C) for different periods of exposed fire (1, 2, and 3 h) was investigated. The higher temperatures and longer exposure times resulted in a significant loss of GFRP properties. It was found that GFRP losses the tensile strength of 9.4%, 19.8%, and 21.8% for a 1 hour of exposure to a temperature of 100 ^{o}C, 200 ^{o}C, and 300 ^{o}C respectively compared to 3 hours of exposure period with the same temperature which had a loss in tensile strength of 19.4%, 19.8%, and 21.8 % respectively. From this result, the authors conclude that the decrease in performance of GFRP is due to the increase in temperature influences the bond between the fibers(Alsayed et al., 2012). Until now, there is a limited study on the post-fire performance of GFRP SIP for concrete bridge decks to assess its performance under fire. According to the knowledge of (Nicoletta et al., 2019) is the only one that has been frist conducted on fire performance of FRP SIP formwork for concrete bridge decks. The study indicates that the fire-damaged GFRP SIP formwork concrete deck exposed to 15 min heptane pool fire had around 13% higher ultimate capacity compared with undamaged concrete decks due to thermal expansion of GFRP formwork.

Many researchers have focused on numerical investigation rather than experimental study due to the expensive cost and time to investigate the fire performance of the structural members(Cai et al., 2020; Hajiloo & Green, 2019; Hashim & Kadhum, 2021; Xu et al., 2017).(Reshma Merin Roy & Jeena B Edayadiyil, 2016) Numerically investigate the transient thermal analysis using commercially available software ANSYS to assess the deflection behavior and thermal behavior of CFRP, Steel, and GFRP exposed to elevated temperature. From the analysis, the maximum measured deflection value for steel bars, CFRP and GFRP is 0.5449mm, 0.0564mm, 0.05mm respectively. Since the GFRP reinforced beam has less deformation as compared with CFRP and steel reinforced beam; FRP can be used as a better alternative to steel reinforcement as both CFRP & GFRP bars have nearly equal deformation. Another researcher (Morgado, Silvestre, et al., 2018) also conduct a numerical investigation on fire resistance of pultruded GFRP beam exposed to ISO 834 using ABAQUS standard. The three-dimensional finite element modeling of pultruded GFRP beam has been developed considering constitutive material properties at elevated temperatures without implementing any failure criterion. The developed model was verified against experimental results based on temperature evolution and load-deformation of the pultruded GFRP beam, and further parametric studies on the type of fire exposure, effect of thermal expansion of GFRP, and load levels were investigated. The result indicates that thermal expansion of GFRP has a greater effect on the mechanical response of pultruded GFRP beam and the numerical simulation of the fire behavior of pultruded GFRP beam using ABAQUS standard predicts accurate results.

2.10.2 Effect of sustained service loading on FRP at elevated temperature

The effect of sustained service loading on FRP reinforced concrete structures has been investigated by many scholars. However, there is still a limited study on pultruded GFRP. (Bellakehal et al.,2014) performed an experimental and analytical study on GFRP by simultaneously heating and loading. During this study different parameters were considered such as concrete cover thickness, GFRP diameter, and temperature variation to assess the effect of the sustained service loading and temperature effect on the thermal strain of the GFRP rebar. The sustained mechanical load is 20% of the ultimate strength of the slab around 40KN at a temperature varying from 20 to -30 ^{o}C and -30 to 60 ^{o}C with a temperature increment of 5 ^{o}C. The applied sustained load and temperature did not show any influence on the transversal thermal strain of GFRP bars em-

bedded in concrete but above 40 ºC the longitudinal thermal strain at the slippage interface between concrete and GFRP shows reduction. This reduction reaches 30% for the temperature of 60 ºC compared to the undamaged specimen.

The effect of sustained load at elevated temperature was also investigated by (Thongchom et al., 2019). This study investigates the effect of sustained service loading at an elevated temperature ranging from 700 and 900 °C for 180 min and air cooling in the furnace. The result indicated that sustained service loading did not significantly affect the peak temperature at the bottom layer of steel reinforcement and the fire resistance of the RC beam exposed to fire. However, sustained service loading increased the creep deflection at elevated temperatures above the temperature of 500 °C and leads to failure of RC beams less than a 180 min fire exposure period based on deflection limit. Additionally, the effect of sustained load on the post-fire performance of the structure was conducted by (Lenwari et al., 2020). This study is concerned with the post-fire performance of reinforced concrete beams subjected to cyclic load after being exposed to a fire for 3 hours, air-cooled, and strengthened with CFRP plates. The parametric study includes the level of exposure temperature (700 or 900 °C), sustained service loading (in addition to the beam self-weight) at the elevated temperature, and the CFRP plate length. The bottom reinforcement beam exposed to 900 ºC gained maximum temperature above the critical value of 593 °C while almost 700 °C exposed beam experienced below 593 °C. The presence of continuous service loading at elevated temperatures did not have a noticeable impact on the bottom steel reinforcement temperature records. It encouraged the creep deflection, however, which led to the 900 °C exposed beams failure of deflection before 3 hours, during exposure to fire, and injuring to the post-fire performance of structures at elevated temperature. The bending of fire-damaged beams may be reinstated by externally bonded CFRP plates and extending the CFRP plate near the supports, the degree of ultimate strength enhancement for the fire-damaged beams can be increased

2.10.3 Effectiveness of strengthening fire-damaged structures using FRP

When RC members are exposed to high temperatures during a fire, they suffer extensive damage, which can result in significant losses in load carrying capacity, compressive and bond strengths of concrete, and plastic deformation of steel bars(Jadooe et al., 2017, 2018). These strength losses due to fire result in the total or partial demolition of the structures. As a result, there is an increasing need to understand the impact of high

temperatures on structures and develop appropriate post-fire repair and rehabilitation techniques. Furthermore, the time and ways of strengthening is the critical factor, since any delays result in a significant impact on the financial problems. Therefore, fire-damaged structural strengthening is the main concern of future studies. Various studies have been conducted on ways of repairing and retrofitting fire-damaged concrete structures using fiber-reinforced polymer(Al-Salloum et al., 2016; Alshannag & Alshenawy, 2020; Yaqub et al., 2013). For example,(Yaqub et al., 2013) experimentally investigate the effectiveness of strengthening the post-heated square and rectangular columns using ferrocement, Glass fiber reinforced polymers(GFRP), and Carbon Fiber Reinforced polymers (CFRP) and were all columns tested under axial compression. The result indicates that the FRP jackets increased the compressive strength, ductility, deformation ability, and energy dissipation capacity of post-heated columns but did not increase the stiffness while ferrocement jackets increase both stiffness and strength of post-heated columns. Strengthening the fire-damaged concrete with the integration of both ferrocement and FRP is more effective. Another researcher(Kai et al., 2011) conduct an experimental investigation on the strengthening of fire-damaged T-beams. During the test, one T-beam was tested at ambient temperature to evaluate the mechanical behavior of the beam at room temperature and three T-beams were subjected to fire for 75 minutes according to ISO 834 standard fire curve. Among these three T-beams, one T-beam was not strengthened and two T-beams are strengthened by Carbon Fiber Reinforced Polymer (CFRP) sheets. The test results showed that external strengthening the fire-damaged T-beams with CFRP sheets enhances the load-carrying capacity and stiffness of the beam. However, the ductility of the fire-damaged beams was decreased.

The numerical investigation was also conducted on fire-damaged concrete structures. (Bhuvaneshwari & Mohan, 2020) In this work both numerical and experimental study has been conducted on the strengthening fire-damaged column using a recent innovative material; Glass Fiber and Polypropylene Fiber-Based Engineered Cementations Composites (GFPPECC). During the study both moderate (500 ^{O}C and high (900 ^{O}C) intensities of fire load as per ISO 834 were adopted and implemented into finite element software ANSYS. The result indicates that strengthening of the fire-damaged column restored about 68% of the stiffness compared with the unstrengthened one.

2.10.4 Parameters that affect fire performance of FRP

Correia, et al., (2018) Perform an experimental study on 12 pultruded GFRP beams subjected to a fire load temperature curve according to ISO 834 to evaluate their fire resistance.

During the test, the authors consider different parameters such as the number of sides exposed to fire, load level, and fire protection system that is believed to significantly affect the fire resistance of GFRP beams. The result indicates that exposing the beam to fire with three exposure have a radical change on the fire resistance of the beam while increasing the load level caused a moderate reduction of fire resistance of the beam. (Hussien & Al-thairy, 2020) numerical investigate the performance of GFRP reinforced concrete beams subjected to high temperatures ranging from 20 to 600 ^{o}C using finite element software ABAQUS. The paper concludes that the number of sides the beam exposed to temperature has more influence on load carrying capacity of beam compared with the exposed length of the beam. Exposing the beam with the temperature of 600 ^{O}C to one side (top surface), one side (bottom soffit) and three sides the maximum carrying capacity of the beam reduced by 11.5%,13% and 13% respectively. In general, from the reviewed paper basic factors that influence the performance of the GFRP subjected to fire were not considered.

2.11 Constitutive material models of concrete at elevated temperatures

Numerical analysis of the post-fire performance of GFRP SIP formwork for concrete bridge decks; requires the material properties of concrete and GFRP at elevated temperatures. These material properties are categorized into two parts: (i) thermal properties and (ii) mechanical properties. The thermal properties include mass or density, specific heat capacity, and thermal conductivity. The thermal properties of the materials manage the transfer of heat and temperature distribution across the section while the mechanical properties of the material include elastic modulus, poisons ration, tensile strength, shear strength, compressive strength, stress-strain, thermal strain or thermal expansion, and transient strain which determines the stiffness, strength, and deformation of the material after exposure to elevated temperature. Therefore, in this part, some of the existing models on normal strength concrete (NSC) and Glass Fiber Reinforced Polymer (GFRP) at elevated temperature are reviewed and the best fit model is proposed for finite element inputs.

2.11.1 Thermal properties of concrete at elevated temperature

The temperature-dependent thermal properties of concrete are governed by mass loss, thermal conductivity, and specific heat capacity. These properties are mostly affected by types of aggregates, moisture content, and concrete mix. Previously, much experimental research is conducted for determining thermal properties of concrete at elevated temperatures (Ki-Yeol Shin, 1999; K. R. Kodur et al., 2009; Othuman Mydin & Wang, 2012) and reviewed the influence of temperature on thermal properties of various types of concrete including steel fiber reinforced concrete.

2.11.1.1 Density or mass loss

Based on density, concrete can be classified into two major parts: normal-weight concrete with a density between 2150 to 2450 kg.m^{-3} and lightweight concrete with a density of between 1350 and 1850 kg.m^{-3}(V. Kodur, 2014b). The density of the concrete is influenced by free water loss and reduced with increasing temperature. European code (EN 1991-1-2, 2011) develop the expression for the variation of density relating with temperature by equation 2.38 and graphically the variation of density of concrete with temperature is illustrated in figure 2.7. The density of the concrete remains constant between the temperature of 20 ^{o}C to 115 ^{o}C and decrease above the temperature of 115 ^{o}C and defined as follows:

$$\rho_{c,T} = \begin{bmatrix} \rho_{c,20} & for\ 20\ ℃ \le T \le 115\ ℃ \\ \rho_{C,20}\left[1-\frac{0.02(T-115)}{85}\right] & for\ 115\ ℃ < T \le 200\ ℃ \\ \rho_{C,20}\left[0.98-\frac{0.03(T-200)}{200}\right] & for\ 200\ ℃ < T \le 400\ ℃ \\ \rho_{C,20}\left[0.95-\frac{0.07(T-400)}{800}\right] & for\ 400\ ℃ < T \le 1200\ ℃ \end{bmatrix} \quad (2.38)$$

Where $\rho_{c,T}$ the density of concrete at specified temperature T in ^{o}C

$\rho_{c,20}$ the density of concrete at ambient temperature, 20 ^{o}C.

2.11.1.2 Thermal conductivity

The thermal conductivity of the concrete is a measure of heat conduction in concrete and is the ratio of heat flux to change in temperature. The ability to conduct the heat of the concrete is influenced by moisture contents; since the concrete contains moisture in different forms, types, and amounts(V. Kodur, 2014b). The thermal conductivity of concrete is determined by a steady-state or transient test(ASTM E1530, 2013). Due to the physical and chemical change of concrete at elevated temperatures causing the flow

direction of heat; the transient method of measuring the thermal conductivity of concrete is preferable.

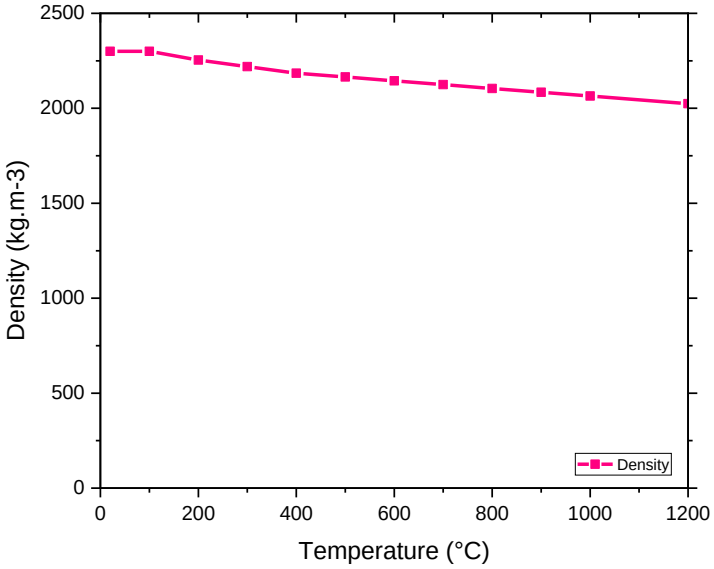

Figure 2.7: Variation in density of normal strength concrete with temperature

Based on the experimental investigation and study different codes of building standards formulate the relation between temperature and thermal conductivity of concrete. European code(EN 1991-1-2, 2011) and ASCE code(ASCE, 1992) develop the expression for the variation of thermal conductivity with temperature as illustrated in equations from 2.39 to 2.43. Graphically the variation of thermal conductivity of concrete with temperature is illustrated in figure 2.8. According to the European code of standard, the thermal conductivity of the upper and lower limit of the concrete decreases with increasing temperature while as per the ASCE code of standard the thermal conductivity of siliceous aggregate concrete decrease with the increase of the temperature up to 800 ℃ and remain constant for the temperature greater than 800 ℃. For carbonate concrete aggregate its uniform between the temperature of 0 ℃ to 293 ℃ and decrease with increasing of temperature above 293 ℃.

A). Eurocode model

The upper limit of thermal conductivity, K_c of normal weight, concrete can be expressed by:

$$K_c = 2 - 0.2451\left(\frac{T}{100}\right) + 0.00107\left(\frac{T}{100}\right)^2 \frac{W}{mK} \qquad for\ 20℃ \leq T \leq 1200℃ \qquad (2.39)$$

Where T is the temperature of concrete in ℃ and K_c is the thermal conductivity of concrete in $\frac{W}{mK}$

The lower limit of thermal conductivity, K_c of normal weight, concrete can be determined by:

$$K_c = 1.36 - 0.136\left(\frac{T}{100}\right) + 0.0057\left(\frac{T}{100}\right)^2 \frac{W}{mK} \qquad for\ 20\ ℃ \leq T \leq 1200\ ℃ \quad (2.40)$$

B). ASCE model

For siliceous aggregate concrete

$$K_C = -0.000625T + 1.5\ W\ m^{-1}℃^{-1} \qquad for\ 0\ ℃\ \leq T \leq 800\ ℃ \quad (2.28)$$

$$K_C = 1\ W\ m^{-1}℃^{-1} \qquad for\ T > 800\ ℃ \quad (2.41)$$

For carbonate aggregate concrete

$$K_C = 1.355\ W\ m^{-1}℃^{-1} \qquad for\ 0\ ℃ \leq T \leq 293\ ℃ \quad (2.42)$$

$$K_C = -0.001241T + 1.7162\ W\ m^{-1}℃^{-1} \quad for\ T > 293℃ \quad (2.43)$$

Where T is the temperature of concrete in ℃

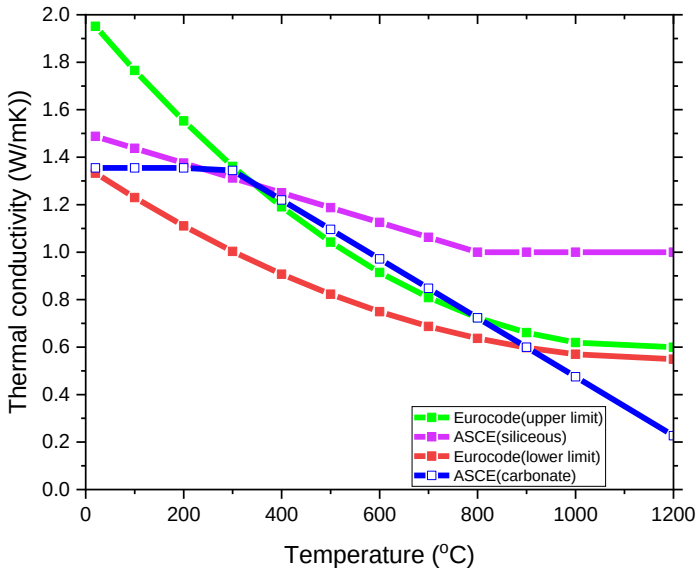

Figure 2.8: Variation in thermal conductivity of normal strength concrete with temperature

2.11.1.3 Specific heat capacity

The specific heat is the amount of heat required per unit mass to alter the temperature of a material by one degree and is expressed in terms of thermal capacity which is the product of specific heat and mass loss(V. Kodur, 2014b). The specific heat capacity of the concrete is influenced by the water in concrete and types of aggregates. The types of aggregate have little effect on the specific heat capacity of concrete and with all

types of aggregates, it is increased with increasing temperature. The approximate value of the specific heat capacity of the concrete is around 1170 J/kg℃ (ASCE, 1992). This model does not consider any variation in moisture content. The model considers the variation due to aggregate types. In this study, the Eurocode(EN 1991-1-2, 2011) and ASCE code(ASCE, 1992) specific heat capacity temperature-dependent were used. Hence, the Eurocode model in reverse to the ASCE code of standard considers the moisture content of concrete which influences the capability of the specific heat capacity of concrete than types of aggregate. This has been considered when the moisture content is considered in an explicit analysis by setting the peak value of the specific heat capacity to 900 J/kg °C at 0% moisture content, 1470 J/kg °C at 1.5% moisture content, and 2020 J/kg °C at 3% moisture content with the peak temperature between 100 °C and 115 °C. The temperature-dependent specific heat capacity according to Eurocode is expressed by equation 2.44 and graphically illustrated in figure 2.9.

$$\begin{bmatrix} 900 & for\ 20\ °C \leq T \leq 100\ °C \\ 900 + (T - 100) & for 100\ °C < T \leq 200\ °C \\ 1000 + \left(\frac{T - 200}{2}\right) & for\ 200\ °C < T \leq 400\ °C \\ 1100 & for\ 400\ °C < T \leq 1200\ °C \end{bmatrix} \quad (2.44)$$

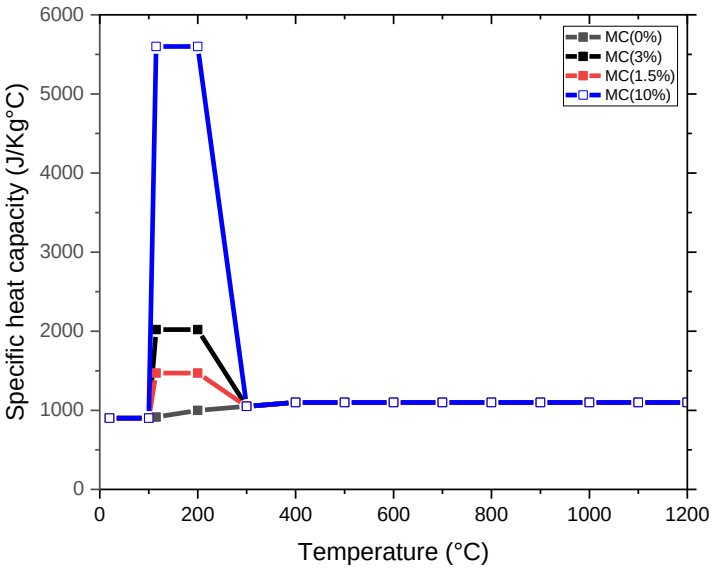

Figure 2.9: Variation in specific heat capacity of normal strength concrete with temperature

2.11.1.4 Thermal diffusivity

The thermal diffusivity of concrete can be defined as a function of thermal conductivity, specific heat, and density of concrete(ASCE, 1992) and it indicates the performance

of concrete in transient heat conduction. The thermal diffusivity of normal strength concrete consists of different mix rations that have different thermal conductivity and specific heat capacity. The normal strength concrete with less thermal diffusivity is preferred over concrete with higher thermal diffusivity in the case of acting as heat insulation in transient heat transfer(Talebi et al., 2020). At high temperatures, the thermal diffusivity of concrete decreases with increasing temperature and is given by the following equation 2.45.

$$D = \frac{K}{\rho C_c} \tag{2.45}$$

Where D= thermal diffusivity ($\frac{m^2}{s}$);

K=thermal conductivity ($\frac{W}{mK}$);

ρ=density ($\frac{Kg}{m^2}$);

C_c=specific heat capacity ($\frac{J}{KgK}$).

2.11.2 Mechanical properties of concrete

The most common important mechanical properties of concrete in fire resistance design are compressive strength, tensile strength, elastic modulus, poisons ratio, and stress-strain response in compression. Extensive research has been received in comparison to the thermal properties of concrete than on the mechanical properties of concrete at elevated temperatures (Li et al., 2004; Tang & Lo, 2009). In this section, the reduction in mechanical properties of concrete at elevated temperatures is discussed.

2.11.2.1 Compressive strength

The most important property of concrete is its compressive strength. Initial curing, moisture content at the time of testing, and the addition of admixtures and silica fume to the concrete mix are all factors that directly affect compressive strength at elevated temperatures(Sideris, 2007). These factors are not addressed in the literature, and no test data exists to demonstrate their influence on the high-temperature mechanical properties of concrete. Figure 2.10 illustrates the variation of compressive strength ratio for normal strength concrete at elevated temperature for siliceous and carbonate aggregates according to Eurocode (EN 1991-1-2, 2011). Between the temperatures, 20°C to 100 °C the reduction in compressive strength for both types of aggregates is the same.

However, between 100 to 1000 °C shows a larger variation in the reduction of compressive strength. In general, for both types of aggregates, the compressive strength decreases as the temperature rises.

2.11.2.2 Tensile strength

Because tensile strength is much lower than compressive strength, it is usually ignored in strength calculations at room and elevated temperatures. However, from the perspective of fire resistance, it is an important property, since cracking in concrete is generally caused by tensile stresses, and structural damage of the member in tension is frequently caused by progression in micro-cracking(Sidney Mindess and J. Francis Young, 2003). If it is important to account for the effect of tensile strength of concrete Eurocode(EN 1991-1-2, 2011) allow the reduction factor coefficient,$K_{c,t}(T)$ as given in expression below and illustrated graphically with the variation of temperature in figure 2.11. Equation 2.46 to 2.48 is applied in absence of more data based on the reduction tensile strength of the concrete at elevated temperatures.

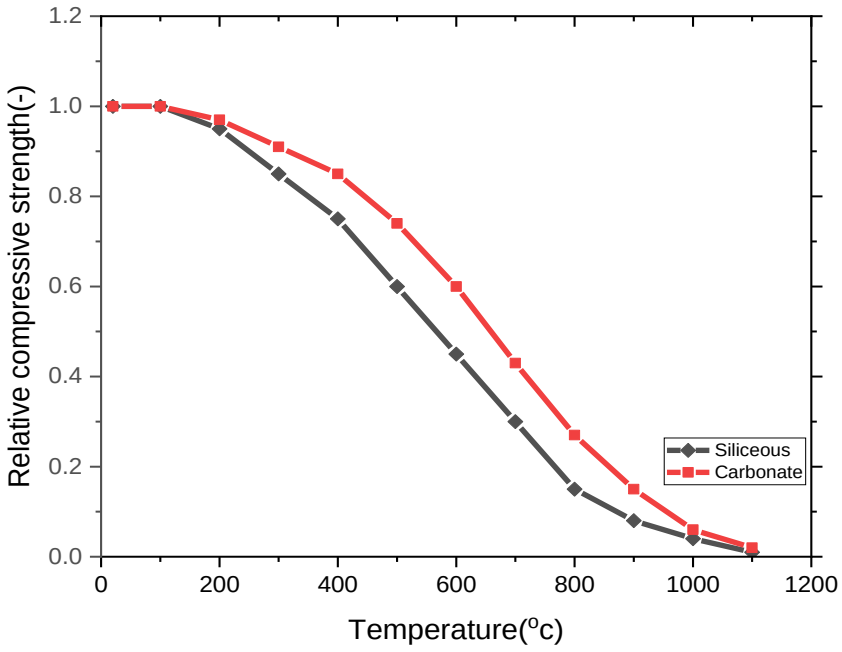

Figure 2.10: Variation of relative compressive strength of normal strength concrete as a function of temperature.

$$f_{ck,t}(T) = K_{c,t}(T) f_{ck,t} \tag{2.46}$$

$$K_{c,t}(T) = 1 \qquad for\ 20\ ℃ \leq T \leq 100\ ℃ \tag{2.47}$$

$$K_{c,t}(T) = 1 - \frac{1(T-100)}{500} \quad for\ 100\ ℃ < T \leq 600\ ℃ \tag{2.48}$$

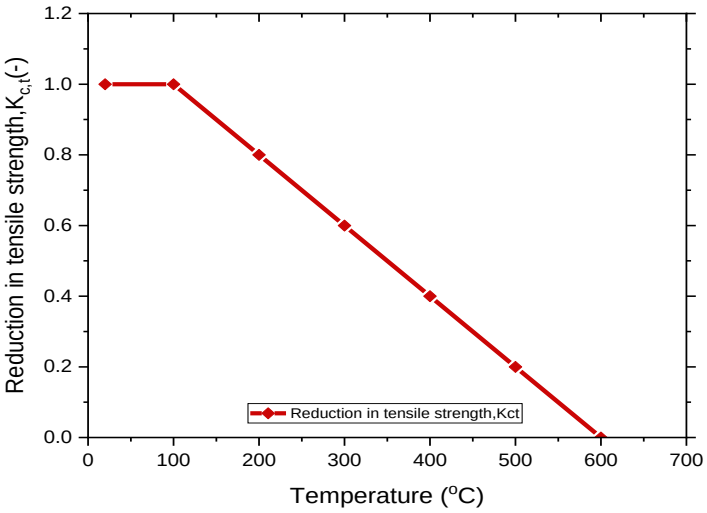

Figure 2.11: Reduction coefficient for tensile strength of concrete at elevated temperatures

2.11.2.3 Elastic modulus

The elastic modulus of concrete is the measure of its stiffness or resistance to deformation and in reinforced concrete structure it is extensively used in the analysis of stresses, moments, and deformation. Since the response of the stress-strain curve of the concrete is nonlinear the elastic modulus of concrete is obtained by initial tangent modulus, secant modulus, or tangent modulus method(Krishna et al., 2019b). The elastic modulus of the concrete can be affected by various variables such as mixing, water-cement ration, quantity and nature of aggregates, age of concrete, and nature of conditioning(V. Kodur, 2014a). At elevated temperatures, the elastic modulus of concrete rapidly decreases as the temperature rises (see figure 2.12).

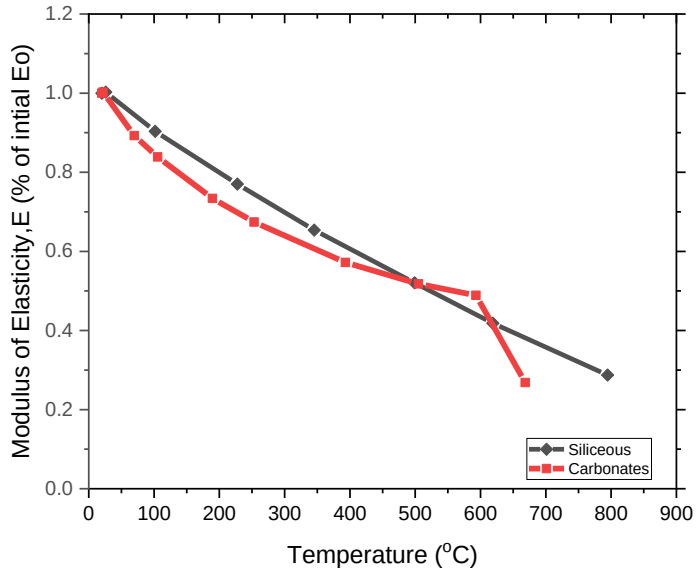

Figure 2.12: Variation of elastic modulus of concrete with temperature

2.11.2.4 Stress-Strain response

This section reviews the existing relationship on temperature-dependent stress-strain properties of concrete from literature review(V. K. R. Kodur et al., 2004; Krishna et al., 2019b) and code of standard(ASCE, 1992; EN 1991-1-2, 2011). Most of the existing constitutive models focus on the relationship between stress-strain curves with compressive strength of concrete, strain at peak stress, and ultimate strain. (Krishna et al., 2019a) develop a stress-strain response of the concrete at elevated temperature. The stress-strain curve decrease with increased temperature since the compressive strength of concrete decrease as temperature rises. The compressive strength of the concrete has a major influence on the stress-strain of concrete at elevated temperature, especially above 500 °C at which the strain at peak stress reaches four times the strain at ambient temperature. the model developed by (Krishna et al., 2019a) did not consider types of aggregates that have a significant effect on the compressive strength of concrete and it is applicable for only normal strength concrete. This is one of the basic limitations of the model.

The North American code of standard(ASCE, 1992) model for stress-strain takes into account the effect of aggregate types(carbonate and siliceous aggregates) and (V. K. R. Kodur et al., 2004) develop the model by modifying the ASCE equation for high strength concrete (ASCE, 1992). Both models together provide the stress-strain relationship at elevated temperature for normal and high strength concrete. However, they do not identify concrete aggregate types separately. Furthermore,(ASCE, 1992; V. K. R. Kodur et al., 2004) implicitly consider the creep strain of concrete deformation in the mechanical strain of the concrete.

There is also another model that estimates the uniaxial compressive stress-strain of concrete at elevated temperature(EN 1991-1-2, 2011). Similar to North American models, the European models have similar trends of the stress-strain curve that is as temperature rises, a significant decrease in peak stress, and a large increase in strain. Unlike the North American model(ASCE, 1992), the Eurocode 2(EN 1991-1-2, 2011) considers three types of aggregate types for normal strength concrete(light-weight, carbonates, and siliceous aggregates). Similar to(ASCE, 1992; V. K. R. Kodur et al., 2004), the Eurocode 2 accounts for the effect of creep strain of concrete at elevated temperature implicitly into mechanical strain. Figure 2.13 shows the stress-strain curve relationship for concrete under uniaxial compression at an elevated temperature accord-

ing to Eurocode 2(EN 1991-1-2, 2011) with all parameters illustrated in the figure as a function of concrete temperatures are given in table 2.1.

$$\sigma(T) = \frac{3 * \varepsilon * f_{c,T}}{\varepsilon_{c1,T}\left(2 + \left(\frac{\varepsilon}{\varepsilon_{c1,T}}\right)^3\right)} \qquad \varepsilon \leq \varepsilon_{c1,T} \qquad (2.49)$$

$\varepsilon_{c1,T} < \varepsilon \leq \varepsilon_{cu,T}$ For the numerical purpose, a descending branch should be adopted

A linear or nonlinear model are permitted

Therefore, in this study a linear descending branch of the compressive stress-strain of concrete at elevated temperature were adopted in finite element modeling following the reduction according the Eurocode specified in table 2.1.

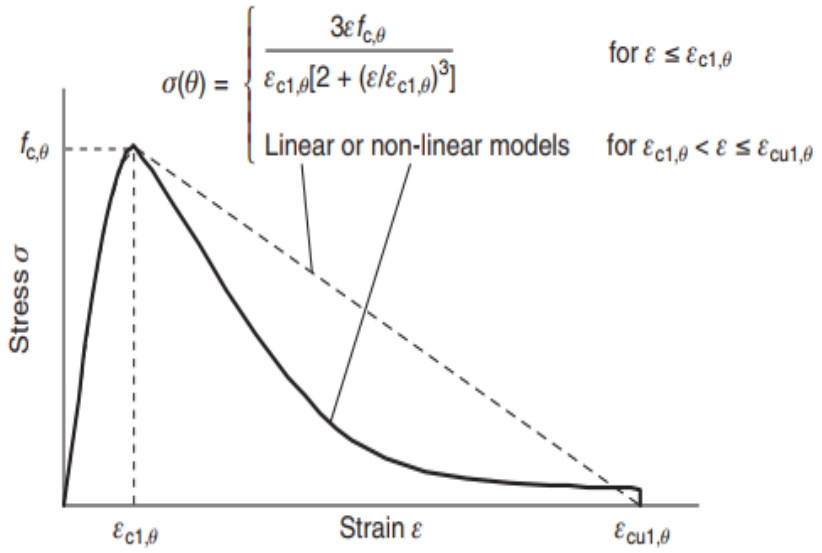

Figure 2.13: stress-strain relation of concrete under compression at elevated temperatures

2.11.2.5 Strain at peak stress and ultimate strain

i) Strain at peak stress

Unlike the elastic modulus of the concrete, the strain at peak stress constitutive models is either given as explicit equations of temperature (ASCE, 1992) or tabulated based on temperature (EN 1991-1-2, 2011) see table 2.1. At ambient temperature, the strain at peak stress, $\boldsymbol{\varepsilon}_{cm}$ models had approximately similar values with a minor difference in increasing the strain at peak stress with increased temperatures. The Eurocode model assumes the strain at peak stress $\varepsilon_{cm} = 0.0025$ at ambient temperature and the ASCE

Table 2. 1: Parameters used in this study for the stress-strain relationship of normal-weight at elevated temperatures

	Siliceous NWC			Calcareous NWC		
Temperature T(°C)	$\frac{f_{c,T}}{f_{ck}}$	$\varepsilon_{c1,T}$	$\varepsilon_{cu,T}$	$\frac{f_{c,T}}{f_{ck}}$	$\varepsilon_{c1,T}$	$\varepsilon_{cu,T}$
20	1.00	0.0025	0.0200	1.00	0.0025	0.0200
100	1.00	0.0040	0.0255	1.00	0.0040	0.0225
200	0.95	0.0550	0.0250	0.97	0.0055	0.0250
300	0.85	0.0070	0.0275	0.91	0.0070	0.0275
400	0.75	0.0100	0.0300	0.85	0.0100	0.0300
500	0.60	0.0150	0.0325	0.74	0.0150	0.0325
600	0.45	0.0250	0.0350	0.60	0.0250	0.0350
700	0.30	0.0250	0.0375	0.43	0.0250	0.0375
800	0.15	0.0250	0.0400	0.27	0.0250	0.0400
900	0.08	0.0250	0.0425	0.15	0.0250	0.0425
1000	0.04	0.0250	0.0450	0.06	0.0250	0.0450
1100	0.01	0.0250	0.0475	0.02	0.0250	0.0475
1200	0.00	0.00	0.00	0.00	0.0 0.00	

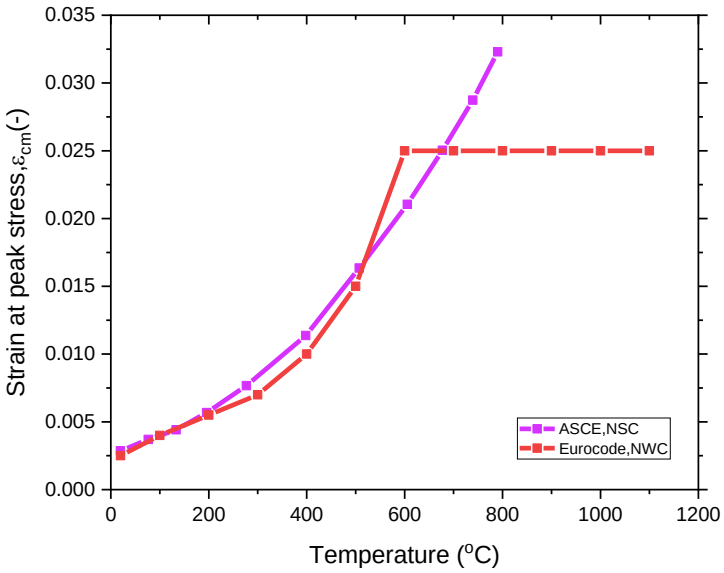

Figure 2.14: Variation with the temperature of strain at peak stress

(ASCE, 1992) models assume the ambient temperature of the strain at peak stress around ε_{cm} = 0.0026. The temperature-dependent strain at peak stress of normal strength concrete, ε_{cm}, as asper North American Code (ASCE, 1992) and Eurocode (EN 1991-1-2, 2011) are presented in figure 2.14. It indicates that above 600 ^{o}C the strain at the peak stress of the concrete remains constant, ε_{cm} = 0.025 in the Eurocode model while in the ASCE model it linear increases.

ii) Ultimate strain

The Eurocode model (EN 1991-1-2, 2011) gives the explicit of the ultimate strain of the concrete in the form table depending on variation with the temperature (see table 2.1). However, the ASCE model (ASCE, 1992) does not provide any explicit relationships of the ultimate strain of the concrete with the variation of the temperature. In the manual, the ASCE (ASCE, 1992) addresses how to determine the ultimate strain of the concrete concerning the maximum stress; that is assuming 85% of the strain at peak stress from the stress-strain relationship. The temperature-dependent ultimate strain of normal strength concrete, ε_{cu}, as asper North American Code (ASCE, 1992) and Eurocode (EN 1991-1-2, 2011) are illustrated in figure 2.15. It can be observed from figure 2.15 that the two models result in a very large difference in the ultimate strain of the concrete with the variation of the temperature. According to the ASCE model, the room temperature of the ultimate strain of the concrete ε_{cu} = 0.006, and the Eurocode assume ε_{cu} = 0.02. This difference is since the Eurocode model implicitly included the creep strain into the constitutive model of stress-strain relationship shown in figure 2.13.

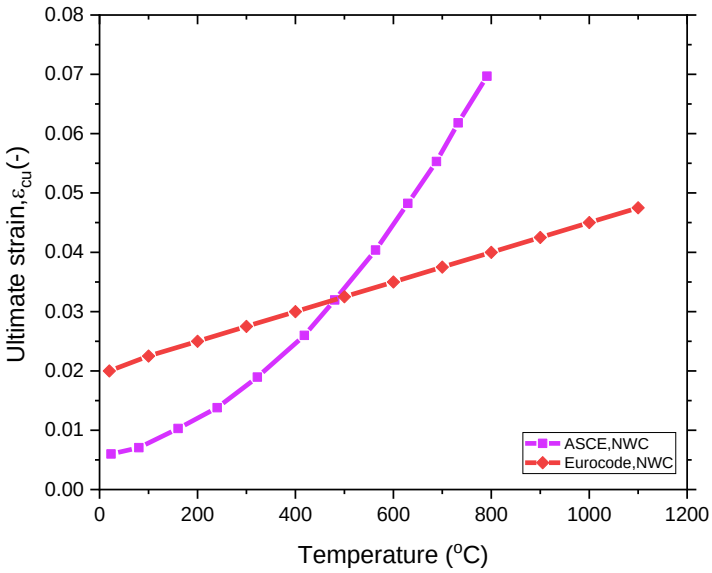

Figure 2.15: Variation with the temperature of ultimate strain

2.11.2.6 Deformation properties of concrete at elevated temperature

The deformation properties of concrete at elevated temperature depend on the thermal expansion, creep strain, and transient strain which is affected by chemical composition, aggregate types, and chemical and physical reaction when the concrete is exposed to heating (Schneider, 1988).

2.11.2.7 Thermal expansion

When concrete undergoes an elevated temperature it can be expanded. This expansion of the concrete is measured through the coefficient of thermal expansion which is the most important parameter that affects the performance of concrete under fire conditions (Ghannam, 2019). Figure 2.16 illustrates the variation of normal weight concrete with temperature according to Eurocode. (EN 1992-1-2, 2011) consider the influence of types of aggregate on the variation of thermal expansion of concrete with temperature. The concrete made of siliceous aggregate has a higher thermal expansion than carbonate aggregates. But,(ASCE, 1992) accounts for only one variation of the thermal strain of concrete with temperature and develops the equation of linear thermal expansion coefficient of concrete at elevated temperature. Therefore, in this study, the equation developed for thermal expansion of concrete with temperature as per ASCE is used to implement the material properties of concrete into finite element software ABAQUS during stress analysis.

The thermal strain or expansion of concrete $\varepsilon_{c,\theta}$ according to Eurocode (EN 1991-1-2, 2011) can be evaluated by:

For siliceous aggregates:

$$\varepsilon_{c,\theta}=\begin{bmatrix}-1.8*10^{-4}+9*10^{-6}T+2.3*10^{-11}T^{3}\ for\ 20℃\leq T\leq 700℃\\ 14*10^{-3} \qquad\qquad for\ 700℃<T\leq 1200℃\end{bmatrix} \tag{2.50}$$

For calcareous aggregates:

$$\varepsilon_{c,\theta}=\begin{bmatrix}-1.2*10^{-4}+6*10^{-6}T+1.4*10^{-11}T^{3}\ for\ 20℃\leq T\leq 700℃\\ 12*10^{-3} \qquad\qquad for\ 700℃<T\leq 1200℃\end{bmatrix} \tag{2.51}$$

The linear coefficient of thermal expansion of concrete according to North American Standard (ASCE, 1992) expressed by equation 2.52

For both siliceous and carbonate aggregate concretes

$$\alpha=(0.008T+6)\times 10^{-6} \tag{2.52}$$

For expanded shale aggregate concrete

$$\alpha = 7.5 \times 10^{-6} \tag{2.53}$$

Where T is the concrete temperature (°C)

2.11.2.8 Creep and transient strain

At elevated temperatures under compressive stresses, time-dependent deformations in concrete, such as creep and transient strains, are greatly enhanced (Kong & Kaplan, 1991). Moisture movement out of the concrete matrix causes creeps in concrete to increase at high temperatures. Moisture dispersal and bond loss in cement gel magnifies creep in concrete. As a result, the creep process is primarily caused and accelerated by two processes: (i) moisture movement and dehydration of concrete as a result of high temperatures, and (ii) acceleration in the bond breakage process (V. Kodur, 2014a). According to a review of the literature, there is a lack of recent information on creep

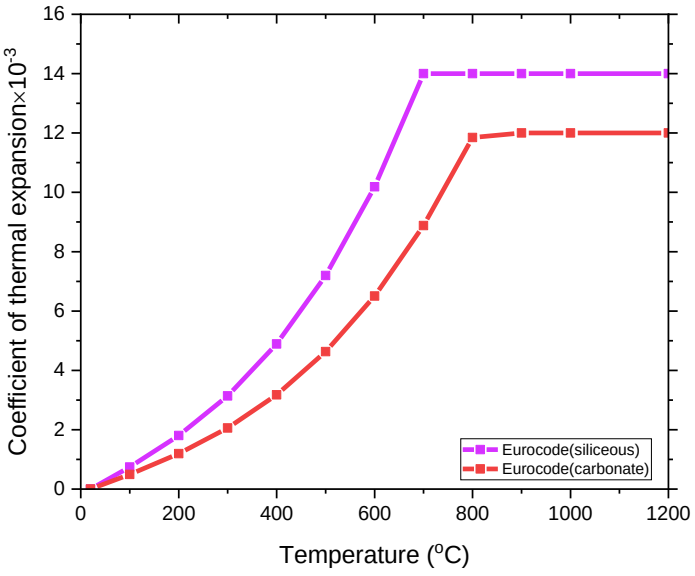

Figure 2.16: Variation of thermal expansion of normal weight concrete with temperature

And transient strain in concrete at elevated temperatures. The work of (Asamoto et al., 2006; Meyers, 1972) provides some data on the creep of concrete at elevated temperatures.(Anderberg & Thelandersson, 1976)perform experimental tests to evaluate transient and creep strains at high temperatures. The result indicates that predried specimens with load stress levels of 45% and 67.5 % were less prone to deformation in the "positive direction" (expansion) under load. At 22.5% preload, there was no significant difference in strains. They also examine the effect of water saturation had a small change,

except for free thermal expansion (0% preload), which was found to be less for water-saturated specimens.

Schneider,(1988) also, investigate the effect of various parameters on the impact of transient and creep restraint on concrete deformation. The transient test for measuring total deformation or restraint of concrete has the strongest relationship to building fires and is supposed to provide the most realistic data with direct relevance to fire. The study's key findings are that (i) water to cement ratio and original strength have little influence on creep deformations under transient conditions, (ii) aggregate to cement ratio has a large influence on strains and critical temperatures: the harder the aggregate, the lower the thermal expansion, and thus total deformation in the transient state; and (iii) curing conditions are very important in the 20–300 ^{o}C range: Lower transient and creep strains are observed in air-cured and oven-dried specimens compared to water-cured specimens.

Constitutive models for creep and transient strains in concrete at elevated temperatures were developed by (Anderberg & Thelandersson, 1976) which can be formulated by following equations 2.54 and 2.55 for creep and transient strain at high temperatures.

$$\varepsilon_{cr} = \beta_1 \frac{\sigma}{f_{c,T}} \sqrt{t} e^{d(T-293)} \tag{2.54}$$

$$\varepsilon_{tr} = K_2 \frac{\sigma}{f_{c,20}} \varepsilon_{th} \tag{2.55}$$

Where ε_{tr} =thermal strain, β_1=6.28*10^{-6} s$^{-0.5}$, d=2.658*10^{-3}K^{-1}, T= concrete temperature (^{o}K) at time t(s), $f_{c,T}$=concrete strength at temperature T, σ = stress in the concrete at current temperature, K_2 = constant range from 1.8 to 2.35, ε_{cr} = creep strain, and $f_{c,20}$= concrete strength at room temperature.

Generally, in terms of transient creep strain, in the current Eurocode 2 (EN 1992-1-2, 2011) model there are no explicit terms for transient creep strain but it is implicitly in the mechanical strain term. Therefore, in this study during the numerical analysis of concrete bridge decks in fire, the effect of creep and transient strain of the concrete explicitly implemented into the finite element model is neglected.

2.12 Constitutive material models of GFRP at elevated temperatures

The time-dependent thermal (mass or density, specific heat, and thermal conductivity) and mechanical (modulus of elasticity, thermal strain, and strength) properties of GFRP

are needed to study the post-fire performance of GFRP at elevated temperatures. The thermal properties evaluate the temperature rise and associated temperature evaluations that develop within the section, whereas mechanical properties determine the degree of fire-induced degradation in capacity and stiffness of the structural member. Deformation properties control the degree of deformation in concrete members containing FRP. Temperature-dependent thermal, mechanical, and deformation properties of concrete(Krishna et al., 2019a) and steel (Saafi, 2002)have been extensively reviewed in the literature. however, constitutive or empirical relationships defining the temperature variation of these properties at elevated temperature are also not addressed in different codes of standards, such as(ASCE, 1992; EN 1992-1-2, 2011). Furthermore, there is no empirical equation regarding the temperature variation with the properties of FRP at elevated temperatures. Therefore, in this section different thermal and mechanical properties of GFRP at the elevated temperature used in this study, based on the experimental investigation from published works of literature are discussed.

2.12.1 Thermal properties of GFRP at elevated temperature

2.12.1.1 Mass or density of FRP

The density of the FRP material remains constant before the decomposition of its polymer matric. As the decomposition of the polymer matric begins; the molecular bond between the polymer matric or thermoset is broken and the polymer materials react with gas and char which brings to a reduction in mass or loss of mass (Correia, Bai, & Keller, 2015). According to (T. Keller et al., 2005) conducted an experimental investigation on pultruded E-glass/polyester composite through thermomechanical analysis to determine the reduction in weight loss from room temperature to 550 ^{o}C under various heating rates, the reduction in mass occurs as illustrated in figure 2.17. From the graph, the decomposition temperature (T_d) of GFRP determined by thermal gravimetric analysis (TGA) is 300 ^{o}C at a uniform rate of heating considering 5% weight loss with 115 ^{o}C glass transition temperature. However, at different heating rates; there are different values of decomposition of temperature, that is, the higher rate of heating produces high decomposition of temperature at the same temperature. This is due to the kinetic mechanism of the decomposition reaction which is explained in (Thomas & Yu, 2007).

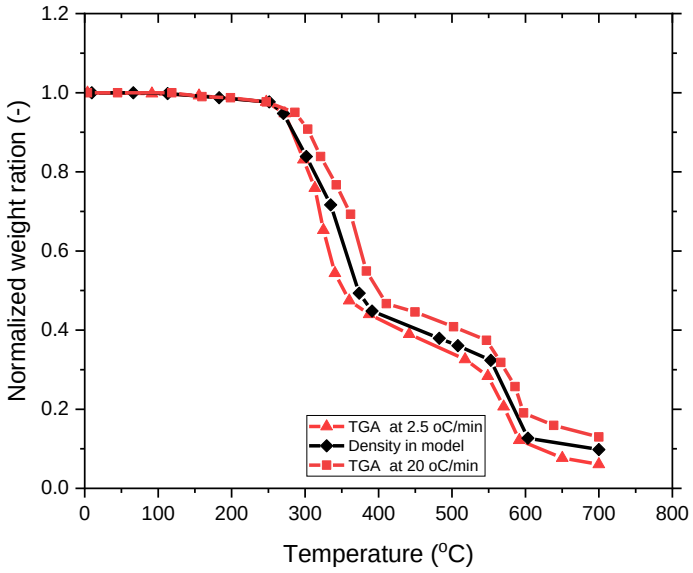

Figure 2.17: Reduction in weight loss of pultruded GFRP as a function of temperature at 2.5 and 20 °C/min rate of heating (Correia, Bai, & Keller, 2015)

2.12.1.2 Thermal conductivity of FRP

The thermal conductivity of FRP composite material at elevated temperature is dependent on the characteristics of constituent material(Correia, Bai, & Keller, 2015; Thomas & Yu, 2007) such as fibers and resin with their contents, forms, and structures. At room temperature, the thermal conductivity of pultruded GFRP can be measured by the hot plate method in which the thermal conductivity of pultruded GFRP is a combination of the thermal conductivities of the fibers and resin (i.e., the constituents' properties) and their volume fractions, geometric properties and morphology (i.e., size, shapes, orientations) as well as any voids between them(Correia, Bai, & Keller, 2015). For that, the time temperature-dependent thermal conductivity of fibers and resins are evaluated first, and then the properties of the composite can be determined.

According to (Thomas & Yu, 2007) also the best way to evaluate the thermal conductivity of FRP material properties at elevated temperature is accounting for the behavior of FRP material at the stage of undecomposed and decomposed. Figure 2.18 illustrates, at room temperature the thermal conductivity of fully decomposed material is less than virgin material. For decomposed material, the thermal conductivity of material rise with temperature while for virgin material as decomposition occurs it is effective thermal conductivity is reduced(Bai, Keller, et al., 2008)

In general, the thermal conductivity of pultruded GFRP at room temperature needs significant research efforts and several theoretical models for prediction purposes. Since

from the literature reviewed there is no analytical equation developed to determine the variation of thermal conductivity of pultruded GFRP with temperature like steel structure. However, there are some models. The simplest model was developed by (Thomas & Yu, 2007) based on the rule of mixtures and inverse rule of mixtures, as given in equations (2.56) and (2.57), respectively. This model represents the thermal conductivity of composite material, accounting for the effective thermal conductivity of material with decomposed (undecomposed) and volume fraction of decomposed (undecomposed).

$$K_c = V_b K_b + V_a K_a \tag{2.56}$$

$$\frac{1}{K_c} = \frac{V_b}{K_b} + \frac{V_a}{K_a} \tag{2.57}$$

Where K_c is the thermal conductivity of the composite material overall temperature V_b (V_a) is the volume fraction of undecomposed (decomposed) material, K_b (K_a) is the thermal conductivity of undecomposed (decomposed) material.

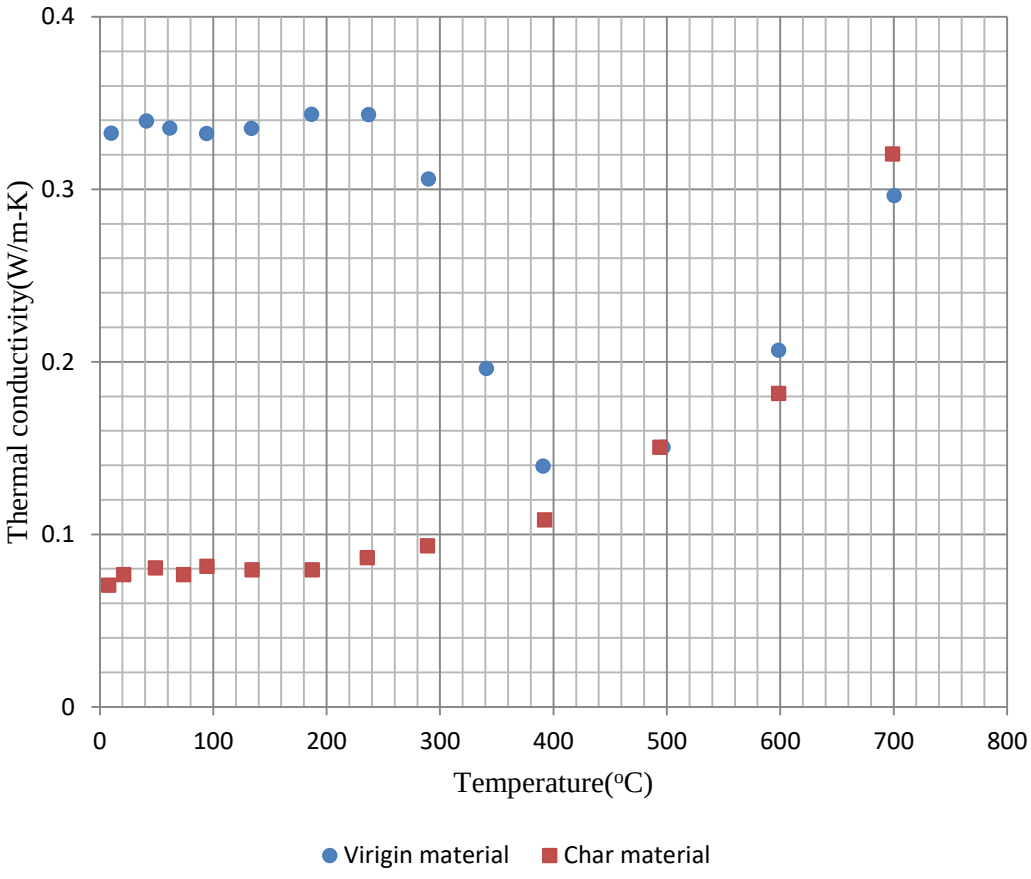

Figure 2.18: Temperature-dependent effective thermal conductivity on virgin and char material from hot disk experiment.

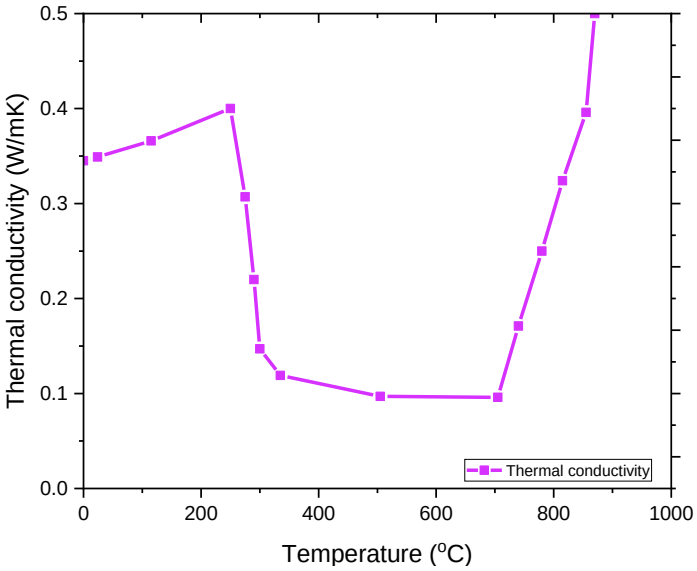

Figure 2.19: Temperature-dependent thermal conductivity of pultruded GFRP.

2.12.1.3 Specific heat capacity

The specific heat capacity of a pultruded FRP material at room temperature can be measured using a calorimetry method that examines a relatively large piece of a specimen. Temperature can be measured directly using differential scanning calorimetry (DSC), which uses a small amount of material, typically in powder form(Correia, Bai, & Keller, 2015). Experimental investigation shows that excluding moisture evaporation, the specific heat capacity of typical pultruded GFRP composites increases only to a small degree with temperature before decomposition of material(Henderson et al., 1982). When decomposition (an endothermic reaction) occurs, additional heat is needed to break the molecular bond in chains. This results in a significant increase in the measurement of specific heat capacity during the decomposition process, as shown in Figures 2.20, and 2.21 illustrates the thermal properties of FRP across the glass transition and decomposition of the material. Because it expresses the total energy required for all physical and chemical changes, the resulting measured value is often referred to as effective specific heat capacity. As a result, rational modeling of effective specific heat capacity can be established by combining the material-specific heat capacity (described by physical theory, such as Debye's or Einstein's models) with the decomposition heat (described by Arrhenius kinetic equations), as presented in(Thomas & Yu, 2007).

Figure 2.21 illustrates the specific heat capacity of the pultruded GFRP obtained via calorimetry is around 1170 J/Kg-K at room temperature and it is used in this study dur-

ing heat transfer analysis. The minor variations of the true specific heat curve were negligible in comparison to the magnitude of the peaks due to dehydration and decomposition, so the curve was idealized as a constant value except in the ranges of boiling (90 ^{o}C to 110 ^{o}C) and resin decomposition (250 ^{o}C to 600 ^{o}C).

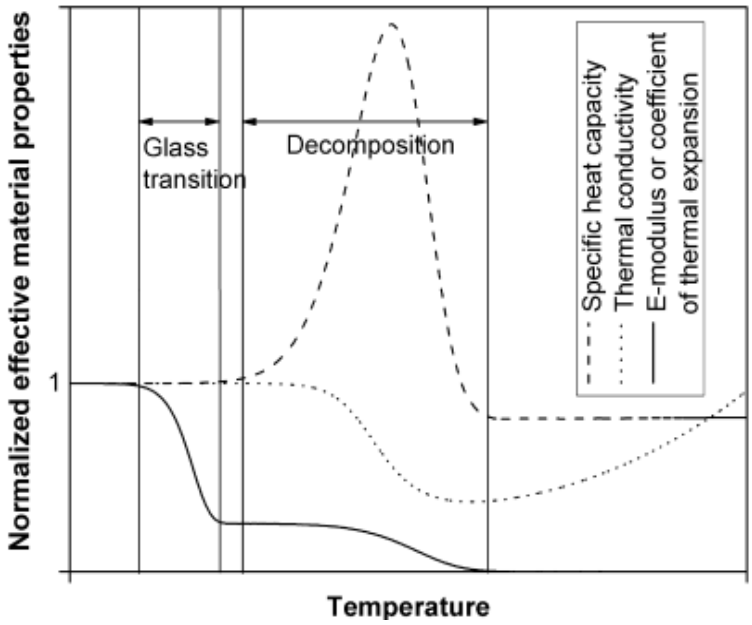

Figure 2.20: Variation of thermal and mechanical properties of FRP material along with glass transition and decomposition

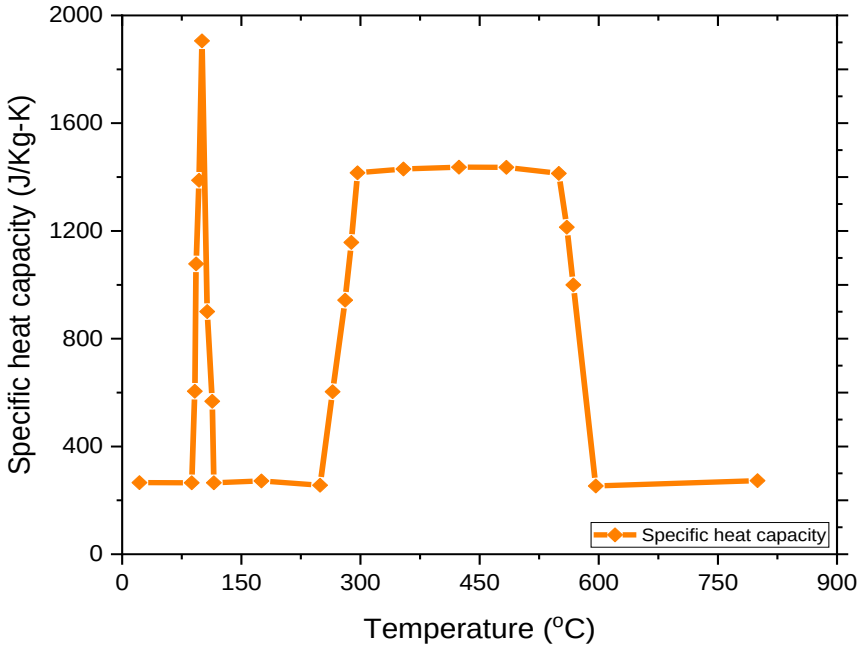

Figure 2.21: Temperature-dependent effective specific heat capacity of pultruded GFRP at elevated temperature

2.12.2 Mechanical properties of GFRP at elevated temperatures

At elevated temperature's the Glass fibers alone can attain their mechanical properties while most polymer resins have less capability of temperatures. When the temperature exceeds the glass transition (T_g) temperature of the material, the time-temperature dependent mechanical properties like tensile strength, compressive strength shear modulus, and modulus of elasticity decrease with an increase in temperature since the composite action between fibers and resins rapidly deteriorate (Correia et al., 2013). This reduction in mechanical properties of GFRP composites results in loss of strength and stiffness. Therefore in this section, the mechanical properties of GFRP at elevated temperature and standardized tests are used to determine these properties at room temperature when it is subjected to various types of loading, like, tension, compression, or shear are discussed.

2.12.2.1 Elastic modulus of GFRP at elevated temperature

The elastic modulus of pultruded GFRP can be obtained through dynamic mechanical analysis (DMA) in which the specimens are loaded in sinusoidal load path within the elastic state of their stress-strain curve and the temperature is relatively small variation at a uniform rate of heating(Bai, et al., 2008). As illustrated in figure 2.22, the degradation in elastic (storage) modulus has two distinct stages that correspond to the material's glass transition and decomposition processes. As a result, the T_g is critical for GFRP composite materials in civil engineering applications due to the significant reduction in modulus (and strength) that occurs during this process. (Post, et al., 2008) perform an experimental investigation on temperature-dependent thermophysical and mechanical properties of pultruded GFRP composites. The result found that the storage modulus of composites reduced with the rise in temperature and both directions along the pultrusion process and transverse directions the pultruded GFRP specimen shows the same temperature mechanical properties.

There are no codes of standards that formulate the analytical equation of the reduction in elastic modulus of FRP at elevated temperatures. However, there are numerous scholars and codes of building standards are formulate analytical expression for steel (ASCE, 1992; EN 1991-1-2, 2011). Because of this, in this study data gathered from literature was used for finite element input. Based on collected data on the reduction of mechanical properties of FRP rebar from literature according to (Saafi, 2002) the modulus of the FRP rebar remains constant up to the temperature of 100 ^{o}C and decreased

linearly as the temperature increases. The value of the reduction in modulus of FRP rebar with room temperature can be obtained from the following equation 2.58, and it is variations with elevated temperatures were determined by equation 2.59 to 2.61

$$K_E = \frac{E_{fT}}{E_{f20℃}} \tag{2.58}$$

Where K_E temperature reduction factor for modulus of elasticity,$E_{f20℃}$ and E_{fT} are the elastic modulus of FRP rebar at 20 ºC and T ºC respectively.

GFRP and AFRP

$$\begin{bmatrix} K_E = 1 & for\ 0 \le T \le 100 \\ K_E = 1.25 - 0.0025T & for\ 100 \le T \le 300 \\ K_E = 2 - 0.005T & for\ 300 \le T \le 400 \\ K_E = 0 & for\ 400 \le T \end{bmatrix} \tag{2.59}$$

CFRP

$$\begin{bmatrix} K_E = 1 & for\ 0 \le T \le 100 \\ K_E = 1.175 - 0.00175T & for\ 100 \le T \le 300 \\ K_E = 1.625 - 0.00325T & for\ 300 \le T \le 500 \\ K_E = 0 & for\ 500 \le T \end{bmatrix} \tag{2.60}$$

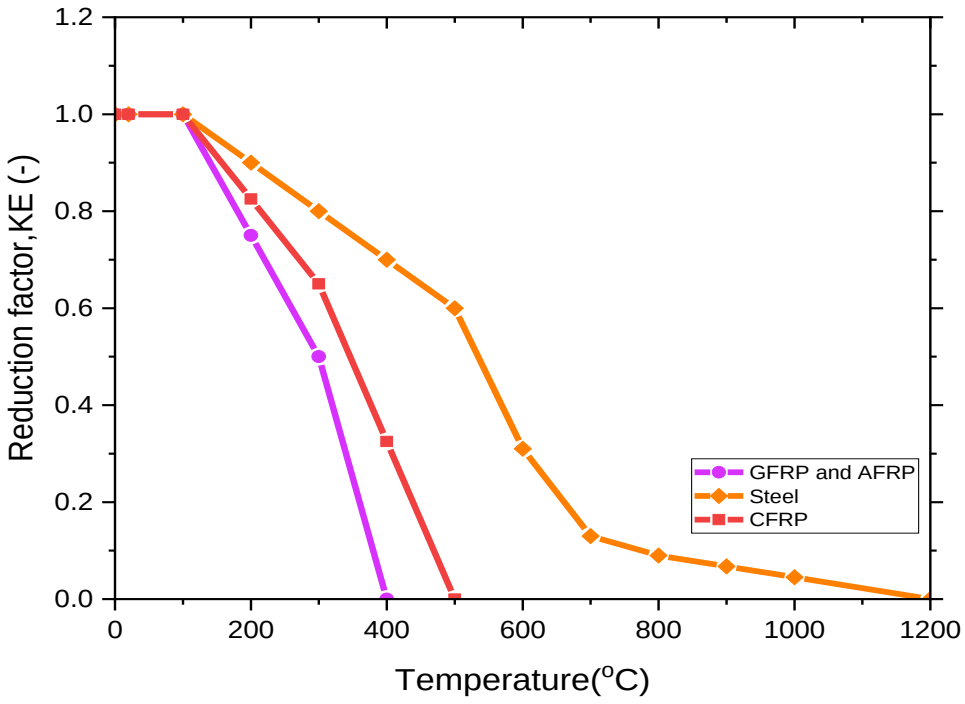

Figure 2.22: Reduction in factor of elastic modulus of CFRP, GFRP, and steel with variation in temperature

$$K_f = \frac{f_{fuT}}{f_{fu20℃}} \tag{2.61}$$

2.12.2.2 Strength of pultruded GFRP at elevated temperature

The glass transition process that the polymer matrix undergoes, as well as the resulting degradation of its mechanical properties, results in a significant reduction in the strength of pultruded FRP composites. Figure 2.23 to 2.25 depicts the strength of pultruded GFRP materials in tension, shear, and compression for the temperature ranges from room temperature 20 ^{o}C to 250 ^{o}C normalized to the room temperature from different literature and are used in finite element input in this study during simulation of fire resistance GFRP SIP concrete bridge decks under fire.

Correia et al., (2015) reviewed that the tensile strength of pultruded GFRP at ambient temperature is dominated by the fiber. This can be true only at elevated and high temperatures if the polymer resin can efficiently transfer stresses between discontinuous fibers. Also, Extensive studies have been conducted by (Correia et al., 2013) on strength properties (tensile, compressive, and shear strength) of pultruded GFRP at elevated temperatures. The experimental result indicates that in the range of the temperature 20 ^{o}C to 250 ^{o}C the pultruded GFRP is more endangered under shear and compression than tension. The Tensile strength of pultruded GFRP exposed to high temperatures significantly reduced, however, at 220 °C, the material retains approximately 54% of its ambient temperature strength. Shear and compressive strengths were extremely decreased at elevated temperatures, with strength retentions of only 11% and 5%, respectively, when compared to the strength at room temperature.

Bai and Keller,(2009) conducted an experimental investigation on modeling of strength reduction of temperature-dependent pultruded GFRP subjected to fire. The model is developed based on the rule and inverse rule of mixture, in which the composite material at a certain temperature is obtained knowing the proportion of the composite material in the mixture. The rule of the mixture can accurately determine the reduction in strength of GFRP with temperature. The result concludes that the proposed modeling can predict accurately the mechanical response of compressive strength, shear strength, and elastic modulus of the composite material subjected to thermal loading, and it can be used for finite element input. Therefore in this study for further parametric study and numerical model validation, the work of (Bai and Keller,2009) was used.

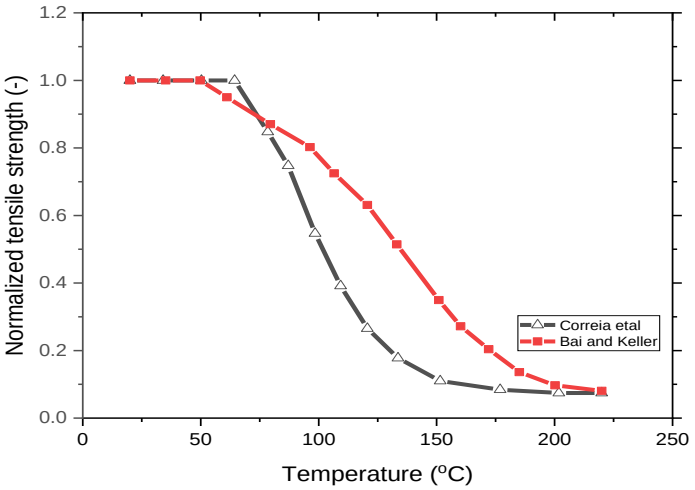

Figure 2.23: Normalized tensile strength of pultruded GFRP with temperature

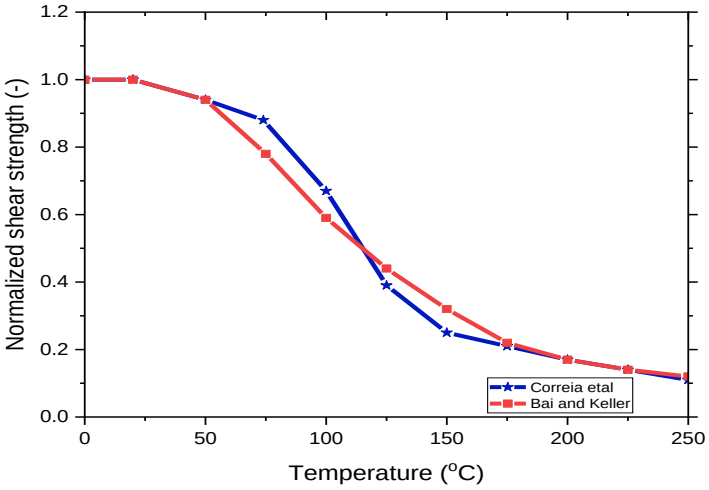

Figure 2.24: Normalized shear strength of pultruded GFRP with temperature

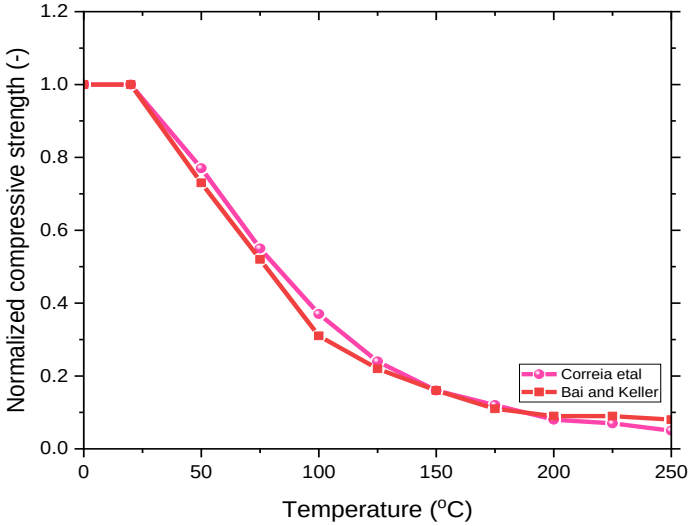

Figure 2.25: Normalized compressive strength of pultruded GFRP with variation in temperature

2.12.3 Deformation properties of FRP at elevated temperature

2.12.3.1 Coefficient of thermal expansion of FRP

The coefficient of thermal expansion of GFRP composite experimental determined in the same way to thermophysical properties of GFRP at elevated temperature using standard test or based on the rule of mixture(Karadeniz & Kumlutas, 2007). The American Concrete Institute (ACI), a guide for the design and construction of structural concrete reinforced with fiber-reinforced polymer (ACI 4401.1R-15, 2015) reported the thermal expansion coefficient of GFRP rebar to vary along its longitudinal and transverse direction based on types of fiber, resin, and volume fraction of fiber. The longitudinal coefficient of thermal expansion of the GFRP rebar is dominated by fiber while its transverse direction is dominated by resin. According to this guide at room temperature, the coefficient of thermal expansion of GFRP varies from 6 to $10*10^{-6}/\ ^{o}C$ in the longitudinal direction and 21 to $23*10^{-6}/\ ^{o}C$ in the transverse direction. At elevated temperatures, there is limited information on the variation of thermal expansion of GFRP rebar with temperature. Consequently, in this study only the longitudinal thermal expansion coefficient of GFRP rebar is considered.

Furthermore, (Bai, Keller, et al., 2008) find the true value of the coefficient of thermal expansion of pultruded GFRP can be obtained based on the integration coefficient of fiber and matrix(micromechanics). As illustrated in figure 2.20 when the temperature above the glass transition of GFRP composites, its elastic modulus is significantly reduced and the thermal expansion coefficient follows the trends of the reduction in elastic modulus at elevated temperatures. As a result, the thermal expansion of GFRP above glass transition temperatures may not induce further stresses or deformation to another component. Therefore, the contributions of the true thermal expansion coefficient of the material after glass transitions to the global structural deformation are neglected. Due to this, for material above the glass transition of the glass state, the effective coefficient of thermal expansion is zero. Based on the true coefficient of thermal expansion of glass state is $12.6*10^{-6}/K$ in the longitudinal direction and temperature-dependent effective coefficient of thermal expansion can be analytically expressed by equation 2.48 (Tracy, 2005) and temperature-dependent thermal expansion coefficient of pultruded GFRP is illustrated in figure 2.26 below.

$$\lambda_{c,e} = \lambda_c * \left(1 - \alpha_g\right) \tag{2.62}$$

Where $\lambda_{c,e}$ the effective thermal coefficient, λ_c true thermal expansion and α_g conversion degree of glass transition

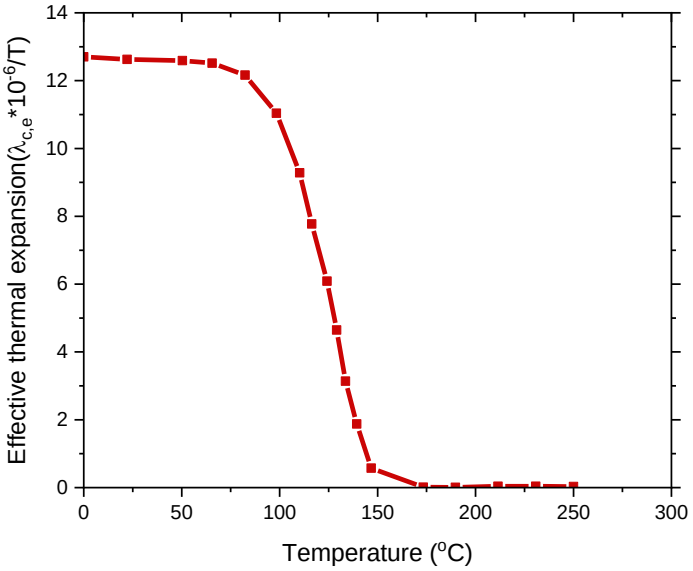

Figure 2.26: Temperature-dependent effective coefficient thermal expansion

2.13 Research gap

Many temperatures dependent material behavior and performance for reinforced concrete members have been investigated previously by scholars and researchers, but only very few such performance and behavior have been available for GFRP SIP formwork for concrete bridge decks under fire. Therefore, in this study, the existing literature on the post-fire performance of GFRP SIP formwork for concrete bridge deck at elevated temperature was reviewed and a well-documented database was presented.

The constitute material models are implemented into the finite element software to conduct numerical analysis of GFRP SIP formwork concrete bridge deck under fire by simultaneously heating and loading. Until now, there is no fire requirement approaches developed for GFRP reinforced structures unlike the design of reinforced concrete structures to meet the fire requirements which can be achieved via the prescriptive approach, which is dependent on analytical or laboratory testing. The methods do not require temperature-dependent material properties. The new international code of practices is moving towards numerical and performance-based fire design for structures, which require temperature-dependent material properties and the application of these properties to perform numerical analysis and design of structures under fire. Hence this research becomes important to full fill this gap of knowledge particularly with GFRP at elevated temperatures.

Fire design of structure based on experimental test takes an excessive time and is expensive. Therefore, fire design of structures must be performed using FE analysis as this would save time and resources. This study is carried out to conduct a numerical investigation on GFRP SIP formwork concrete bridge decks under fire. Using the performance-based approach with FE software; duration of fire exposure; fire type, sustained service load, aggregate type, GFRP plate length, GFRP plate thickness, deck width, span to depth ratio, and cooling and heating phase are taken into consideration, as these factors influence the performance of GFRP SIP concrete decks under fire. Through the verified FE model, the assessment of the post-fire performance of GFRP SIP formwork for concrete bridge decks exposed to fire conditions were investigated.

From the review of previous experimental and numerical studies, it can be seen that most of these have been limited to conventional steel and CFRP but there are limited studies concerning GFRP SIP forms. Therefore, this research was focused on GFRP under fire conditions at elevated temperatures. As reported by several researchers, GFRP is more vulnerable than CFRP under such conditions and loading. There are also uncertainties on strength of GFRP reinforcing bars due to a lack of knowledge on the assessment of the post-fire performance of GFRP at elevated temperatures (Hajiloo & Green, 2018b, 2019). The flexural strengthening mechanism of fire-damaged GFRP SIP formwork and performance of GFRP at elevated temperature warranted further investigation. No-load was applied during fire exposure, short duration of fire exposure (pool fire) is applied which cannot represent the behavior of GFRP at elevated temperature, and variables that affect the fire resistance of the deck were not considered during the study(Nicoletta et al., 2019). Additional mechanical and bond performance of FRP strengthening systems at high temperature, the effect of varying the duration of exposure to high temperatures that is, thermal aging, and effect of sustained load during and after thermal exposures are addressed issues for further investigation(Foster et al., 2008).

CHAPTER 3
MATERIALS AND METHODS

3.1 General

An experimental investigation needs a great amount of cost and time to conduct an experimental test on the post-fire performance of the concrete bridge deck. As a result, finite element modeling and simulation of fire have a powerful and interesting computational tool for complicated nonlinear analysis of concrete bridge decks subjected to different fire scenarios. Therefore, in this study due to the unavailability of testing machines and expensive costs, finite element software ABAQUS was used throughout this study. Particularly, the behavior of GFRP SIP formwork concrete bridge deck subjected to simultaneously heating and loading is very complex and several parameters that influence its fire performance were not further investigated (Nicoletta et al., 2019). Because of this, the nonlinear finite element analysis has become much needed to investigate further on fire performance of concrete bridge decks.

In this section, the material used and methodology followed in the present study are more described in detail. The main goal of this section is to present all important information and details to reach the result and discussion of nonlinear finite element analysis conducted in chapter four. This chapter includes material properties of concrete bridge deck components at room temperature from different literature-based manufacture data and model geometry used to validate the numerical model, introduction to ABAQUS software which briefly explain its application in the field of engineering, constitutive material models of concrete, GFRP, and pultruded GFRP at elevated temperature implemented into finite element model, loading and boundary condition, thermal and mechanical contact interface, finite element analysis and parametric calibration such as mesh sensitivity study, viscosity, and dilation angle.

3.2 Material and model geometry

3.2.1 Model geometry

Two 1,675 ×840 mm GFRP forms used in model validation each had four T-Up ribs spanning the full length of the forms spaced at 205 mm on center. Figure 3.1 shows a typical span of a bridge deck reinforced with the spliced GFRP formwork used in this study. The experimental program (Nicoletta et al., 2019) consisted of seven deck sections of a concrete bridge deck reinforced using a GFRP stay-in-place form. Figure 3.2

shows the cross-section detailing of the tested GFRP stay-in-place form decks. The total beam had a height including the GFRP base plate and width of 186mm and 205mm, 410mm, respectively. The total length of the beam specimens was 1675 mm having a variable exposed span length. The beams were reinforced with Φ10 mm GFRP bars. The longitudinal rebar was placed at 35mm from T-up ribs and the transverse bars are a lower rebar layer spaced at 185mm typical for all specimens.

Glass Fiber Reinforced Polymer (GFRP) thickness greater than 9.5 mm was used to make use of the fire resistance benefits associated with thermal thickness and select a GFRP structural form that was representative of a full-scale bridge deck in practice. The base plate has a maximum thickness of 19 mm, which is tapered to 13.7 mm away from the ribs. The ribs protruded 96 mm from the interior of the base plate to the top of the rib flange. The ribs are 12.7 mm thick, and their flanges are 102 mm wide(M. Nelson & Fam, 2013).

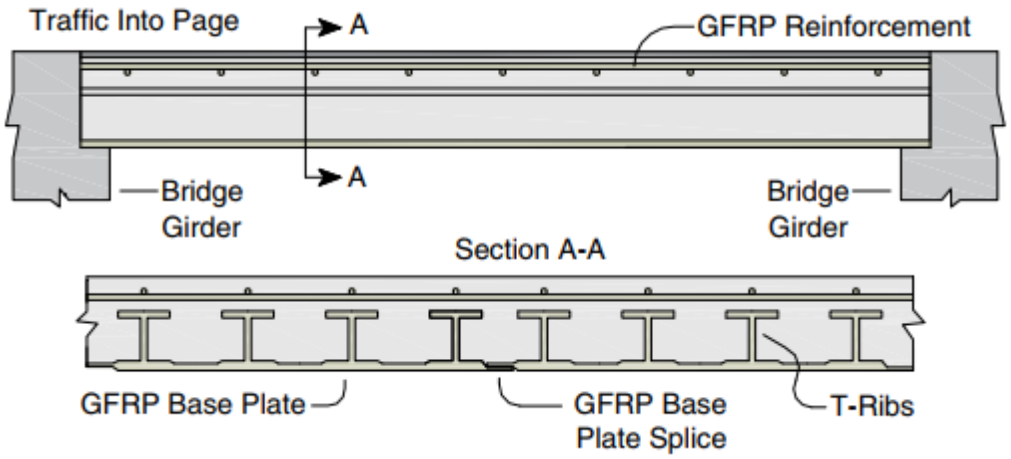

Figure 3.1: Typical configuration of GFRP stay in place T-up formwork [source :(Nicoletta et al., 2019)]

3.2.2 Material models at room temperature

According to ASTMC39 the beam and cylindrical test were covered with wet burlap during the curing. Based on the six cylindrical tests and taking their averages the 50 and 90 days of the compressive strength of the concrete is given as a table 3.1and to better represent the actual strip of a GFRP stay in place formwork concrete bridge deck a two-dimensional grid of 10-M GFRP V ROD of top rebar mesh was used only along with both directions. The longitudinal rebar was placed at 35mm from T-up ribs and the transverse bars are a lower rebar layer spaced at 185mm typical for all specimens having the following material properties.

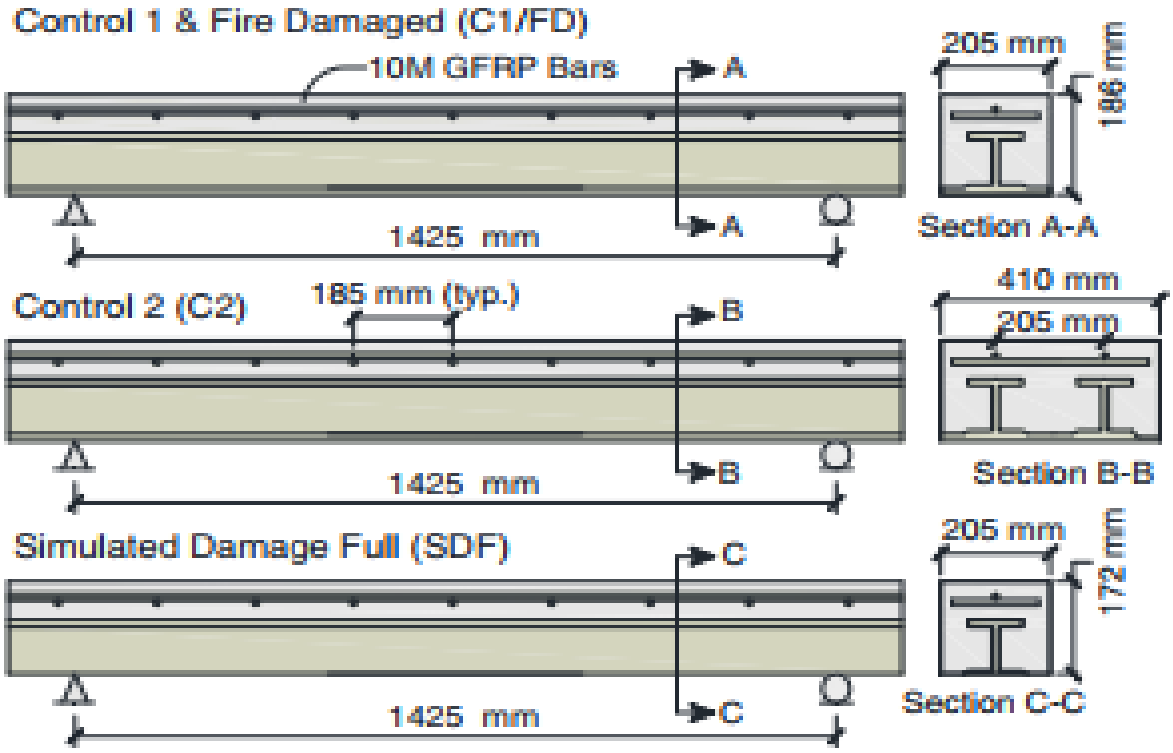

Figure 3.2: Dimension of concrete deck specimen [source :(Nicoletta et al., 2019)]

A12.7mm thick pultruded GFRP plate is were composed of alternating layers of longitudinal, transverse, and random mat E-glass fibers saturated with polyester resin. According to the manufacturer's data and code of standard the mechanical properties of GFRP rebar and pultruded GFRP at room temperature is listed in table below.

Table 3. 1: Lamina engineering constant of pultruded GFRP laminate

Mechanical properties		Sources
E_1 (GPa)	16.8	(Nicoletta et al., 2019)
E_2 (GPa)	15.6	(Nicoletta et al., 2019)
E_3 (GPa)	15.6	(Nicoletta et al., 2019)
G_{12} (GPa)	4.5	(Ayman et al., 2017)
G_{13} (GPa)	4.5	(Ayman et al., 2017)
G_{23} (GPa)	5.51	(Ayman et al., 2017)
V_{12}	0.25	(Ayman et al., 2017)
V_{13}	0.25	(Ayman et al., 2017)
V_{23}	0.3	(Ayman et al., 2017)

Table 3. 2: Lamina ultimate capacity of pultruded GFRP lamina

Mechanical properties		Sources
Longitudinal tensile strength (MPa)	203	(Nicoletta et al., 2019)
Longitudinal compressive strength (MPa)	110	(M. Nelson & Fam, 2013)
Transverse tensile strength (MPa)	126	(Nicoletta et al., 2019)
Transverse compressive strength (MPa)	110	(M. Nelson & Fam, 2013).
Longitudinal shear strength (MPa)	65.5	(Ayman et al., 2017)
Transverse shear strength (MPa)	65.5	(Ayman et al., 2017)

Table 3. 3: Material properties of GFRP rebar

Mechanical properties		Sources
Elastic modulus (GPa)	46	(ACI 4401.1R-15, 2015)
Density ($Kg.m^{-3}$)	2100	(ACI 4401.1R-15, 2015)
Poisons ration (-)	0.25	(Raza et al., 2019)

Table 3. 4: Material properties of concrete

Mechanical properties			Sources
Compressive strength (MPa)	50 days	45.7±1.2	(Nicoletta et al., 2019)
	90 days	47.9	
Density ($Kg.m^{-3}$)		2400	(EN 1991-1-2, 2011)
Poisons ration (-)		0.2	(fib), 2010)

3.3 An experimental program for numerical model validation

A small-scale Glass Fiber Reinforced Polymer (GFRP) stay-in-place formwork for concrete bridge decks (Nicoletta et al., 2019) was selected and simulated to illustrate the capability and accuracy of the proposed finite element model. During the fire testing (Nicoletta et al., 2019) apply a pool fire to GFRP soffit between two point loads approximately which cover 33% of the span length of the beam. Un exposed parts of the beam were protected by using a 12.7mm thick gypsum board with a lightweight of 6.4 kg/m2. A 300mm pan diameter of pool fire with 1.6L of heptane at 0.11L/min and a flame height of approximately 0.5m was used to expose the fire to the GFRP soffit.

The beam was supported at 500mm from the base of the fuel pan (as shown in figure 3.3 b). A 14.5 min heptane pool fire was applied to the fire-damaged beam, FD, and tested at 90 days after casting due to laboratory restrictions at ambient temperatures after being exposed to fire. Four-point monotonic bending of a beam spanned 1425mm from the center of support with 125mm overhangs at either side with 475mm center to center spacing of point loads (figure 3.3a) was applied to fire-damaged specimens to identify the load-deflection performance of GFRP stay in place formwork.

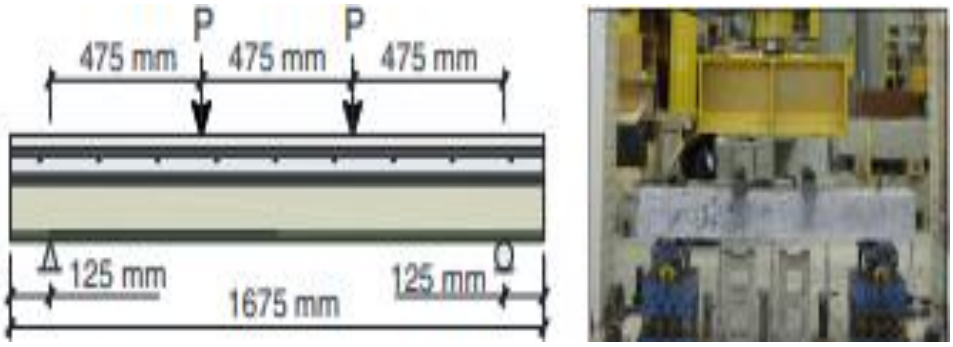

(a)

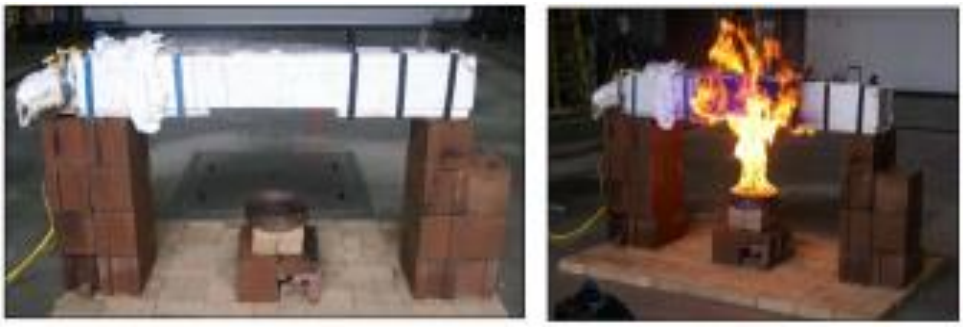

(b)

Figure 3.3: Experimental test set up of concrete deck (a) four-point loading condition and (b) exposing to pool fire[source:(Nicoletta et al., 2019)]

3.4 ABAQUS software

ABAQUS software has the capability of performing linear and nonlinear static, dynamic, and transient analyses of various engineering problems. This includes coupled temperature displacement, coupled thermal-electrical-structural, direct cyclic, dynamic, geostatic soils, static, dynamic implicit, and other complex analyses across various engineering disciplines. In this study, a nonlinear static general with a sequential thermo-mechanical analysis was performed.

ABAQUS/CAE is a complex ABAQUS environment that presents a simple, consistent interface to creating, submitting, monitoring, and visualization the results from ABAQUS/Standard and ABAQUS/Explicit simulation. Abaqus is divided into modules, each of which contains only the tools necessary for the specific portion of the modeling task. The logical sequence that the user follows to create a model corresponds to the order of the modules in the menu and the model tree(ABAQUS, 2020) are well explained as (I) Part in which individual parts are created either by sketching or importing their geometry from other interface software such as AutoCAD, ANSYS, CATIA, etc. (II) Property module which is used to create the material constitutive model, Section, composite layup and assigning of the section to the region of parts. (III) Assembly is used to an instance of parts and position of the instances relative to each other in a global coordinate system. (IV) Step module used to create and define the analysis steps, associated field, and history output results. (V) Interaction module used to define and manage mechanical and thermal interaction between the region of a model or region of the model and its surrounding, interface region and coupling schemes for an Abaqus/Standard to Abaqus/Explicit co-simulation, analysis constraints between regions of a model, assembly-level wire features, connector sections, and connector section assignments to model connectors, inertia (point mass, rotary inertia, and heat capacitance) on regions of the model, cracks on regions of the model and springs and dashpots between two points of a model or between a point of a model and ground. (VI) The load module is used to define load, boundary conditions, load cases, and predefined fields. (VII) Mesh module allows generating meshes on parts and assemblies created within ABAQUS/CAE. Furthermore, the mesh module contains functions that verify an existing mesh and assign the stacking direction of composite bodies. (VIII) The job module allows to create a job, submit it for analysis, and to monitor its progress. And finally, (IX) Visualization to read the output database that Abaqus/CAE generated during the analysis and to view the results of the analysis.

3.5 Finite element modeling

The finite element model developed for some parametric studies such as aggregate types, fire types, duration of the fire, deck width and sustained load has the same geometry as tested GFRP SIP formwork for concrete bridge decks by (Nicoletta et al., 2019) but different loading condition and material properties since the mechanical and thermal properties of materials were considered based their variation with temperature.

The geometry of the concrete, GFRP reinforcing bars, and pultruded GFRP were created as solid, wire, and shell/solid (during fire simulation) respectively.

3.5.1 Basic assumption

Some basic assumptions were proposed to simplify the simulation, analysis, and aid in convergence solution of the post-fire performance of concrete bridge deck.

- There was no bond-slip between the concrete, reinforcement, and GFRP T-up ribs, that is perfect bond is assumed.
- GFRP reinforcement is anisotropic material but it is modeled in finite elements as isotropic material.
- The heat loss due to moisture evaporation and spalling of the concrete at elevated temperatures during the fire was not considered.

3.5.2 Damage and failure criteria

In the current study, in both material concrete and GFRP were their damage and failure mechanism were taken into account. The adapted failure criteria for concrete is the compressive failure of concrete which occurs when the strain in the outermost fiber of the section exceeds 0.0038 at room temperature and according to table 2.1 as per the European code of standard (EN 1991-1-2, 2011) at elevated temperature. The material rupture of the GFRP can be controlled using material strength at room temperature and with the respective variation of material strength at elevated temperature. The initial failure of the composite material can be modeled in ABAQUS either using Tsai-Hill failure criteria (R.M. Jones, 1999) or Hashin damage criterion (Z. Hashin, 2016). The Tsai-Hill failure criteria can be used only for plane stress elements and cannot indicate the failure mode of the composites but indicate the damaged point of the composite material. It can be expressed mathematically by equation 3.1 according to the ABAQUS manual (ABAQUS, 2020).

$$\mathrm{I_F} = \frac{{\sigma_{11}}^2}{{S_1}^2} - \frac{\sigma_{11}\sigma_{22}}{{S_1}^2} + \frac{{\sigma_{22}}^2}{{S_2}^2} + \frac{{\sigma_{12}}^2}{{S_{12}}^2} \leq 1.0 \qquad (3.1)$$

Where $\mathrm{I_F}$ is Tsai-Hill failure index, σ_{11}, σ_{22} and σ_{12} are respectively the longitudinal, transversal, and shear stresses in a given point of the composite material, and S1, S2, and S12 are respectively the longitudinal, transversal, and shear strengths of the GFRP material. If Tsai-Hill index values reach $(\mathrm{I_F} = 1)$ at a given point, it shows that such point appeared to be the onset of failure. For a given stress state, this criterion allows the boundary between the damaged $(\mathrm{I_F} > 1)$ and undamaged $(\mathrm{I_F} < 1)$ state of the

composite. But, the Tsai-Hill failure criterion did not influence the reduction in material stiffness and strength of the composite material. In general, Tsai-Hill failure criteria only illustrates the zone of the composite failure and do not introduce a reduction in the mechanical properties of the material.

In opposite to the Tsai-Hill failure criterion, providing a single model to determine damage and failure initiation, Hashin damage failure criterion takes into account the material progressive damage by considering four failure criteria: fiber compression, fiber tension, matrix tension, and matrix compression. In this criterion, the equations 2.7 to 2.19 in chapter two were used. The Hashin damage failure criteria (Z. Hashin, 2016) was used in the load-dependent model to estimate the load-carrying capacity of the GFRP SIP formwork for concrete bridge deck and to predict their mode of failure. The Hashin failure criteria also need the fracture energy of the GFRP, the values were set as 12.5 N/mm in longitudinal tensile and compressive fracture energy, and 5 N/mm in transverse tensile and compressive fracture energy of fiber-reinforced epoxy (Ayman et al., 2017). In this study to avoid the convergence problem, the viscosity coefficient of fiber and matrix failure modes were assumed as 0.005 and 0.05 s respectively.

3.5.3 Thermal and mechanical contacts at the interface

There is a lack of information on contact between pultruded GFRP and concrete at elevated temperatures. Therefore, in this study, the author enforced to use of the gab conductance previously used for the contact between steel tube and concrete. The thermal resistance at the boundary between the GFRP T-up ribs and the concrete was modeled by providing the temperature-independent constant value of 200 W/m^2K gap conductance according to (Espinos et al., 2010). Furthermore, a radiative heat transfer mechanism at the interfaces between GFRP T-up ribs and concrete with an emissivity of both GFRP T-up ribs and concrete surface equal to 0.8 and configuration factor equal to 0.8. The fraction of dissipated energy caused by friction between concrete and pultruded GFRP converted to heat and the fraction of converted heat distributed to slave surface were assumed a default value of ABAQUS program (ABAQUS, 2020) set as 1 and 0.5 respectively.

The mechanical interaction between GFRP T-up ribs and the concrete contacting surface was modeled using tie constraint available in ABAQUS Standard by selecting the master and slave surface. The master and slave surfaces were selected depending on the load transferring mechanism. In this study, concrete is the master surface, and GFRP T-

up ribs are the slave surface. Moreover, the interaction between loading plates and concrete, supporting plates, and GFRP T-up ribs were modeled by surface-to-surface contact with hard contact in normal behavior which allows any force or pressure value when the two surfaces are in contact and when the surfaces are not in contact cannot transfer any force. In tangential behavior using the Coulomb friction model with a constant friction coefficient of 0.25 which had previously been used by many researchers. In surface-to-surface contact loading and supporting plates act as master surfaces, and concrete and GFRP Tup-ribs act as slave surfaces. The GFRP reinforcement is embedded into the concrete using an embedded region available in ABAQUS standard

3.5.4 Discretization of the Finite Element Model

Different element types were selected from the ABAQUS element library selection for both heat transfer and structural analysis. A three-dimensional eight-node solid linear element with temperature degree of freedom (DC3D8) was used to model concrete during heat transfer analysis. While the respective three-dimensional eight nodes (C3D8R) general-purpose linear brick element with reduced integration (1 integration point) was used to model concrete in structural analysis.

Linear displacement truss elements with two nodes (T3D2) were used in the modeling of GFRP during structural analysis. It is noted that T3D2 is a three-dimensional two-node linear displacement truss element. The three-node linear displacement quadratic truss elements are unable to model the reinforcing bar accurately since the embedded mid-node of the reinforcement is not properly in contact with the surrounding concrete and result in excessive deformation of the reinforced concrete(Hajiloo & Green, 2019). In addition, the author refers that the reinforcing bar cannot affect the temperature evolution of the reinforced concrete structure because of very small in size compared to the surrounding concrete, and it's possible to omit it during heat transfer analysis. Therefore, in this study, the effect of nodal temperature of GFRP top bar reinforcements was ignored. Figure 3.4 shows the three-dimensional elements used in structural and heat transfer analysis of the current study.

The general-purpose continuum shell element (SC8R) with an eight-node, quadrilateral, first-order interpolation, and stress or displacement continuum shell element with reduced integration was used in modeling of pultruded GFRP during structural analysis at room temperature. The continuum shell element allows for modeling of the three-dimension solid composite laminate, more accurate contact modeling, and stacking of

the composite to capture a more accurate response of composite laminate through thickness.

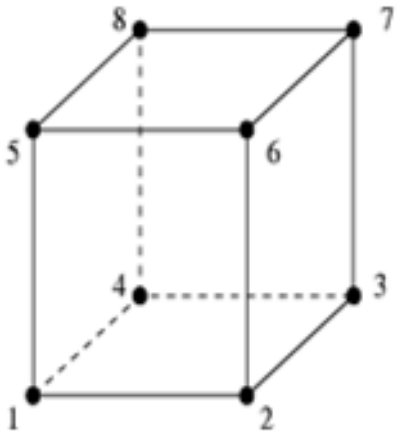

(a)DC3D8 and C3D8R element

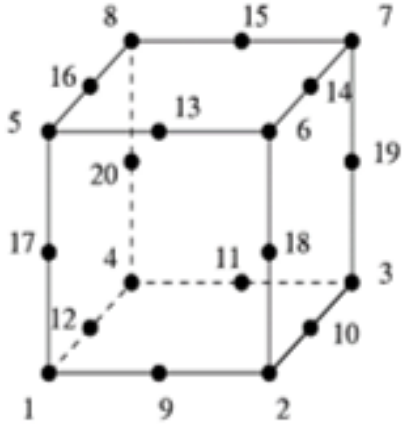

(b) DC3D20 and C3D20R element

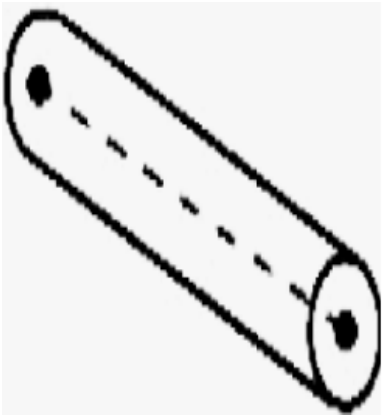

(c) T3D2 element

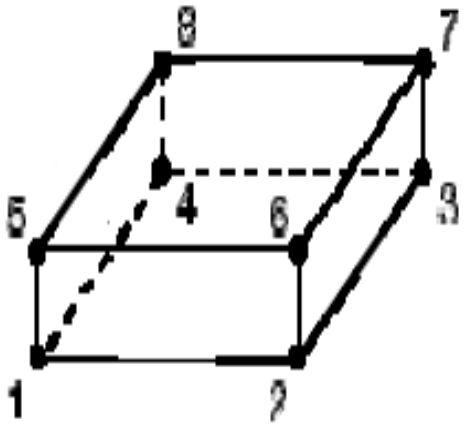

(d) SC8R shell element

Figure 3.4: The three-dimensional element model used in heat and thermomechanical analysis.

During heat transfer analysis the second-order quadratic solid element (DC3D20) was used in modeling of pultruded GFRP because in ABAQUS/Standard only for convectional shell element is available to model heat transfer in shell-type structures to input directly to the equivalent stress analysis shell element for sequentially coupled thermal stress analysis. Figure 3.5 illustrates the difference between convectional and continuum shell elements during finite element mesh.

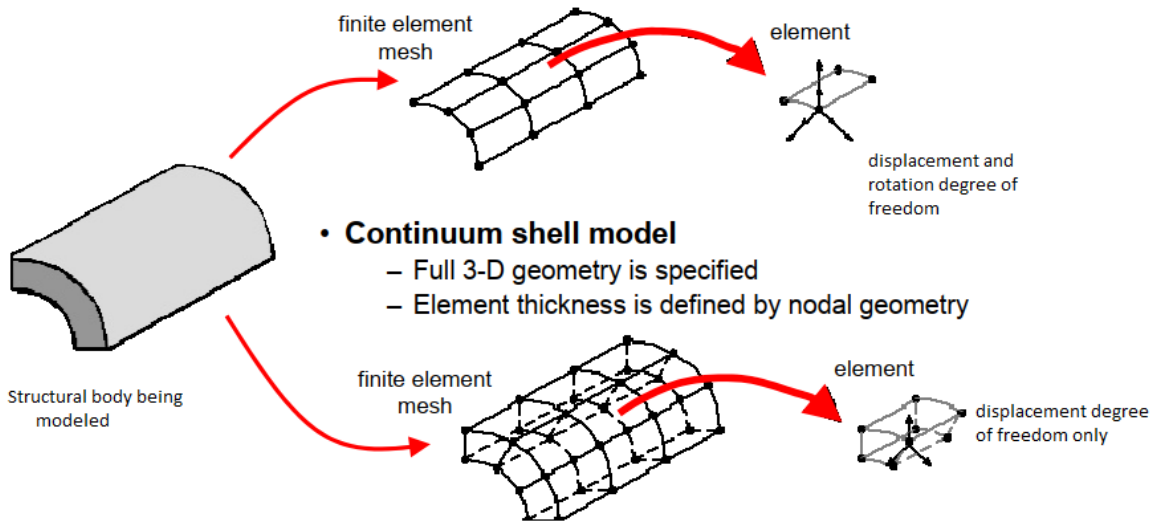

Figure 3.5: Convectional and continuum shell element

Furthermore, during thermo-mechanical analysis the corresponding (C3D20R) second-order quadratic three-dimensional solid element with twenty nodes was used to model the pultruded GFRP at elevated temperature. Its notes that the second-order element can capture high accuracy in ABAQUS/Standard than first-order element-based stress concentration and modeling geometric features. Overall, second-order elements are very essential in problems dominating bending.

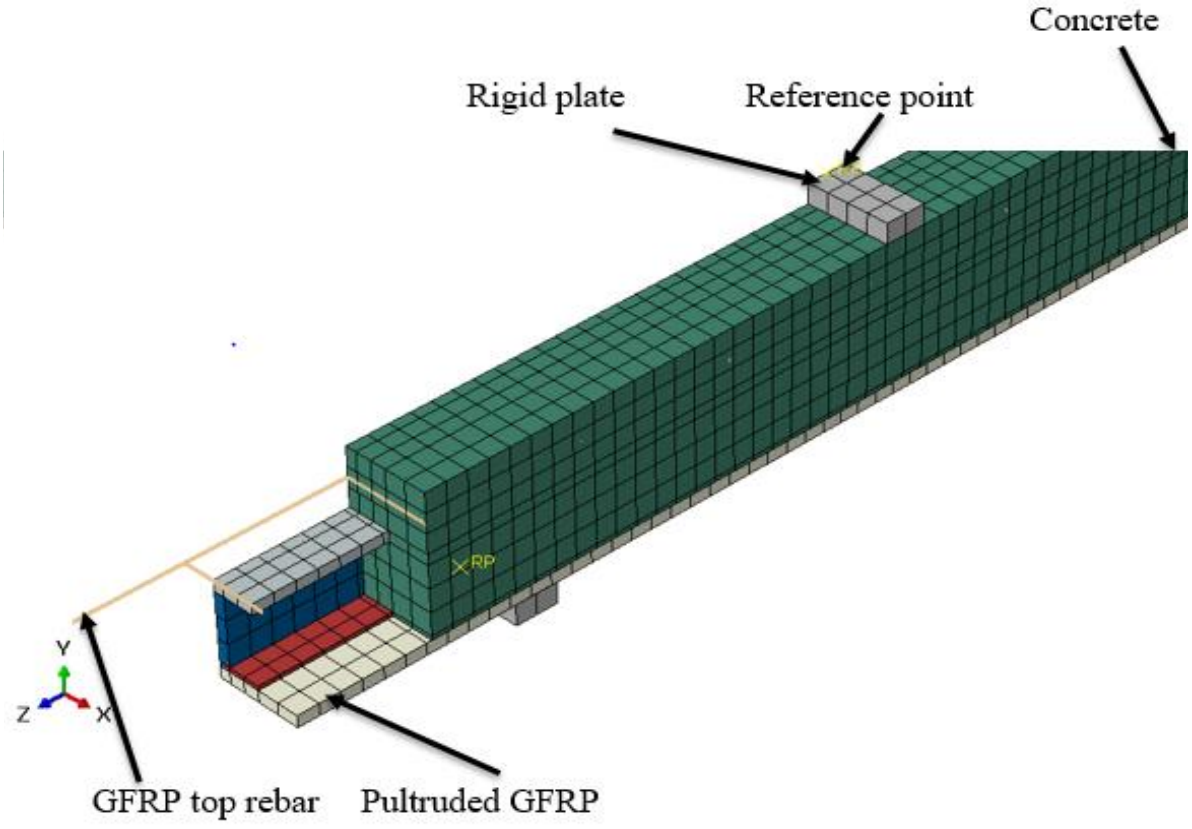

Figure 3.6: Symmetric finite element meshing of concrete bridge deck components

Table 3. 5: Element used in the current numerical model

Parts	Types of analysis	
	Structural analysis	Heat transfer analysis
	Types of element	
Concrete	C3D8R	DC3D8
GFRP rebar	T3D2	Neglected
Rigid plate	R3D4	Neglected
Pultruded GFRP	C3D20R and SC8R	DC3D20

3.5.5 Loading and boundary condition

The thermal and mechanical response of the GFRP SIP formwork for the concrete bridge deck was simulated assuming the simple supported symmetric conditions concerning the x-axis, and therefore, during mechanical analysis, the displacement in x (U1=0), rotation in y (UR2=0), and z (UR3=0) were fully restrained as illustrated in figure 3.7. The mechanical load was applied at top of the two loading of rigid plates in the Y direction (downward) to the reference point using displacement control. The value of displacement applied in all specimens was equal to the ultimate displacement (Δ_{max}) at peak load (P). The reference point of the loading rigid plates was fully constrained in all directions to prevent the excessive distortion of the elements in FRP and material instability.

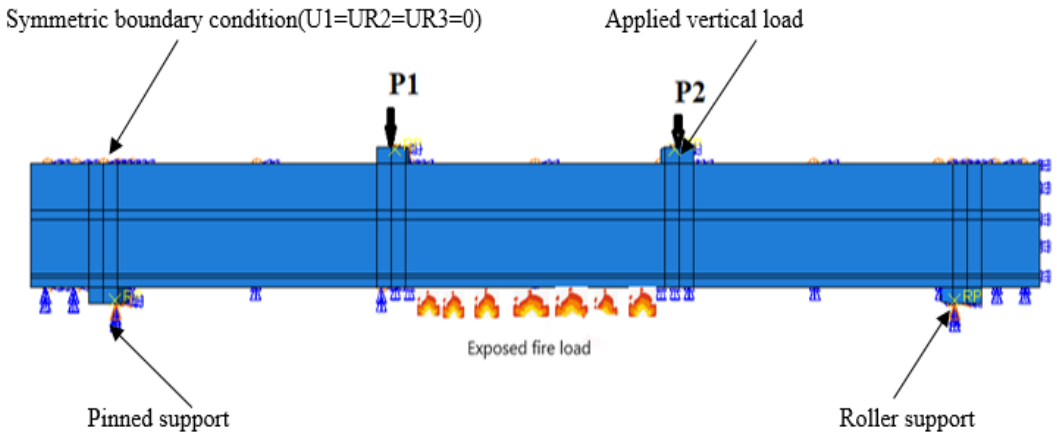

Figure 3.7: The loading and boundary condition of the concrete bridge deck

Regarding the thermal loading and boundary condition, in case of finite element validation and further parametric study except in case of durations and types of fire, the ther-

mal load was applied at the soffit of the concrete bridge deck between the two loading plates following the time-temperature curve as shown in figure 3.8 for 2340 sec. The reason why this time-temperature curve was used, it represents the real fire loading with cooling phase that the bridge deck subjected to fire. However, the standard Eurocode fire temperature curve will be applied as nodal temperature loading versus time at the soffit of the concrete bridge decks for further parametric study of fire types and duration. In the cooling stage to investigate the effect of the sustained load on concrete deck subjected to fire after cooling; linear cooling (decay) in fire temperature according to European code of standard (EN 1991-1-2, 2011) recommended according to the work of (Alconpat, 2020; Hosseini et al., 2014).

In ABAQUS software, in all fire loading cases, the average furnace temperature was applied in terms of small-time incremental steps. Each time step is composed of several smaller sub-steps that are solved using Newton-Raphson's technique. At the end of each time-temperature step, the convergence was achieved by Newton-Raphson equilibrium iterations when the temperature difference at each node from each iteration do not above 5 ^{o}C. And the boundary condition conduction, convection, and radiations were used during heat transfer analysis, and for more detail, the reader may refer to section 3.7.2 of this study. In general, the locations of the applied nodal transient temperatures are based on their damaged types and the sustained load is applied at 475mm from the center of support at each point load as shown in figure 3.3 a.

3.6 Identification of constitutive material models

The bridge deck components considered in this study consist of three materials. The three materials are GFRP reinforcement, pultruded GFRP, and concrete which are briefly described in chapter two based on information presented in the current code of standard, manuals, and previously conducted research. In this section, it is necessary to describe how material properties and stress-strain curves of the two main components are accurately implemented into the finite element modeling both at room and elevated temperatures. Numerical analysis of the post-fire performance of GFRP SIP formwork for concrete bridge decks requires the material properties of concrete and GFRP at elevated temperatures. These material properties are categorized into two parts: (i) thermal properties and (ii) mechanical properties. The thermal properties include mass or density, specific heat capacity, and thermal conductivity.

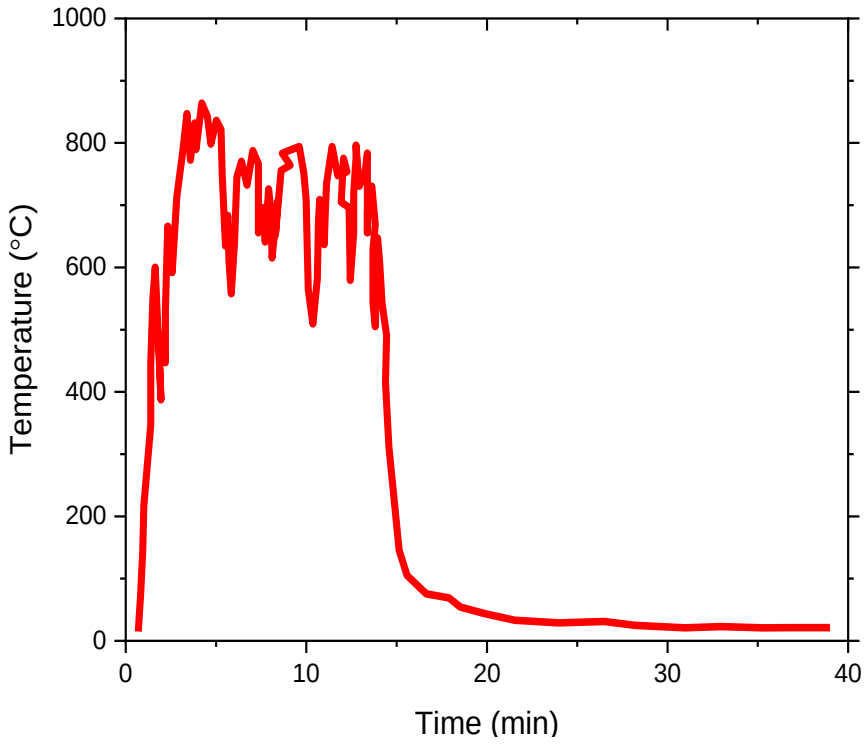

Figure 3.8: Pool fire loading of time-temperature history [sources: (Nicoletta et al., 2019)]

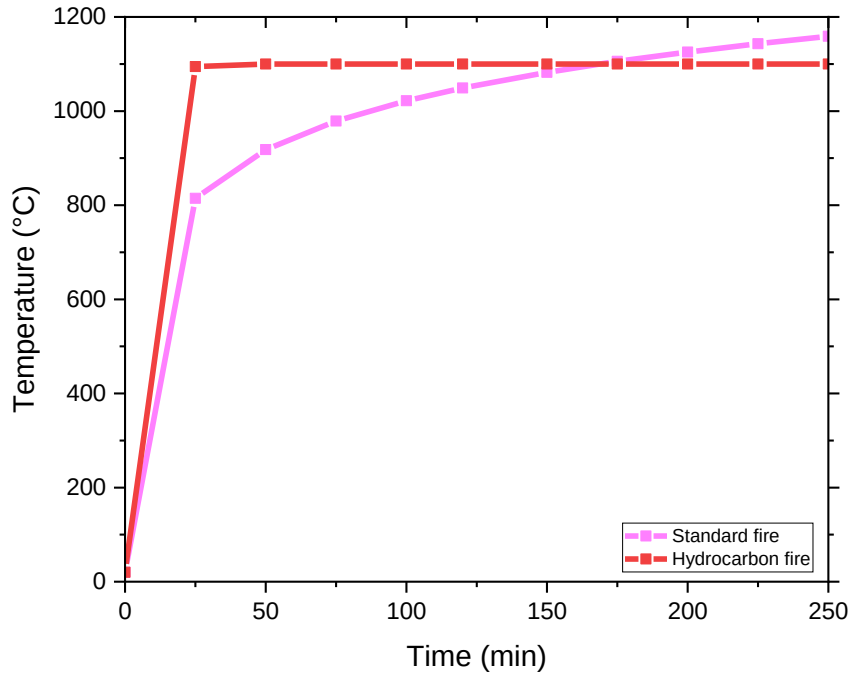

Figure 3.9: Nominal temperature-time curve for standard and hydrocarbon fires [source: (EN 1991-1-2, 2011)]

The thermal properties of the materials manage the transfer of heat and temperature distribution across the section while the mechanical properties of the material include elas-

tic modulus, poisons ration, tensile strength, shear strength, compressive strength, stress-strain, thermal strain, or thermal expansion which determines the stiffness, strength, and deformation of the material after exposure to elevated temperature.

3.6.1 Concrete

ABAQUS program (ABAQUS, 2020) can allow three ways to simulate the damage in concrete using the crack models, those are concrete damage plasticity (CDP) model, brittle crack model, and smeared crack concrete model. In this study, Concrete Damage Plasticity (CDP) model was used to model the mechanical behavior of concrete at room and elevated temperatures by providing inelastic behavior of the concrete in compression and tension softening of the concrete with their respective damage parameters. The failure criteria mechanisms in CDP are cracking and crushing of the concrete under tensile and compressive strength. The basic initial requirement to define the CDP model in ABAQUS such as yield surface, a hardening rule, and a flow rule is essentially taken into consideration. The four constitutive parameters used to model the yield surface of concrete are: (a) the poisons ratio set as 0.2 which controls the volume changes of concrete before the inelastic behavior. (b) The dilation angle ($\boldsymbol{\psi}$) which is the internal friction angle of concrete was taken as 35^{o} default value of ABAQUS was recommended as calibrated in section 3.8. (c) The flow potential and (d) the ratio of the second stress invariant on the tensile meridian to that on the compressive meridian; in this study, the default values in the ABAQUS program respectively 0.1 and 0.66 were used. The default value for the ratio of initial biaxial compressive yield stress to initial uniaxial compressive yield stress was 1.16. Through finite element calibration, the viscosity of the concrete was determined to be 0.004 (see section 3.8). All above-listed parameters were implemented into the finite element model independent of the temperature since according to the author's knowledge there is no information presented in a code of standard and published papers on their mechanical properties with temperature variation.

In the present study, the default value of stiffness recovery factors of concrete both in compression and tension at room and elevated temperature. In past also, numerous researchers use the default value to model the stiffness recovery of concrete in finite element software ABAQUS (Poudel and Yadav, 2021; Wahalathantri et al., 2021). Therefore, the default value in ABAQUS for the compressive stiffness recovery factor, W_c = 1is used based on an assumption that compressive stiffness of concrete is fully recov-

ered upon the closure of crack as the load changes from tension to compression, and the tensile stiffness recovery factor, $W_t = 0$ is assumed that the tensile stiffness is not recovered as load changes from compression to tension once the initiation of concrete crushing. The reinforcement and surrounding concrete act independently during the cracking of the concrete.

3.6.1.1 Thermal properties of concrete

Thermal conductivity, specific heat capacity, and density of concrete are the required material parameter to perform transient heat transfer analysis. The equation of Eurocode (EN 1991-1-2, 2011) is used in this study to define the temperature-dependent thermal properties of concrete at elevated temperatures for both siliceous and carbonate aggregates. For more information, the reader may refer the chapter three of this study. Figure 3.10a illustrates the variation of specific heat capacity with temperature. It can be seen between the temperature of 100 and 115 °C there is a sharp spike is presented with the ultimate value of specific heat capacity which has a variation with the moisture content of the concrete. In figure 3.10a the specific heat capacity of the concrete was shown for the moisture content of the concrete up to 10% but in this study, the effect of moisture content not concrete that is 0% moisture contents were assumed.

Eurocode (EN 1991-1-2, 2011) proposed the upper and lower limit of the thermal conductivity of the concrete at elevated temperatures. In this study, the heat transfer analysis was performed using the upper limit of thermal conductivity of the concrete and good agreements were made with the experimental result as shown in chapter four, figure 4.1. Most researchers recommend the upper limit of the thermal conductivity of concrete (Hawileh & Rasheed, 2017). For the further parametric study on the effect of types of aggregates (ASCE, 1992) equations were used (figure 3.10b). The density of normal weight concrete for siliceous and carbonates was taken as 2400 $kg.m^{-3}$.In ABAQUS software density has been defined as a function of temperature and/or field variables. For all elements except acoustic, heat transfer, coupled temperature-displacement, and coupled thermal-electrical elements the density is a function of the initial values of temperature and field variables. It will not be updated if temperatures and field variables change during the analysis. Therefore in this study, density can be with only the initial temperature of 20 °C.

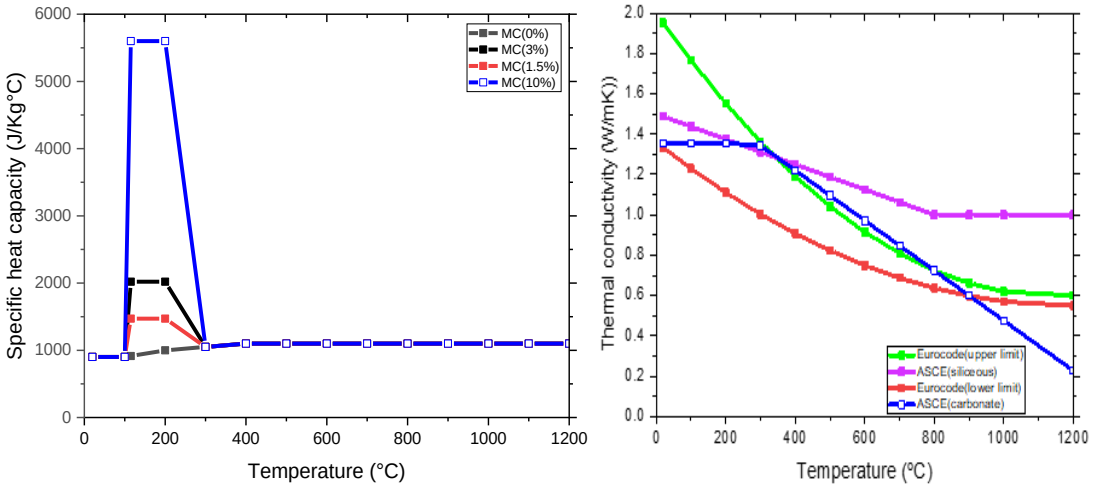

(a) (b)

Figure 3.10: The variation with the temperature of (a) specific heat and (b) thermal conductivity of concrete [source: (EN 1991-1-2, 2011)

3.6.1.2 Mechanical properties of concrete

The Compressive strength, tensile strength, elastic modulus, poisons ratio, and stress-strain response in compression are the mechanical properties of concrete used in fire resistance design. In this study, the equation of Eurocode (EN 1991-1-2, 2011) on compressive, tensile, and stress-strain of concrete at elevated temperature were used. Figure 3.12a illustrates the variation of compressive strength for NSC for siliceous and carbonate aggregates according to Eurocode (EN 1991-1-2, 2011) at elevated temperature and figure 3.11a the stress-strain curve used at room temperature in this study. Between 20°C to 100°C the degradation in compressive strength for both types of aggregates is the same while at 100°C to 1000°C shows a larger variation in the reduction of compressive strength. The tensile strength of concrete is lower than compressive strength and ignored in strength calculations at elevated temperatures. However, it is an important property in terms of fire resistance, because cracking in concrete is typically caused by tensile stresses, and structural damage of the member in tension is frequently caused by progression in micro-cracking (Sidney Mindess and J. Francis Young, 2003). In case of; to account the tensile strength of the concrete Eurocode (EN 1991-1-2, 2011) allows the reduction factor coefficient,$K_{c,t}(T)$ as illustrated in figure 2.11 and tensile stress-strain of concrete at room and elevated temperature presented in figure 3.9b and 3.88b respectively. The elastic modulus of the concrete affected by various variables such as mixing, water-cement ration, quantity and nature of aggregates, age of

concrete, and nature of conditioning(V. Kodur, 2014a). At elevated temperatures, the elastic modulus of concrete rapidly decreases as the temperature rises (figure 2.12).

Most of the existing constitutive models focus on the relationship between stress-strain curves with compressive strength of concrete, strain at peak stress, and ultimate strain of concrete at elevated temperature (Krishna et al., 2019a). In this study, the compressive stress-strain curves at elevated temperature are implemented into the finite element model as per the relationship developed by Eurocode (EN 1991-1-2, 2011). The stress up to $0.3f'c$ is linear for the stress-strain curves at different elevated temperatures with a nonlinear ascending branch up to $f'c$. For descending branch the Eurocode permits linear or nonlinear stress-strain curves at various elevated temperatures. To ensure the numerical convergence ABAQUS(ABAQUS, 2020) enforces a lower value of compressive and tensile strength of the concrete not less than 0.01 of the initial compressive and tensile strength of the concrete implemented into the ABAQUS program. Figure 3.12a illustrates the reduction of the compressive stress-strain curve of siliceous aggregates introduced into the FEM in the current study up to 1100 °C for the concrete compressive strength of 45.7 MPa. The linear thermal expansion coefficient,α of the concrete with the variation of temperature required to input into the ABAQUS program was according to the equation of (ASCE, 1992).

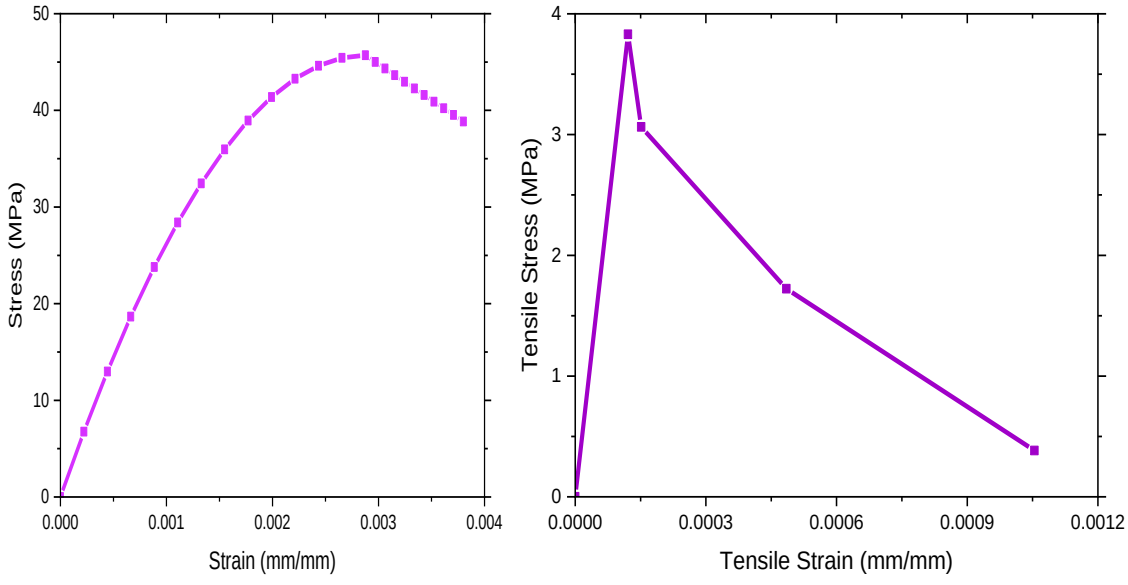

(a) (b)

Figure 3.11 :(a) Compressive and (b) tensile stress-strain of concrete at room temperature

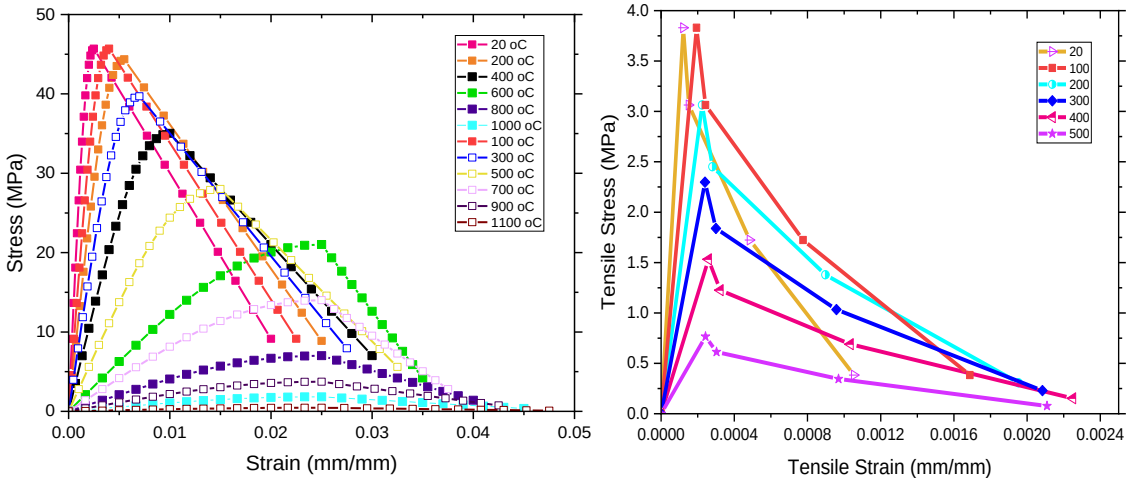

(a) (b)

Figure 3.12 :(a) Compressive and (b) Tensile stress-strain of concrete at elevated temperature

3.6.2 Glass Fiber Reinforced polymer

The GFRP is an anisotropic material, due to limited studies on thermal and mechanical properties, it is assumed as an isotropic linear elastic behavior providing the elastic modulus and strength of material properties for GFRP rebar in finite element software ABAQUS and ANSYS (Hawileh & Rasheed, 2017; Raza et al., 2019) until failure without fiber damage criterion. Therefore, in this study, the GFRP reinforcement rebar was simulated in the ABAQUS program as elastic-brittle materials until rupture. Figure 3.13 illustrates the stress-strain relationships of GFRP reinforcement that are applied in the FE simulations.

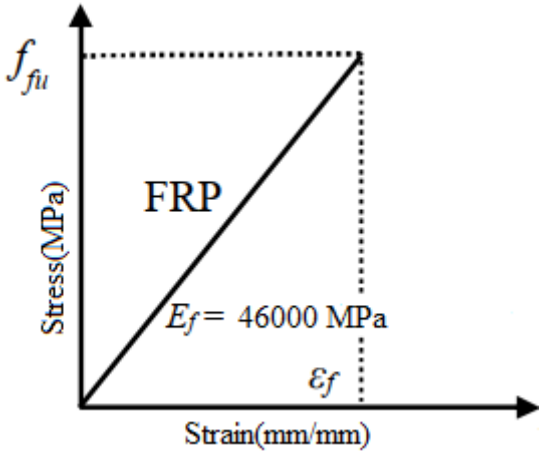

Figure 3.13: The stress-strain relationships of FRP reinforcement

The pultruded GFRP SIP formwork for concrete decks was modeled as anisotropic material according to the material properties of the manufacturer (M. Nelson & Fam, 2013) and presented data according to (Nicoletta et al., 2019) using engineering con-

stant parameters such as elastic modulus in the x-direction (E1), elastic modulus in the y-direction (E2), elastic modulus in the z-direction (E3), poisons ration in XY (NU12), poisons ration in XZ (NU13), poisons ration in YZ (NU23), shear modulus in XY (G12), shear modulus in XZ (G13), shear modulus in YZ (G23) available in ABAQUS/standard based on the manufacturer data listed in table 3.3 to 3.4. In ABAQUS; the composite material can be modeled using the composite layup in which the number of plies, material, rotation angle, and integration points is specified. Based on the partition cell of the pultruded GFRP different thickness of the composite layup was performed in ABAQUS program with [0/40/90/130º] fiber orientation according to (M. Nelson & Fam, 2013) conduct an experimental investigation GFRP panel similar with GFRP SIP formwork for concrete bridge used in this study. The panel consists of the 12.7mm GFRP base plate integrated with T-up ribs spaced at 12.7 mm, and the ribs are 12.7 mm thick with a flange width of 102 mm.

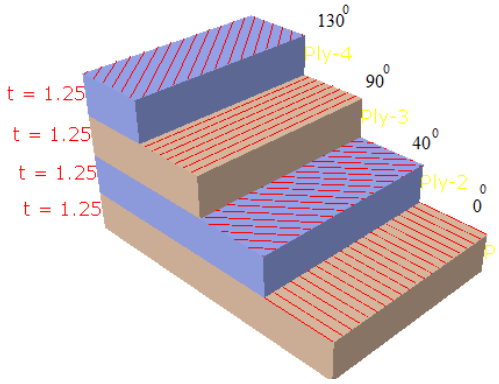

Note: All dimensions are in millimeter (mm) and degree (º)

Figure 3.14: Composite layup of Pultruded GRP

3.6.2.1 Thermal properties of Glass Fiber Reinforced Polymers

For fiber-reinforced polymer rebar's, their thermal properties(thermal conductivity, specific heat capacity, and density are not accounted in the finite element model in heat transfer analysis since they do not affect temperature evolution within the cross-section and negligible volume ratio in reinforced concrete section (Yu & Kodur, 2013). However, the properties of constitutive materials of pultruded GFRP varying with temperature have a significant effect on the thermal response of concrete bridge deck exposed to fire. For pultruded GFRP high-temperature thermal properties were built into the finite element model according to (T. Keller et al., 2006a) as illustrated in figure 3.15a and b. The density of pultruded GFRP at room temperature was taken as 2100 $Kg.m^{-3}$ with independent of temperature from ACI code of standard (ACI 4401.1R-15, 2015).

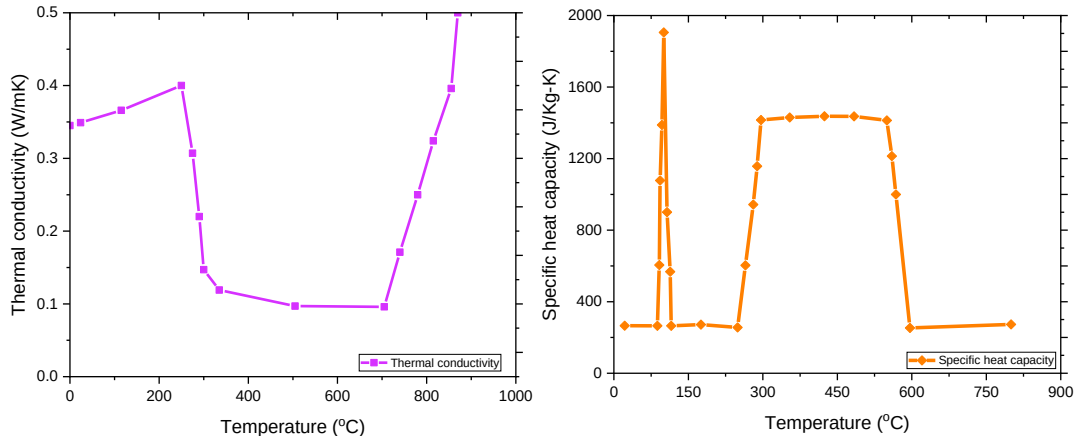

Figure 3.15: The variation with the temperature of (a) thermal conductivity and (b) specific heat capacity of pultruded GFRP Mechanical properties of GFRP

In terms of mechanical properties of FRP bars at elevated temperatures, lack of sufficient and well-documented databases, and there is an agreement between the researchers as well as the design codes that the behavior of FRP reinforcing bars require further investigation. Therefore, in this study, the variation of the mechanical properties of the GFRP reinforcing bars and the pultruded GFRP were taken from the published paper. Figure 3.16a presents the reduction factor in shear, tensile and compressive strength of the pultruded GFRP up to 250 °C according to the experimental work of (B. and Keller, 2009) and in figure 3.16b the reduction factor in elastic modulus of FRP and steel according to (Saafi, 2002) were compared and illustrated. The elastic modulus of the FRP rebar remains constant up to the temperature of 100 °C and decreased linearly as the temperature increases.

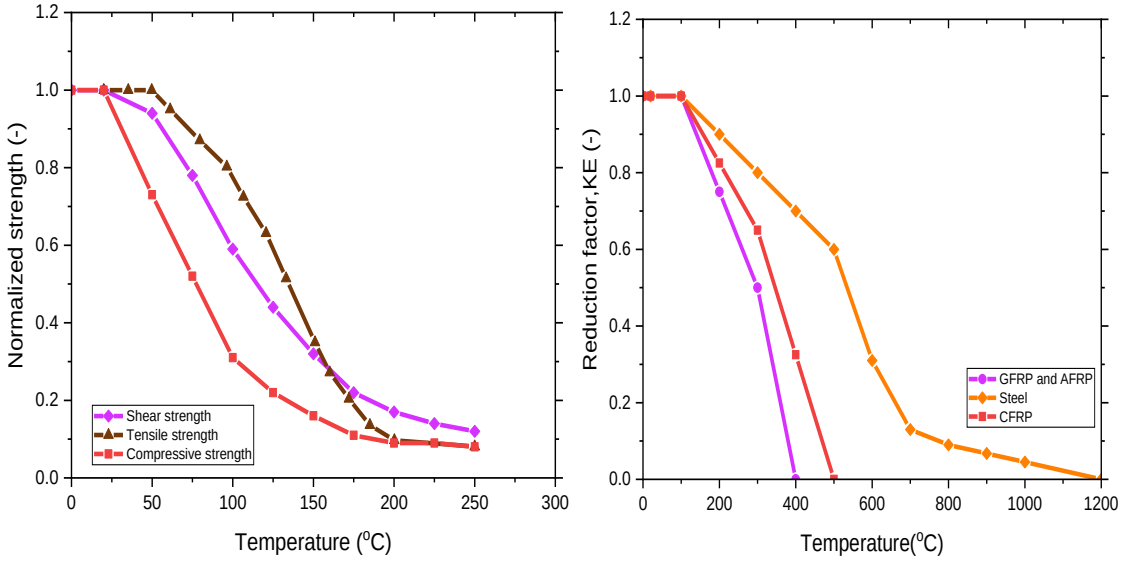

(a) (b)

Figure 3.16. The Variation with the temperature of mechanical properties of FRP

The linear thermal expansion coefficient (CTE) of FRP reinforcing bars are widely different in the longitudinal and transverse directions. The longitudinal thermal expansion of FRP is dominated by the fibers while the transverse direction is dominated by resin properties (ACI 4401.1R-15, 2015). According to this guide, the coefficient of thermal expansion of GFRP varies from 6 to $10*10^{-6}/\,^{o}C$ in the longitudinal direction and 21 to $23*10^{-6}/\,^{o}C$ in the transverse direction. At elevated temperatures, there is limited information on the variation of thermal expansion of GFRP rebar with temperature. Consequently, in this study, only the longitudinal CTE GFRP reinforcing rebar is taken as $6 \times 10^{-6}/°C$ based upon the material properties provided by (ACI 4401.1R-15, 2015) independent of temperature. Experiment investigation shows that based on the rule of mixture the coefficient of thermal expansion of pultruded GFRP along the direction of the pultrusion $\alpha_x = 12.6\times10^{-6}/K$, transverse $\alpha_y = 21.8\times10^{-6}/K$, and through-thickness $\alpha_z = 37.0\times10^{-6}/K$ (T. Keller et al., 2006a) and the values were used in this study independent of temperature

3.7 Finite element analysis

The finite element software (ABAQUS, 2020) was used to implement the proposed finite element models. The temperature-independent thermal and mechanical contact models described above were provided in the ABAQUS program (ABAQUS, 2020) to accurately simulate the interface between concrete and pultruded GFRP. The constitutive material models for concrete, GFRP rebar, and pultruded GFRP were implemented into the framework of the software packages. The modeling of fire performance of concrete bridge decks subjected to fire was conducted using sequentially coupled thermomechanical analysis. The sequentially coupled thermomechanical analysis means that the stress analysis depends on thermal analysis; however, the reverse is not permitted in ABAQUS software(ABAQUS, 2020). Therefore, this procedure consists of two stages: first, heat transfer analysis in which the temperature distribution of the cross-section of the structures is obtained. Second, stress analysis is sometimes a so-called mechanical analysis in which the residual strength of the structures is evaluated. More detailed descriptions of both types of analysis were given in sections 3.7.2.1 and 3.7.2.2.

3.7.1 Procedure of analysis

The process of developing finite element modeling and analysis was classified into the following five stages.

- Concrete, GFRP Tup ribs, GFRP base plate, loading plate, support plate, and GFRP rebar were created as separate parts in the graphical interface of the *ABAQUS (2020)* program. Since the sequential analysis was performed two models are constructed as per the case study; one model for heat transfer analysis and the other for structural analysis. During the finite element modeling of concrete bridge decks, the configuration of the model is similar for both heat transfer analysis and mechanical analysis. The number of elements and mesh size remain the same for both thermal analysis and mechanical analysis to transfer safely the nodal temperature from heat transfer analysis to stress analysis.
- Thermal and mechanical properties for concrete, GFRP Tups ribs, and GFRP rebar were defined. In this section, the heat transfer model is differentiated from the structural analysis using element types, boundary conditions, and loading.
- Thermal analysis was performed by using the time-temperature history obtained from experimental results by(Nicoletta et al., 2019) for finite element model validation only. However, for further parametric study, the standard fire curve(ISO 834) and hydrocarbon fire asper (EN 1991-1-2, 2011) were used.
- Sustained loads were applied as a displacement control at the top face of concrete bridge decks in the structural analysis model to study stress-strain before exposure to fire.
- The pre-defined field available in the *ABAQUS* program was defined at the end-stage of analysis to transfer the nodal temperature into the mechanical analysis model, and sustained load and thermal effect were analyzed simultaneously at each increment of the analysis time.

3.7.2 Type of analysis and increments

The sequential thermo-mechanical analysis procedure in ABAQUS/Standard was used in the current study to analyze the GFRP SIP formwork concrete bridge deck subjected to fire.

3.7.2.1 Heat transfer analysis

In this study to simulate the thermal response of the GFRP SIP formwork concrete bridge deck; a transient heat transfer process is considered, during which the heat from the fire flow to the soffit of the concrete deck and then propagated into the inner part of the deck. The boundary conditions convective and radiative are used to transfer the heat from the fire to the surface of the deck (Dai et al., 2014; Hajiloo & Green, 2019) and

conduction is used to transfer the heat from GFRP SIP formwork to the concrete section. The heat convection and radiation are analytically expressed by equation 3.2

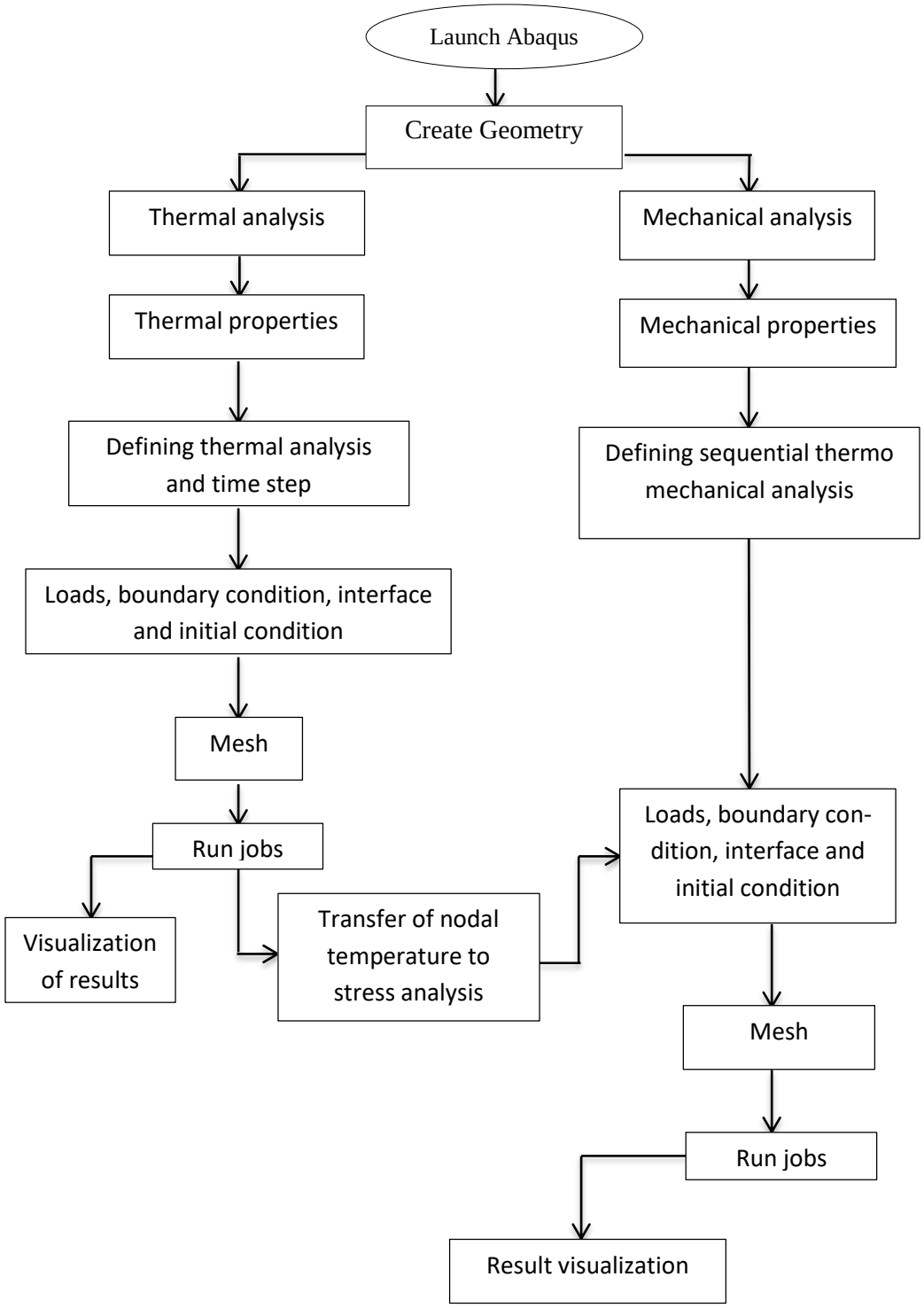

Figure 3.17: Flow chart of finite element modeling and analysis procedure

$$k\frac{\partial T}{\partial n} = h_c(T_g - T_m) + \varepsilon_m * \varepsilon_f * \sigma\left((T_g - T_z)^4 - (T_m - T_z)^4\right) \quad (3.2)$$

Where n is the outward normal direction of the deck surface; h_c is the coefficient of convective heat transfer, T_g is the gas temperature near the fire exposed surfaces, T_m is the surface temperature of the structural member $\varepsilon_m, and\ \varepsilon_f$ is the surface emissivity of the element and the fire respectively. The Stefan Boltzmann constant σ is taken as $5.67*10^{-8}$W/m^{2}K^4 and T_z is the absolute zero and the initial temperature was set at -273.15 °C below zero and 20 °C respectively. During fire simulation in ABAQUS, the effect of convection is based on film condition with the varying temperature-time curve according time-temperature curve illustrated in Figures 3.8 and 3.9. For standard fire; the film condition was defined as 25 W/m^{2}K as h_c for the fire exposed portion of the concrete bridge deck. The unexposed part of the concrete bridge deck the film condition was taken as 9 W/m^{2}K. While for hydrocarbon fire; the film condition of 50 and 9 W/m^{2}K for exposed and unexposed parts of concrete bridge deck based on the provision of Eurocode(EN 1991-1-2, 2011). The nodal temperature obtained during heat transfer analysis was read into mechanical analysis for stress analysis as a predefined field in the respective step module created in ABAQUS/Standard. The temperature read into the stress analysis were varied in position and time. The ABAQUS/Standard can interpolate the nodal temperature of the points within the element based on the convergence required.

3.7.2.2 Mechanical response analysis

In the current study, the mechanical analysis is divided into two stages: first, the concrete bridge deck is loaded at room temperature to investigate the material stability and behavior of the concrete bridge deck; and second, the surface temperature which applies the nodal temperature to each node on the surface from heat transfer analysis is then applied as predefined to model the process of fire. Following the fire load, the mechanical load was applied to the concrete bridge deck using displacement control at the reference point of the rigid plate as illustrated in figure 3.7. During the mechanical analysis to transfer the nodal temperature from heat transfer analysis to stress analysis, the finite element mesh was kept uniform. However, the thermal elements were changed to their respective stress element as further explained in section 3.5.4. Throughout, a sequentially coupled thermomechanical analysis the real fire period (2340 sec) was replaced to the extremely small period of 1s since the computational time of the real fire period during mechanical analysis needs huge time even a week; as a result, it is necessary to use the load factoring(Mago et al., 2014). The ABAQUS pro-

gram selects the value of each step time automatically depending on the required convergence; the minimum step time chosen in this study was initial (0.001), minimum (0.00001), and maximum (0.001) to avoid the numerical convergence problems relating to the nonlinear analysis. Because the concrete bridge deck exposed to fire generally undergoes significant deflections, the consequences of dimensional nonlinearity were incorporated into the Finite element model by using the updated Lagrangian approach(ABAQUS, 2020). The influence of nonlinear geometry has been included in the ABAQUS program by turning on the Nlgeon, choosing automatic stabilization with a default value of specified dissipated energy fraction 0.002, and adaptive stabilization with the maximum ratio of stabilization to strain energy 0.05.

3.8 Calibration of mesh sensitivity and plasticity parameters

The finite element analysis requires the calibration analysis to find the effect of the varying constitutive material parameters on the finite element model comparing the result of numerical and experimental tests. Additional to ensure the accuracy and convergence of the finite element model of the concrete bridge deck, it is necessary to investigate the role of varying geometric and concrete material input plasticity parameters to obtain accurate results. These parameters are mesh sensitivity study, dilation angle, viscosity parameter, eccentricity, stress ratio, and shape factor. However, according to (Raza et al., 2019) conduct, in an investigation on plasticity parameters only viscosity parameters, dilation angle, and mesh size have an impact on the finite element analysis result. The result indicates that with increasing viscosity parameter from 0.0018 to 0.0068 the peak load of the control specimen increased by 16%. Moreover, the ultimate load increased by 13% when the mesh size of the element decreased from 60mm to 15mm. The effect of dilation angle has only 4.75% on the peak load of the control specimen when it is increased from 30^{o} to 40^{o}. Therefore, viscosity parameters and mesh size have a critical influence on finite element results.

Specimen C1 was selected to calibrate the effect of those parameters on the load defection response of the concrete bridge in comparison with the experimental test. After that, the calibrated parameters are used to simulate the nonlinear finite element analysis of concrete bridge deck subjected room and elevated temperature. The following subsection describes the effect of varying mesh size and concrete damage plasticity model on load-deflection response.

3.8.1 Mesh sensitivity analysis

Mesh sensitivity analysis was performed to avoid the effect of element size on the analysis of the results(Elbahy et al., 2021). It can also investigate to obtain the optimal mesh size and as the finite element size becomes finer; the computational cost of the analysis increase. Due to this, it is necessary to model either half or quarter of the structures based on the mesh size required. Mesh sensitivity analysis was carried out to overcome the effect of element size on finite element analysis results. In this study, the mesh size of 20mm, 25mm, and 30mm was used to investigate the effect of mesh size on load-deflection response of concrete bridge deck. In figure 3.18 it is observed that as the mesh size element increase the accuracy of finite element result decreases. Therefore, the optimum mesh size of 25 mm was selected for this study.

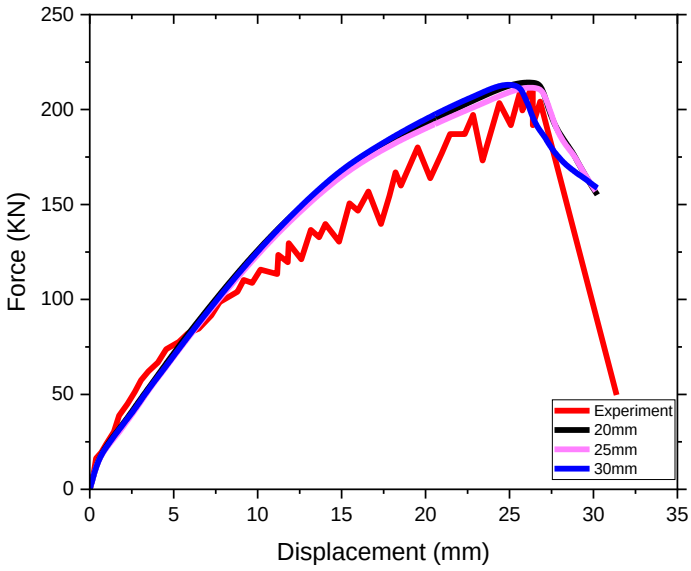

Figure 3.18: Effect of mesh size on load-deflection response of concrete bridge deck

3.8.2 Viscosity parameter

Viscosity parameter is used for visco-plastic regularization of the concrete constitutive equation in Abaqus/Standard analysis. The viscosity parameter can also serve for improving the problem of convergence in nonlinear finite element analysis. The smaller value of viscosity requires less regularization and gives an accurate result, but the small value of viscosity significantly increases the computational cost of the analysis and is faced with the problem of convergence(Wahid & Bisby, 2019).

This parameter is neglected in Abaqus Explicit due to ABAQUS/Explicit did not have convergence issues. The default value viscosity in Abaqus is zero. In this study, the approximately high value of viscosity parameters ranging from 0.0035 to 0.005 was taken

due to the convergence problem of finite element analysis. Figure 3.19 illustrates the effect of varying the viscosity parameter on load-deflection response. It can be seen that keeping the time increment of the initial and maximum increment constant through the analysis to 0.001 and mesh size of 25mm, a higher value of 0.005 viscosity can estimate a stiffer response of concrete bridge deck than experimental test and smaller value of 0.0035 can predict less value of the ultimate load. Therefore in this study, the most approximate value was achieved using 0.004 viscosity of concrete keeping the mesh size and dilation angle 25 mm and 35^{o} respectively.

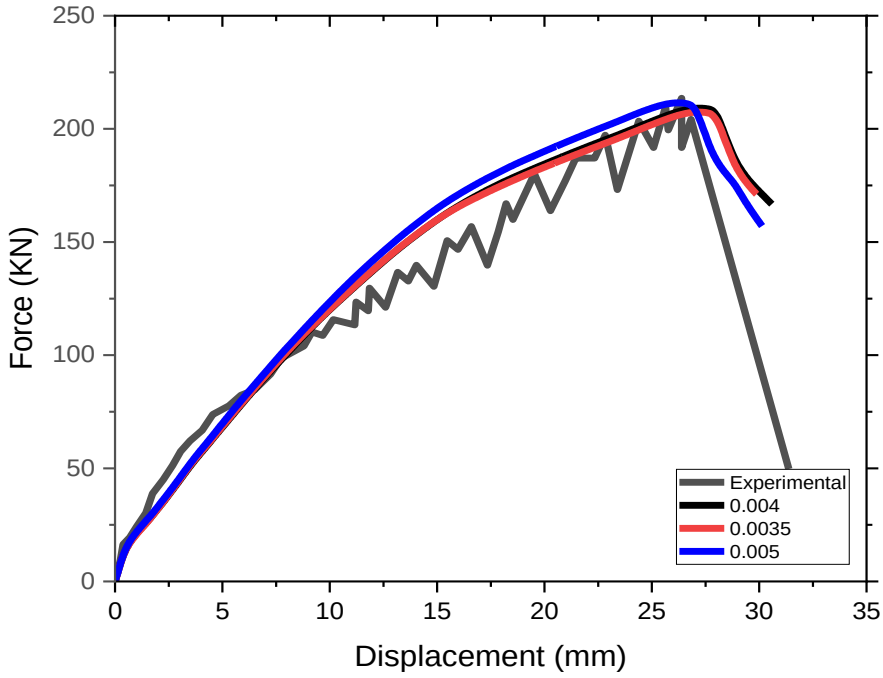

Figure 3.19: Effect of viscosity on the load-deflection response of concrete bridge deck

3.8.3 Dilation angle

Dilation angle defines the concrete dilatancy or a volume change in concrete which is influenced by inelastic strain in Ducker-Prager hyperbolic function, used in concrete plasticity flow potential in concrete damage plasticity model(Dassault system, 2012). Also according to (Raza et al., 2019) dilation angle is one of the constitutive material parameters and act as the internal friction angle of the concrete. The Drucker-Prager function can be expressed in terms of dilatancy parameter for the concrete and represented by equation 3.3

$$G = \sqrt{2J_2} + \alpha_p I_1 \tag{3.3}$$

Where α_p the dilatancy parameter for concrete.

The flow potential function used in the concrete damage plasticity model can be derived from equation 3.3 of Drucker-Prager hyperbolic function is represented by equation 3.4:

$$G = \sqrt{(\varepsilon\sigma_{to}tan\psi)^2 + q^2} - ptan\psi \quad (3.4)$$

Where $\boldsymbol{\psi}$ is dilation angle, $\boldsymbol{\varepsilon}$ is the eccentricity parameter of the plastic flow potential function required to adjust the shape of hyperbola and σ_{to} is the tensile strength of the concrete.

In this study to observe the effect of dilation angle parameter on the load-deflection response of concrete bridge deck the dilation angle 35°, 37°, and 40°. Figure 3.20 shows the effect of the dilation angle on the load-deflection curve for specimen C1. It can be noted from the load-deflection response the effect of the variation of dilation angle on finite element analysis results is relatively small as compared with the effect of the viscosity parameter. Therefore, in this study, the default value of viscosity parameter 35° is used throughout the finite element model of concrete bridge deck material both at room and elevated temperatures.

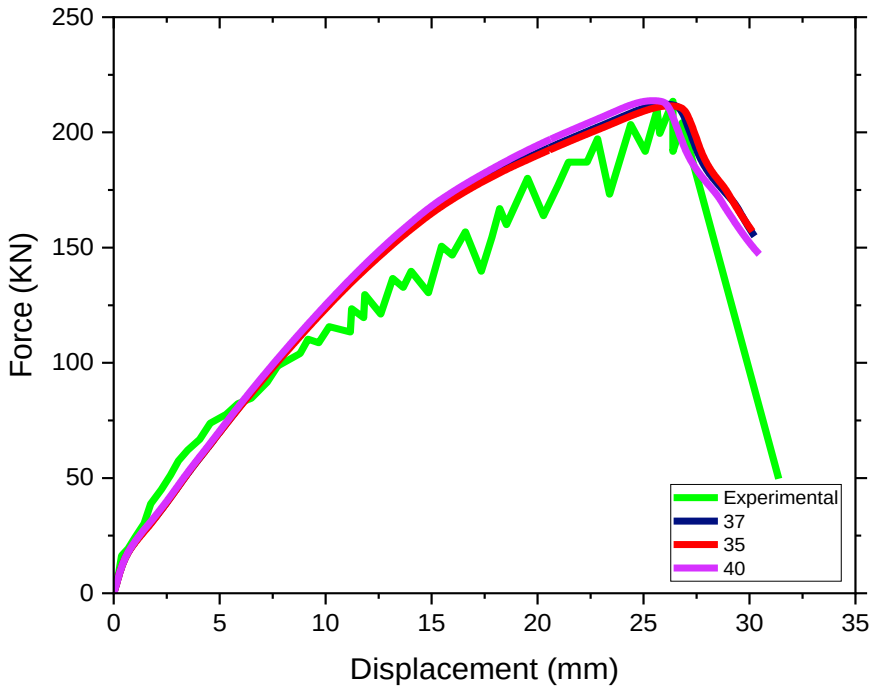

Figure 3.20: Effect of dilation angle on the load-deflection response of concrete bridge decks

The plasticity parameter viscosity, eccentricity, dilation angle, stress ratio, and shape factor used in the current study were presented in table 3.6.

Table 3. 6: Concrete plasticity parameter used in current study

parameter	values	Remark
Viscosity(-)	0.004	Calibration
Eccentricity(-)	0.1	Default
Dilation angle(degree)	35	Calibration
Stress ration	1.16	default
Shape factor	0.67	default

CHAPTER FOUR
RESULTS AND DISCUSSIONS

4.1 General

In this section, the main finding of this study is described based on finite element analysis. The validation of finite element models is performed using a commercially available finite element software ABAQUS/Standard. In this study, the experimental program of (Nicoletta et al., 2019) is used as a benchmark to validate the accuracy of the developed finite element model. The results of this small-scale experimental investigation on the post-fire performance of GFRP stay in place formwork concrete bridge decks validates with the ABAQUS finite element analysis and compared with load versus deflection, crack patterns, failure modes, and time-temperature history. The developed and verified numerical model is used for further parametric study on types of fire, duration of the fire, Sustained service loading (in addition to bridge deck self-weight), length of GFRP plate, the thickness of GFRP plate, types of aggregates, span to depth ration, and deck width

In the next section of this chapter, a separate validation of the numerical model against thermal test and structural response of concrete bridge deck at room and elevated temperature after exposure to fire are further illustrated. In this chapter also various parameters that affect the performance of the GFRP SIP formwork concrete bridge deck under fire were further investigated by the finite element model. Overall, the structural and thermal response of the GFRP SIP formwork concrete bridge deck is discussed based on a time-temperature, load-displacement curve, damage mode, crack pattern, and plastic strain.

4.2 Validation of Finite Element Analysis

To ensure the accuracy of the developed numerical model and the data collected from literature, the numerical model was validated against experimental tests carried out on GFRP SIP formwork concrete bridge decks subjected to fire.

The numerical simulation results obtained from the suggested model were compared with the experimental tests results and further parametric studies are conducted in this paper. The section below describes the experimental tests used in the validation of the current numerical model, validation of the numerical model against the thermal test,

validation of the numerical model against structural test at room temperature and elevated temperature.

4.2.1 Validation of numerical model against the thermal test

The results obtained from heat transfer analysis were presented in terms of temperature-time- histories of GFRP internal temperature at the soffit center and compared with temperature-time- histories of corresponding experimental thermal tests(Nicoletta et al., 2019). Fig. 4.1 and 4.2 show the temperature distribution predicted by the FE model and the relevant experimental data. The model estimates the temperatures of the GFRP very closely with the experimental one. The maximum predicted peak temperature is about 104 and 100 °C by numerical simulation and experimental tests respectively. The percentage of the difference between numerical simulation and the experimental test is 3.8% which is below 10% and acceptable. Therefore, the comparisons show reasonable agreement between the numerical simulation results and the experimental test results, especially at maximum temperature transferred from the soffit of GFRP to the internal surface of GFRP. This agreement indicates the accuracy of the suggested model in capturing the temperature distribution inside the GFRP SIP formwork concrete bridge deck Crossection.

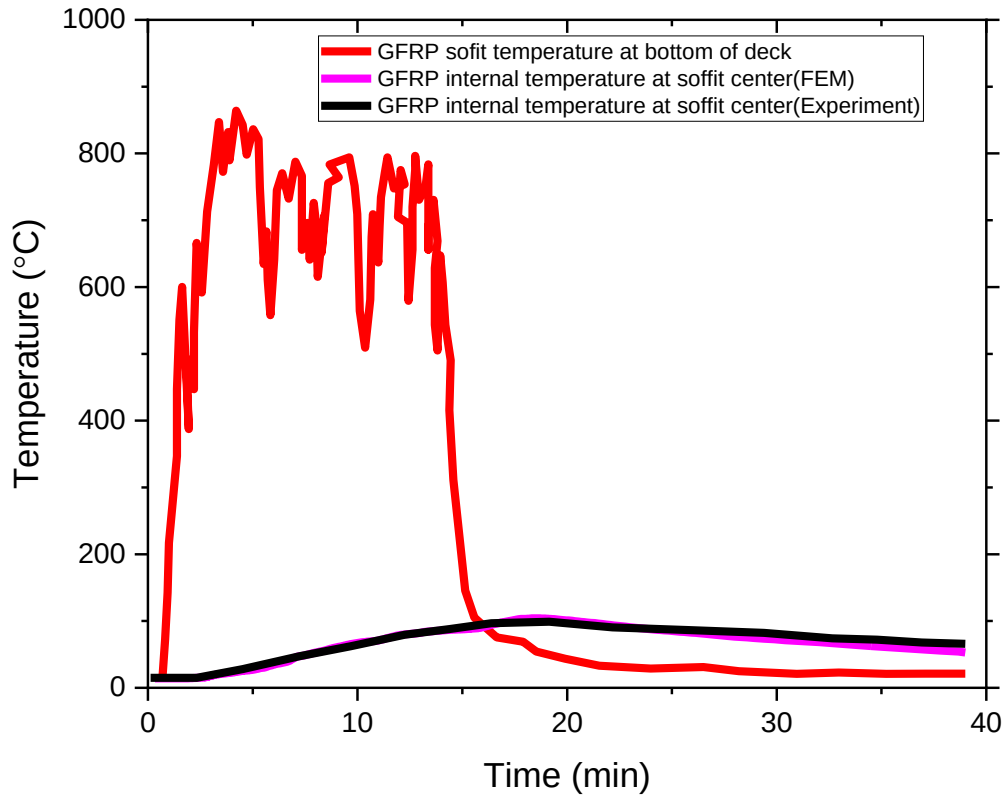

Figure 4.1: Temperature distribution predicted by the FE model and experimental data.

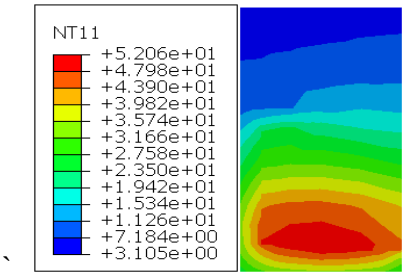

Figure 4.2: Temperature evolution of concrete bridge deck across a critical section.

4.2.2 Validation of numerical model against structural test before the fire

The mechanical behavior of concrete bridge decks is first investigated at room temperature to study the behavior of the concrete decks at ambient temperature. The load-displacement curves and failure modes obtained from finite element analysis and experimental results were analyzed and compared. As shown in Fig. 4.3a, the load-displacement curves obtained for specimen C1 from FE analysis were in good agreement with experimental results. However, did not show any failure mode without implementing failure material of pultruded GFRP to the finite element model.

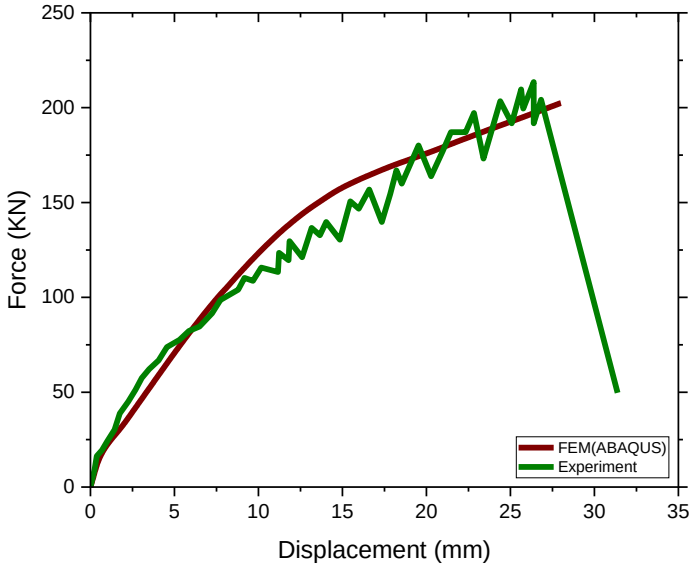

Figure 4.3: Load-deflection response of numerical and experimental result for specimen C1 without providing failure criteria of Pultruded GFRP

Figures 4.4a and b illustrate load versus deflection of the concrete decks of specimen C1 and C2 respectively providing failure material into FEM and it captures both ultimate load and failure modes with experimental tests. This agreement confirms that the proposed numerical model can estimate and predict the response and maximum load of GFRP SIP formwork concrete bridge decks under load at room temperature up to failure. The analyzed ultimate strength of specimen C1 was about 209.1 KN, accounting

for 98.58% of the experimental result. The analyzed ultimate strength of specimens C1 was lower than the experimental result with 1.42%. Additionally, the numerical results showed slightly fair displacement corresponding to the ultimate strength at failure compared with the experimental result. The ultimate displacement obtained by finite element analysis is about 29 mm which has a percentage of difference of 11.37% compared with an ultimate displacement of the experimental result of 25.7 mm. This may be due to the inaccurate simulation of friction and bonding effect. But the finite element model could still be used to capture the load-displacement behavior. Similar, the specimen C2, the ultimate load obtained by FEM is 438 KN accounting for 92.21% of the experimental result. The analyzed ultimate load of specimen C2 was lower than the experimental result with 7.79%.

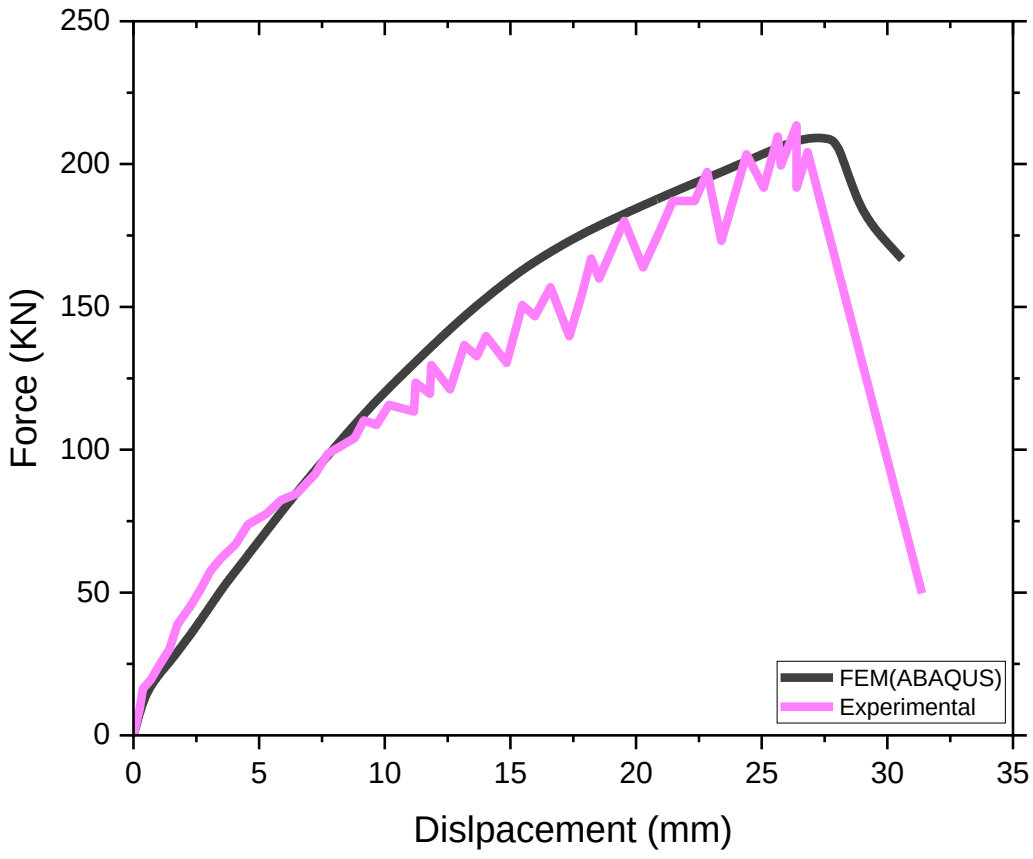

(a)

The ultimate displacement measured by FEM was 25.67 mm with a 13.57% percentage of difference compared to experimental measured maximum displacement. In general, the finite element model has good agreement with the experimental result since it captures both the ultimate load and displacement of the concrete bridge deck at room temperature.

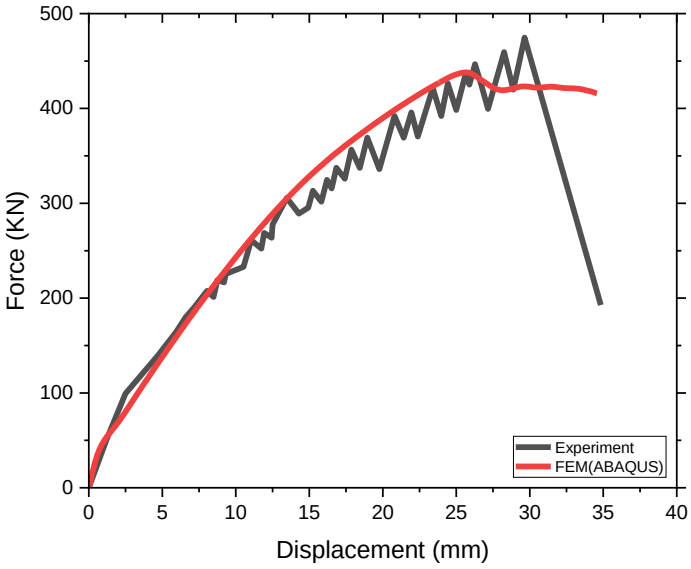

(b)

Figure 4.4: Load-deflection response of numerical and experimental result for specimen C1 and C2 with providing failure criteria of Pultruded GFRP

4.2.3 Validation of numerical model against structural test after the fire.

The mechanical behavior of concrete bridge decks at elevated temperatures is also investigated to study their behavior when subjected to fire. The results of the numerical model in terms of ultimate load-displacement relationships of the concrete bridge deck were compared with the corresponding experimental load-displacement relationships. Figures 4.5 below illustrate the comparison for the concrete bridge deck between finite element analysis and experimental results. Good agreement can be seen between the two sets of results. This agreement confirms that the proposed numerical model can estimate and capture the response and maximum load of the concrete bridge deck under different elevated temperatures up to failure. However, did not show any failure mode due to material failure Hashin damage of pultruded GFRP for the solid element is not supported in ABAQUS/Standard. The effect of implementing Hashin damage of fiber-reinforced polymer into the FEM did not affect the ultimate load of the concrete bridge deck as illustrated in figure 4.3 above but have effects on showing the mode of failure. Therefore, in this during thermomechanical modeling of the concrete bridge deck, these effects were neglected. Numerical simulation results reveal that the maximum load of fire-damaged concrete bridge deck FD was found to be increased by 8.67% compared to the maximum load of undamaged concrete bridge deck C1. This shows that there is some level of strengthening, because of heating and cooling of the pultruded GFRP

which results in concrete prestressing. This result can also validate the experimental work of (Nicoletta et al., 2019).

Figure 4.5 illustrates the load-deflection response of fire-damaged concrete bridge deck specimen FD. The finite element result captures the ultimate load of the concrete bridge deck in comparison with the experimental result shows good agreement. This agreement confirms that the proposed numerical model can estimate and predict the response and maximum load of GFRP SIP formwork concrete bridge decks subjected to fire. The ultimate strength of fire-damaged deck specimen FD obtained by finite element model was 228.85 KN, accounting for 95.35% of the experimental result. The analyzed ultimate strength of specimens was lower than the experimental result within 4.64%. Additionally, the numerical results showed slightly fair displacement corresponding to the ultimate strength at failure compared with the experimental result. The difference in the ultimate strength of the finite element model and the experimental result had 1.27%.

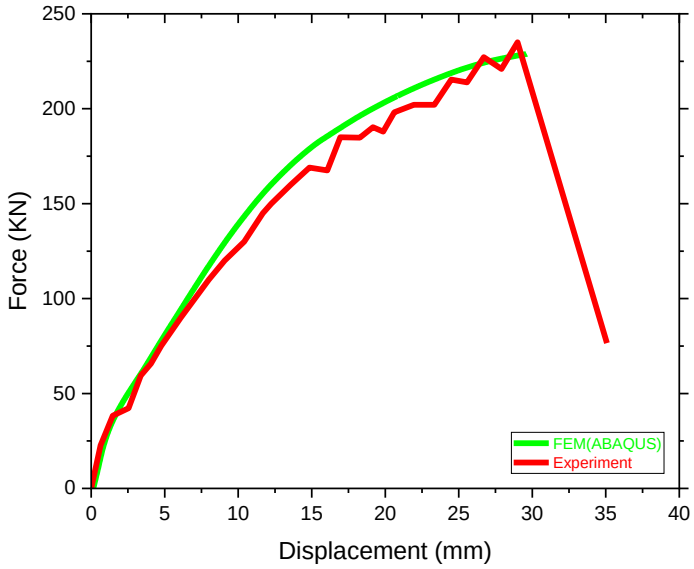

Figure 4.5: Numerical versus experimental load-deflection response of concrete deck after exposed to fire for specimen FD

In table 4.1 the summary of the percentage of error and the mean model accuracy of predicted results obtained by FEM and experimental results based on the ultimate displacement at mid-span and ultimate load of the concrete bridge deck is described. The following equations were directly taken from(YIMER, 2019).

$$Error = \left|\frac{FEM_{result} - Test_{result}}{Test_{result}}\right| \times 100 \qquad (4.1)$$

$$\text{Mean model accuracy, M}(\%) = \frac{FEM_{result}}{Test_{result}} \times 100 \quad (4.2)$$

Table 4. 1: Comparison of ultimate displacement and load of concrete bridge deck with the experimental result.

Specimen	Ultimate displacement at mid span(mm)		Prediction	Ultimate load(KN)		Prediction	
	Experi-mental	FEM	Percentage difference (%)	Experimental	FEM	Error (%)	M (%)
C1	25.7	29	11.37	212	209	-1.42	98.58
C2	29.7	25.67	13.57	475	438	-7.79	92.21
FD	30	29.62	1.27	240	228.85	-4.64	95.35

As illustrated in table 4.1 above in all cases, the finite element model prediction of percentage difference of the ultimate displacement at mid-span and ultimate load error leads to below 15% and 10% respectively, which shows that the finite element response is in good agreement with the experimental result.

4.2.4 Cracking pattern

The concrete damaged plasticity model in ABAQUS assumes that the initiation of cracking is due to the positive maximum principal plastic strain (PE). The orientation of the cracks is considered to be normal to the maximum principal plastic strains (PE) and thus, the direction of the cracking is visualized through the maximum principal plastic strains. The maximum tensile principal stresses are also can be used to show the cracking patterns in finite element analysis. However, the maximum plastic equivalent principal strain can give a better visualization of crack direction on concrete surfaces. Therefore, it's necessary to use strain for showing the cracking patterns for the finite element analysis (Genikomsou & Polak, 2015).

The cracking pattern on the tension side of the concrete bridge deck specimen C2 at a failure is presented in figure 4.7 with the comparison between the finite element model and experimental test. The cracking propagates to the compression zone of the concrete bridge deck from the interface between concrete and pultruded GFRP. It starts tangentially near the interface of concrete and pultruded GFRP and then extends radially as the applied load increase. The presence of top reinforcement changes the behavior of cracking and prevents the propagation of cracking further to the compression zone of the deck. Overall, the finite element cracking patterns were in good agreement with the experimentally obtained crack patterns.

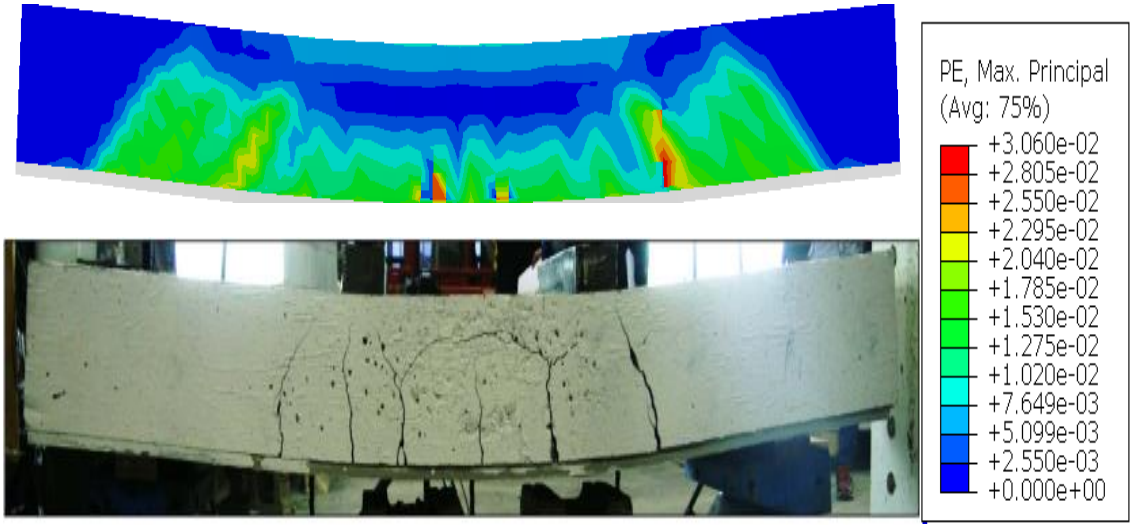

Figure 4.6: Cracking pattern at the ultimate load between finite element model and experimental test for specimen C2.

The crack pattern of specimen C1 and fire-damaged FD obtained from finite element analysis were illustrated in figure 4.7. The author(Nicoletta et al., 2019) did not present the image of a crack pattern of the fire-damaged FD during the experimental test in his published paper but well describe theoretically the difference between the undamaged and fire-damaged concrete deck based on their variation of the crack pattern. Therefore, in this study based on the theoretically addressed in the literature, the crack pattern obtained by finite element analysis were compared and discussed below.

To better understand the influence of fire on load transfer to the GFRP stay-in-place formwork concrete bridge deck finite element analysis was applied to visualize the crack pattern in specimens C1 and FD. As illustrated in Figures 4.7a and b the most prominent flexural cracks occurred at the mid-span of the deck between the two loading plates and the shear cracks were developed nearest to the two supporting radiating from the interface between concrete and pultruded GFRP. Furthermore, for the same applied load; the fire-damaged FD had smaller crack width than undamaged C1. This shows that better load transfer to the GFRP stay-in-place formwork in fire-damaged FD than in undamaged C1 as a result of concrete precompression due to thermal straining. Overall, the crack pattern obtained by finite element analysis of concrete bridge at room temperature and subjected to fire well agree with the experimental work of (Nicoletta et al., 2019).

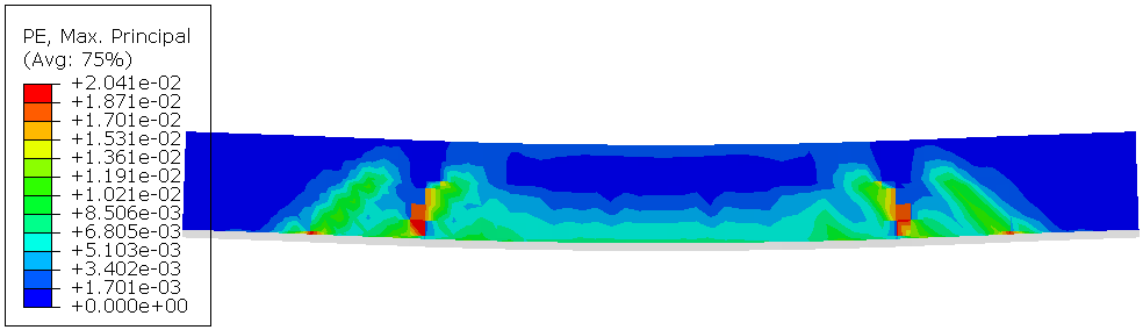

(a)

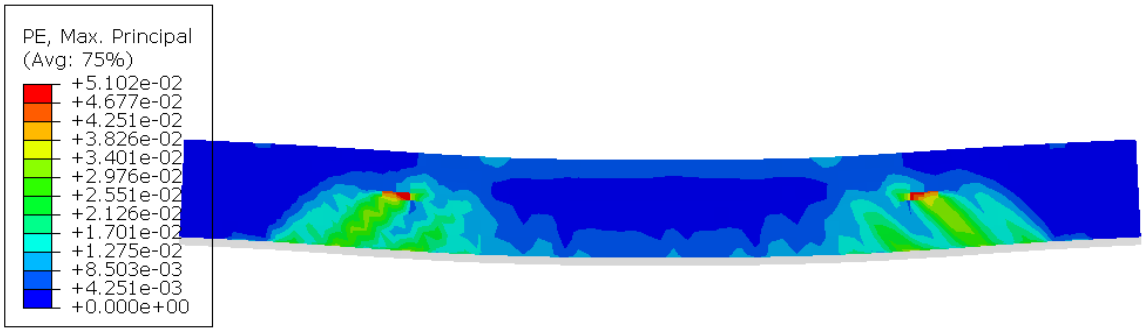

(b)

Figure 4.7: Cracking pattern for (a) specimen C1 and FD

4.3 Parametric study

Various parameters that affect the performance of the GFRP SIP formwork concrete bridge deck under fire were investigated by the finite element model. The parameters were types of aggregates (siliceous and carbonate), duration of the fire, types of fire (hydrocarbon and standard fire), sustained load, deck width, GFRP plate length, GFRP plate thickness, span to depth ratio, and heating and cooling phase

4.3.1 Effect of aggregate type on concrete deck

This parametric study was conducted to investigate the influence of aggregate types on temperature evolution of concrete surface, load-deflection response, tension damage, compression damage, and crack pattern of concrete bridge deck subjected to pool fire. In this study siliceous and carbonate, aggregates were used for concrete deck specimen C1 and other parameters were kept the same. The effects of aggregate type on the predicted temperature of the concrete surface at mid-span of the concrete deck with a specified distance of 19 mm from the base of the concrete bridge deck cross-section are illustrated in figure 4.8.

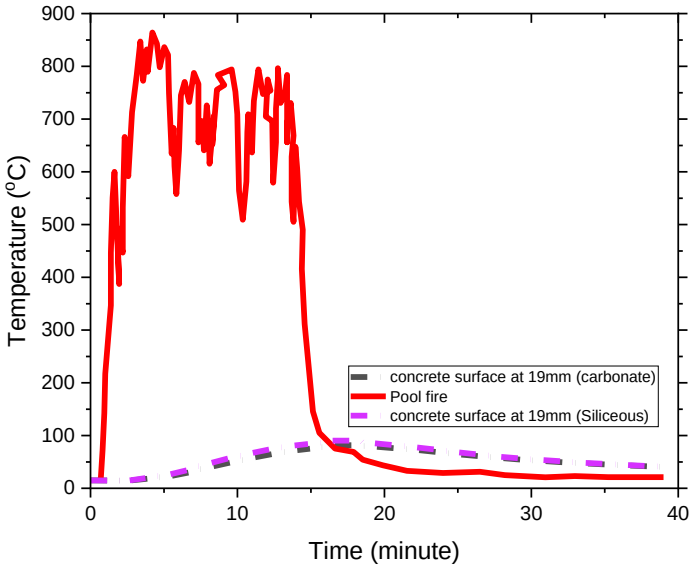

Figure 4.8: Effect of aggregate types on temperature evolution of the concrete deck

The result presented in figure 4.8 shows the types of aggregates do have not a significant influence on the predicted temperature of the concrete deck. The peak temperature predicted on the concrete surface for carbonate and siliceous aggregate is about 82 and 91 °C respectively.

Figure 4.9 illustrates the effect of aggregate types on the load-deflection response of the concrete bridge deck. It can be seen that with different types of aggregate the deflection mode of the concrete bridge is the same for both carbonate and siliceous concrete decks. Additionally, the initial cracking load in both carbonate and siliceous occurred around 30 KN. However, aggregate types have a little or low influence on the ultimate load-carrying capacity of the concrete bridge deck. The ultimate load of the concrete bridge deck consists of siliceous aggregate less than those of the concrete deck made of carbonate aggregates. The predicted ultimate load of the concrete bridge deck is about 230 and 226 KN for carbonate and siliceous aggregate respectively. This is due to the reduction in compressive strength of the concrete consists of siliceous aggregates more than carbonates aggregate at elevated temperature. In general, aggregate types did not have significant effects on predicted temperature and ultimate load-carrying capacity of concrete bridge deck subjected to fire.

As illustrated in Figures 4.10a and b the mode of cracking failure of the concrete bridge deck consists of siliceous and carbonate aggregates almost similar. Therefore, in both cases, the cracking propagates from the interface between concrete and GFRP T-up ribs to the compression zone of the concrete deck and radiates to the compression zone of

the concrete deck up to the presence of the embedded top GFRP reinforcement and GFRP T-up ribs.

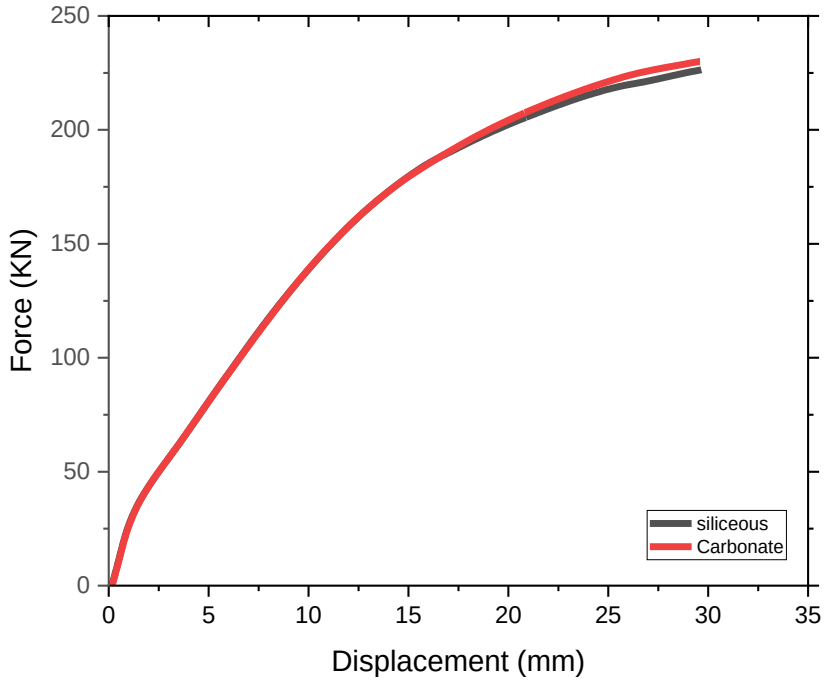

Figure 4.9: Effect of aggregate types on the load-deflection response of concrete bridge deck.

This indicates that the presence of the GFRP T-up ribs and top reinforcement prevents the damage of concrete above the ribs from fire damage and further cracking of the concrete as applied load increases. However, the maximum plastic deformation and crack width were observed for the deck consists of siliceous aggregates more than the carbonate aggregates. This is because the siliceous aggregates are relatively less fire-resistant than carbonate aggregates.

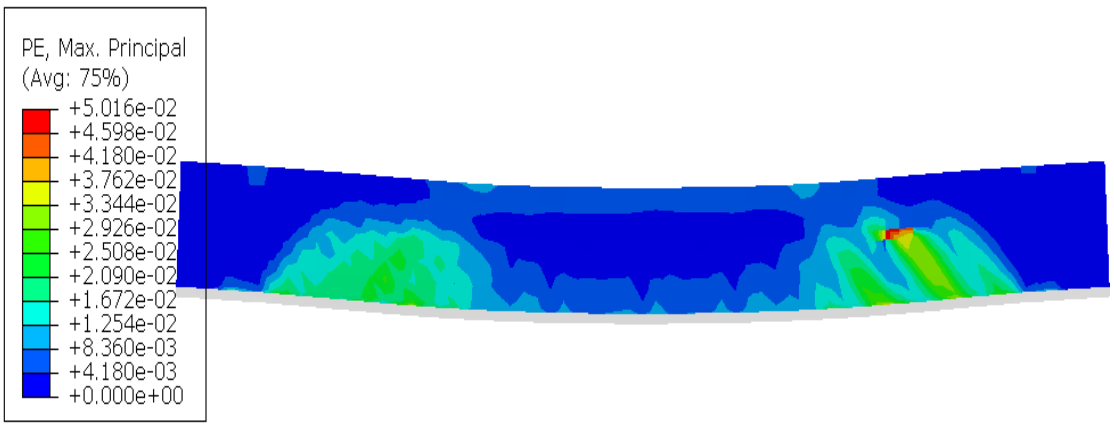

(a) Maximum principal plastic strain for siliceous aggregates

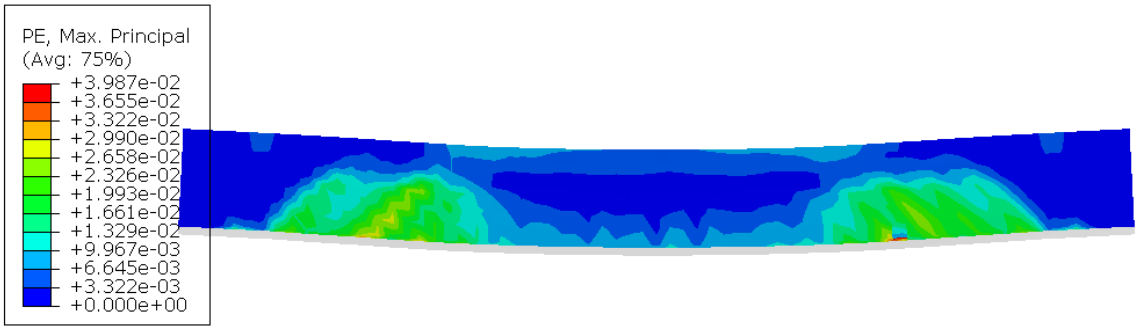

(b) Maximum principal plastic strain for carbonate aggregates

Figure 4.10: Effect of aggregate types on the maximum principal plastic strain and cracking failure pattern of concrete

Figures 4.11a and b illustrate the observed tensile damage of the concrete bridge deck consisting of siliceous and carbonate aggregates. In both concrete bridge decks, the most severe damage of the deck is at the tension zone of the deck subjected to pure bending under combined thermal and mechanical load. There was also a wider spread of tensile damage at shear span supports. It's observed that the spalling of concrete at top of the deck nearest to the loading point occurred with a little difference in the concrete deck consisting of siliceous aggregates. Therefore, based on the tension damage observed the aggregate types do not have a notable effect on fire-damaged concrete bridge decks.

The pultruded GFRP Mises stress contours observed for concrete bridge deck made up of different aggregates types subjected to fire were illustrated in figure 4.12a and b. This result indicates that the maximum Mises stress on pultruded GFRP T-up ribs is more concentrated at the soffit of the GFRP base plate between two loading plates.

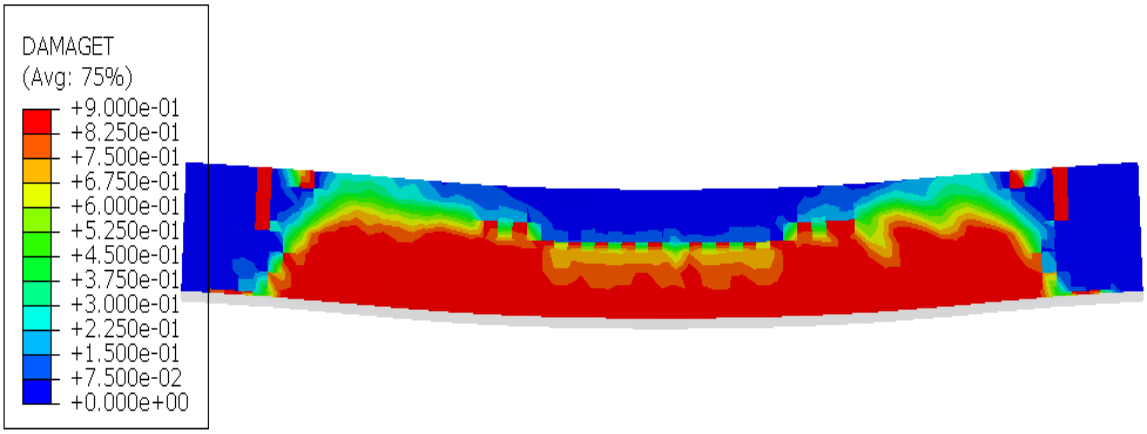

(a) Tension damage of concrete deck consists of siliceous aggregate

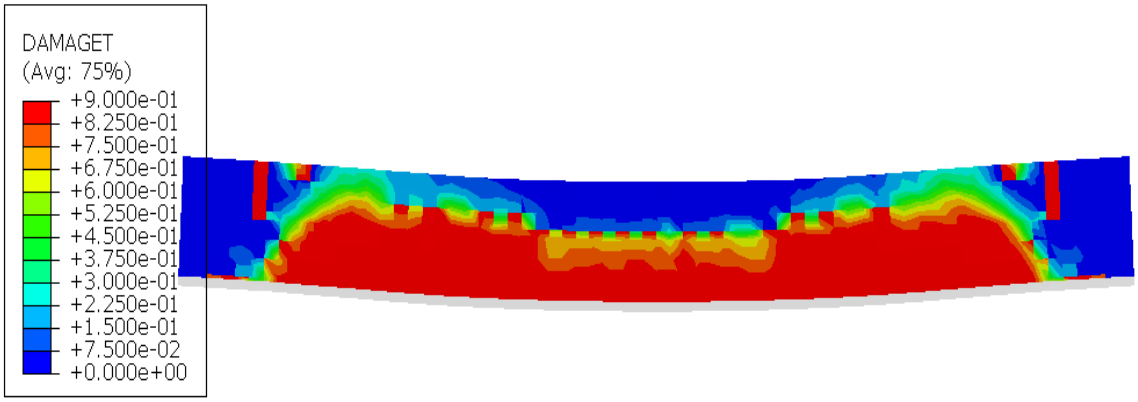

(b) Tension damage of concrete deck consists of carbonate aggregate

Figure 4.11: Effect of aggregate types on tension damage of concrete bridge deck

The concrete bridge deck consists of siliceous aggregates relatively more experienced GFRP T-up ribs Mises stress at the bottom soffit of the deck. The maximum Mises stress on T-up ribs of concrete bridge deck with siliceous and carbonates were 176.3 and 175.5 N/mm^2 respectively. In general, also the aggregate types have very small or a little effect on maximum mises stress developed on GFRP SIP formwork concrete bridge decks.

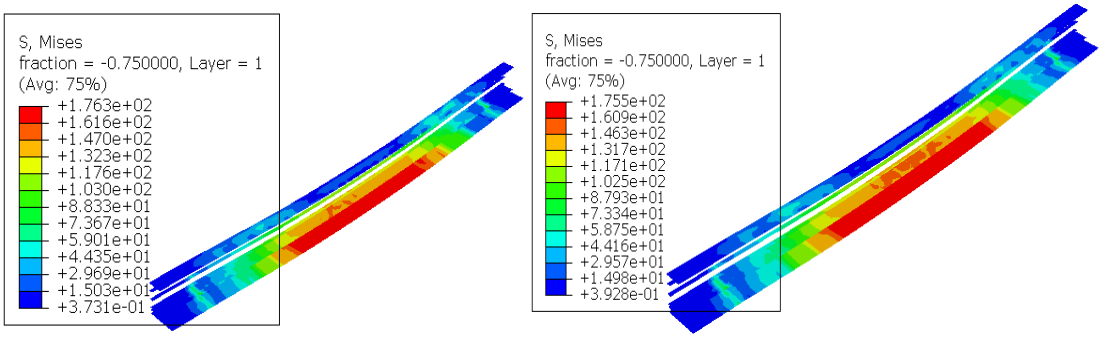

(a) Mises stress using siliceous aggregate (b) Mises stress using carbonate aggregate

Figure 4.12: Pultruded GFRP Mises stress at different types of aggregates

4.3.2 Effect of fire duration on the concrete bridge deck

This parametric study was performed to evaluate the effect of fire duration on temperature evolution, load-displacement response, damage, crack pattern, and Mises stress of concrete bridge deck exposed to fire. Fire duration of one and two hours was used in this study following the time-temperature curve of standard fire according to Eurocode. During this parametric study, the fire was exposed to the full span length of the concrete bridge deck between the two supports for a variable time. The effect of fire duration on temperature predicted can be illustrated as in figures 4.13a and b.

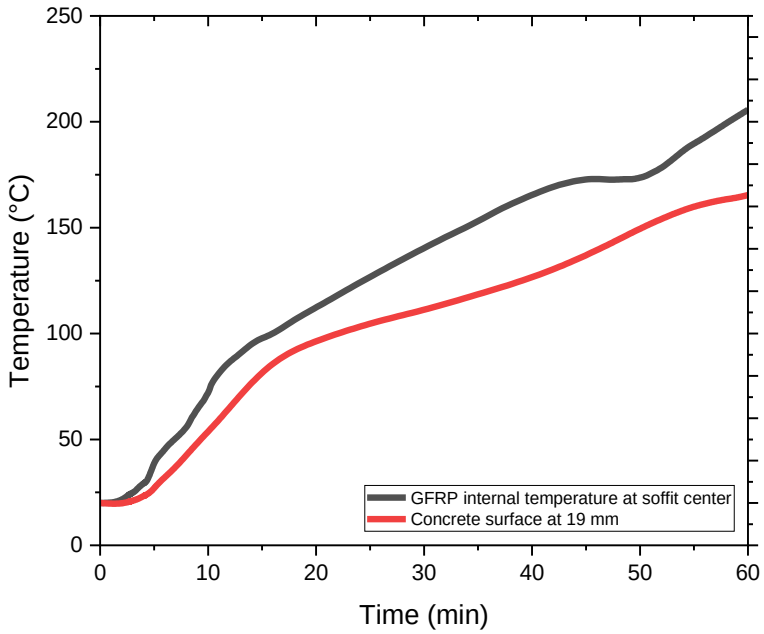

(a) Predicted temperature evolution at 60min of standard fire

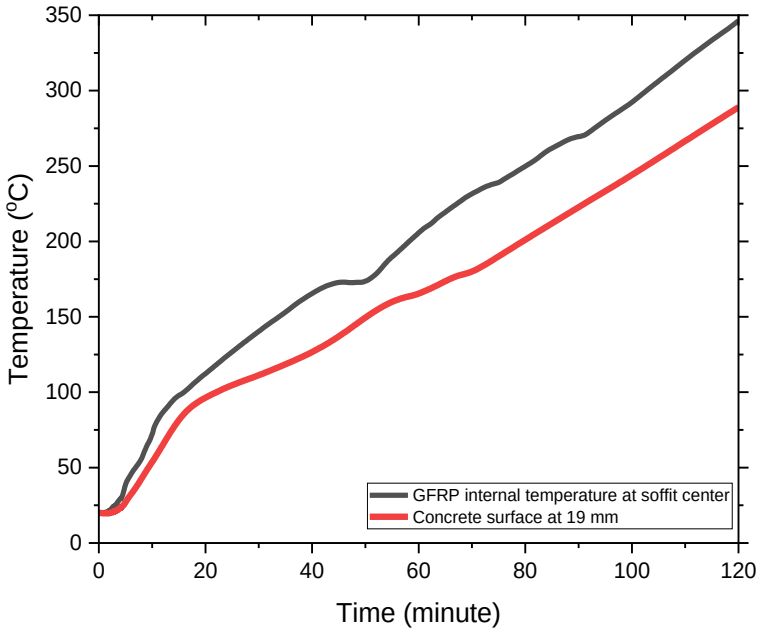

(b) Predicted temperature evolution at 120 min of standard fire

Figure 4.13: Effect of fire duration on temperature evolution of concrete bridge deck

It can be observed from Figures 4.13a and b the fire duration significantly influences the predicted temperature of pultruded GFRP and concrete with a peak temperature of about 205 and 165 °C exposing the fire for 60 minutes standard fire (ISO 834). Similarly, for 120 minutes of fire exposure, the predicted temperature were 346 and 289 °C on pultruded GFRP and concrete surface respectively. This result indicates that from the first 20 min heating rate temperature evolution of concrete bridge deck on pultruded

GFRP and concrete surface close to each other, and the temperature of GFRP T-up ribs rapidly increases at about 50 min. This is due to the thermal conductivity of the material that is above the decomposition temperature (300 °C) the thermal conductivity of the pultruded GFRP increases rapidly to a very high level which validates the experimental test conducted by(T. Keller et al., 2006b).

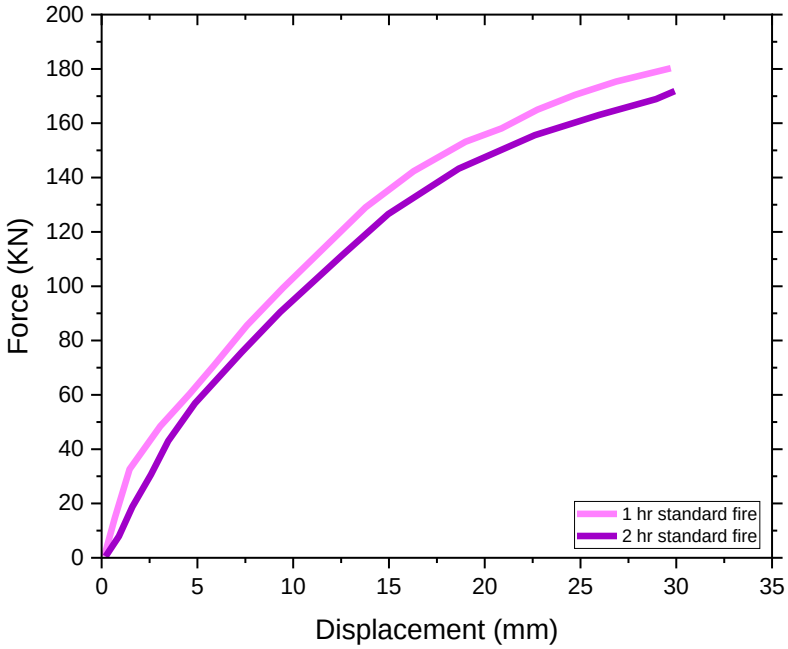

Figure 4.14: Effect of fire duration on load-deflection response of concrete bridge deck

It can be seen from figure 4.14 that with different fire duration the deflection mode of the concrete bridge is the same. However, with increased fire duration the ultimate load-carrying capacity of the concrete bridge deck is reduced. The ultimate load of the concrete bridge deck exposed to fire for 60 and 120 minutes are less than those of the control concrete deck which are investigated without exposure to fire at room temperature. The reduction in ultimate load for concrete bridge deck is about 15 and 19% respectively of the reference concrete deck specimen C1. This is due to high thermal load resulting in excessive deflection, loss in strength, and stiffness of concrete and pultruded GFRP. Also, the reduction in strength of concrete deck subjected to standard fire is as a result of no thermal heating and cooling phase was considered which result in precompression of the concrete compared with the deck subjected to the pool fire mentioned in this study. Overall, the fire duration has a significant effect on ultimate load carrying capacity and the stiffness of concrete bridge decks subjected to different fire duration.

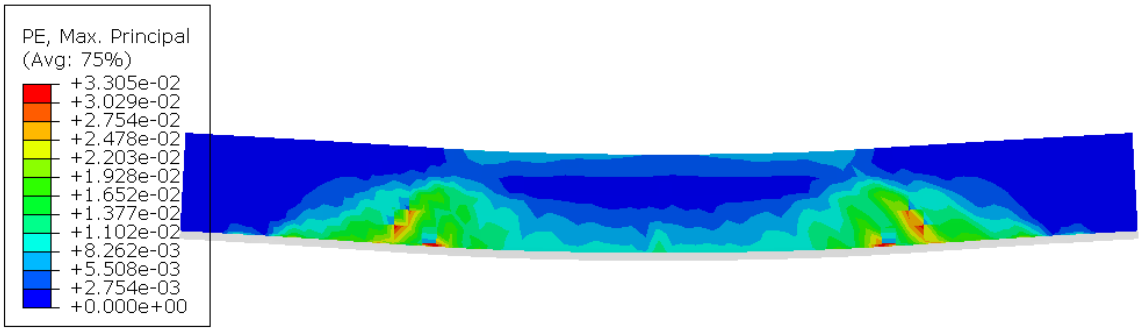

(a) Maximum principal plastic strain at 60 minutes of standard fire

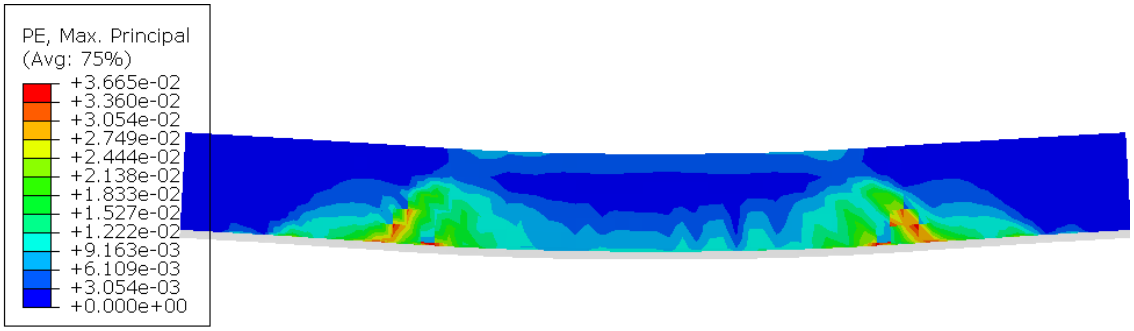

(b) Maximum principal plastic strain at 120 minutes of standard fire

Figure 4.15: Effect of fire duration on the maximum principal plastic strain and crack pattern of the concrete bridge deck.

Figure 4.15a and b illustrate the plastic strain distribution and cracking failure pattern obtained from finite element analysis for the concrete bridge deck subjected to standard fire for a period of one and two hours respectively. In ABAQUS it is possible to visualize the crack pattern by using the maximum principal plastic strain (PE), in which the material constitutive model is defined as cracking strain. The cracking pattern was observed at the interface between pultruded GFRP and concrete in both cases. However, the concrete deck subjected to two-hour standard fire experiences higher plastic deformation than the deck exposed to one hour and the crack is further growth to compression zone. The result indicates that the concrete deck subjected to fire for a long period increases the occurrence of cracking at interfaces and concrete crushing at the compression zone.

The tensile damage contours illustrated in Figures 4.16a and b were obtained from finite element models for specimen C1 subjected to the standard fire of one and two hours respectively. In both cases, the tensile damage was initiated at extreme tension fiber of the concrete deck in zones subjected to pure bending. There was a wider spread of tensile damage around the loading point and shear span supports. The tensile damage

of the concrete deck was more concentrated under the loading points. It's observed that the presence of the top reinforcement and pultruded GFRP prevents the tensile damage of the concrete at the compression zone. The only difference in tensile damage of the concrete deck in both cases was the degree of tensile damage.

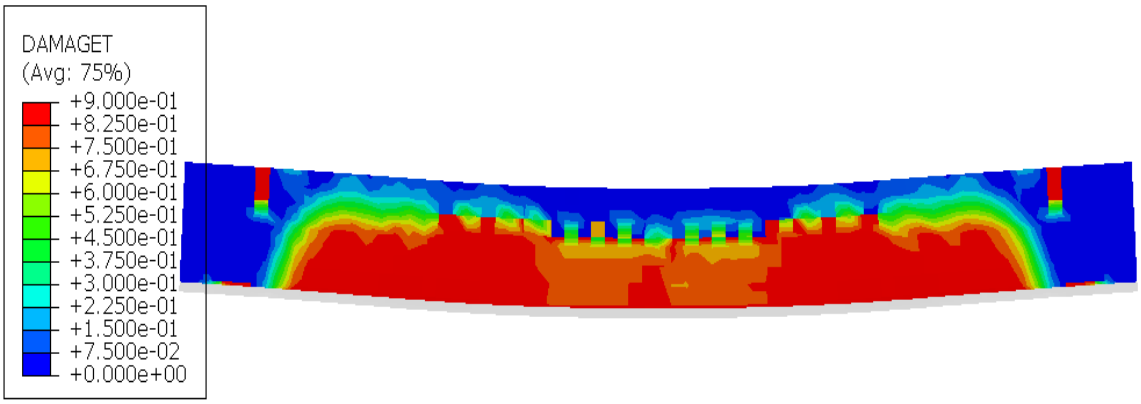

(a) Tension damage at 60 minutes of standard fire

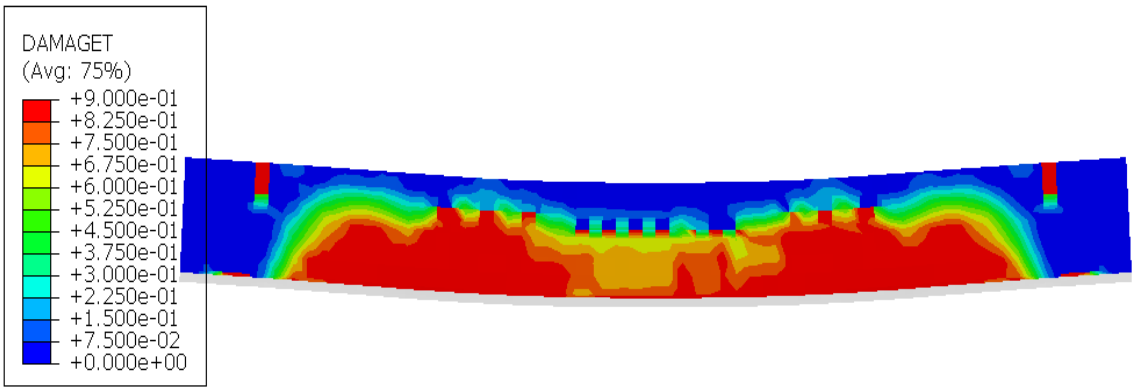

(a) Tension damage at 120 minutes of standard fire

Figure 4.16: Effect of fire duration on tension damage of concrete bridge deck

The effect of fire duration on the Mises stress distribution of pultruded GFRP is illustrated in Figures 4.17a and b for different fire duration of the same fire types. As observed from the contour plot; when the concrete bridge deck is subjected to fire for 60 minutes of standard fire the Mises stress on pultruded GFRP is more concentrated at the web of the ribs while for 120 minutes of fire exposure; it's more concentrated across the soffit of the deck towards the web of the ribs. This is due to the rapid rise in temperature of the GFRP above the decomposition temperature of about (300 ^{o}C). The fire duration significantly influences the predicted Mises stress of pultruded GFRP. The peak Mises stress recorded for 60 and 120 minutes on the ribs were 142.5 and 112.9 N/mm^2 respectively.

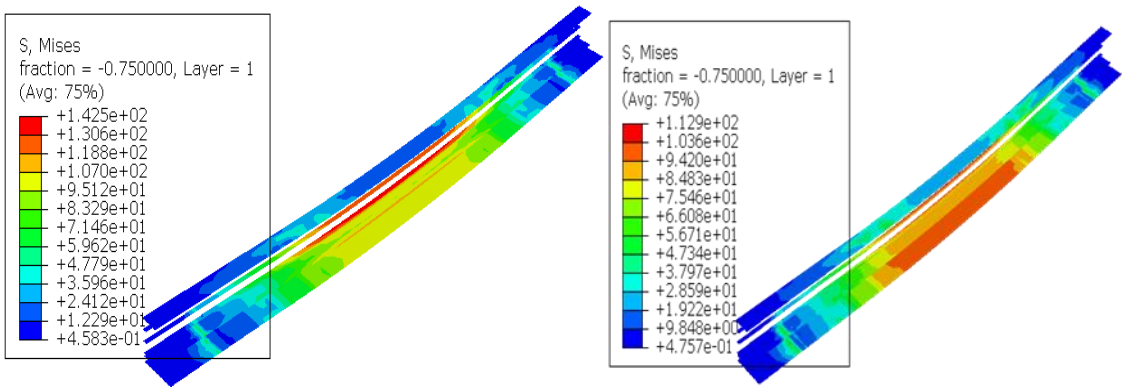

(a) Mises stress at one hour standard fire (b) Mises stress at two-hour standard fire

Figure 4.17 Effect of fire duration on Mises stress of pultruded GFRP

4.3.3 Effect of Fire Scenarios on the concrete bridge deck

The influence of fire scenarios was studied to determine the effect of fire type on the performance of GFRP SIP formwork for concrete bridge decks subjected to fire. In this study, hydrocarbon and standard fires (ISO 834) according to Eurocode were selected. The fire was applied at the soffit of concrete decks between two supports for one and two hours. The temperature distribution of the internal temperature of GFRP base plate at soffit center, concrete surface, load-deflection response, and Mises stress of the GFRP SIP formwork concrete bridge decks are compared and illustrated in figure 4.18 to 4.22.

As expected in Figures 4.18a and b, the predicted time-temperature evolution of pultruded GFRP base plate and concrete surface is higher with hydrocarbon fires in comparison with the standard fires. The predicted GFRP base plate of the concrete deck at fire exposure of 60 minutes was about 352 and 206 °C using hydrocarbon and standard fire respectively. This is due to the rapid increase in temperature within the first 10 minutes of hydrocarbon fires, as the standard fire temperature increases gradually. The predicted GFRP base plate internal temperature with both fire types is very close at the initial stage of heating rates of about 20minutes. Above this time range, the concrete surface temperature is greater with hydrocarbon fires, with the maximum recorded temperature of about 306 °C under hydrocarbon fire and 289 °C under standard fire for a similar fire exposure time of 60 minutes. Therefore, the effect of fire scenarios becomes more significant on the temperature evolution of concrete decks

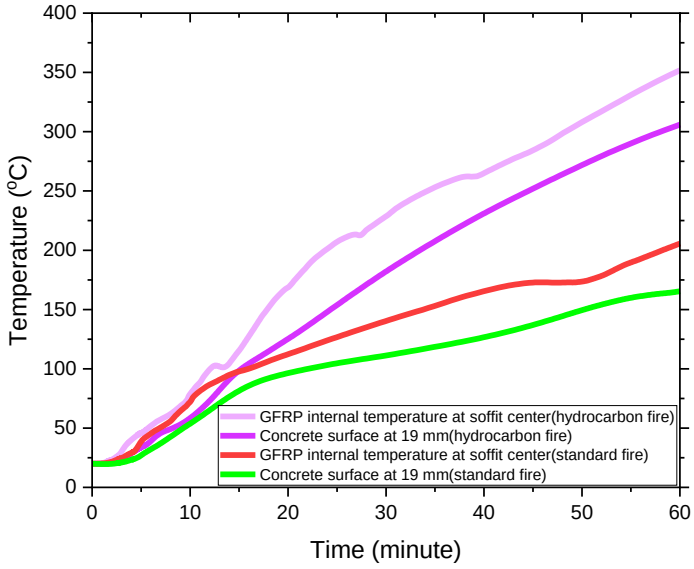

(a) Predicted temperature evolution at 60 minutes of standard and hydrocarbon fire

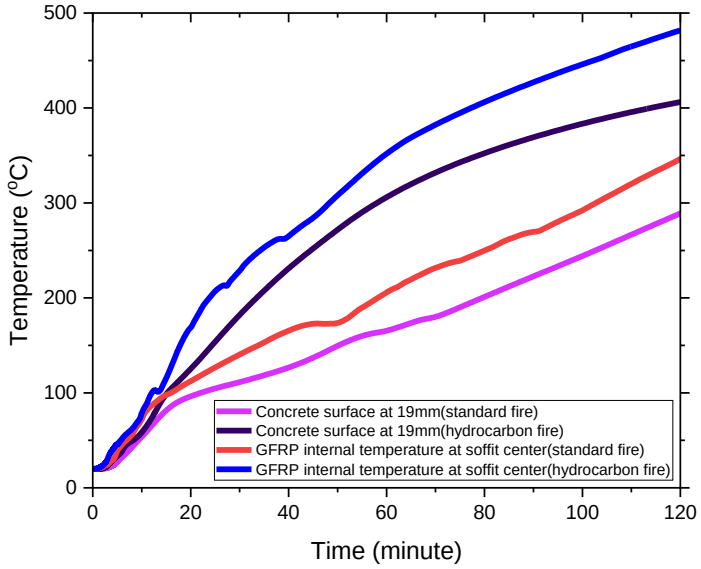

(b) Predicted temperature evolution at 120 minutes of standard and hydrocarbon fire

Figure 4.18: Effect of fire scenarios on temperature evolution of concrete bridge deck

From figure 4.19 the ultimate load-carrying capacity of the concrete bridge deck is much higher under the standard temperature fire curve (ISO834), with the ultimate load of 180 KN. In comparison, 172 KN ultimate loads were obtained under hydrocarbon fire. Compared to undamaged specimen C1 the reduction in ultimate load of fire-damaged specimen C1 was 13.9 and 17.7 % under standard and hydrocarbon fire respectively.

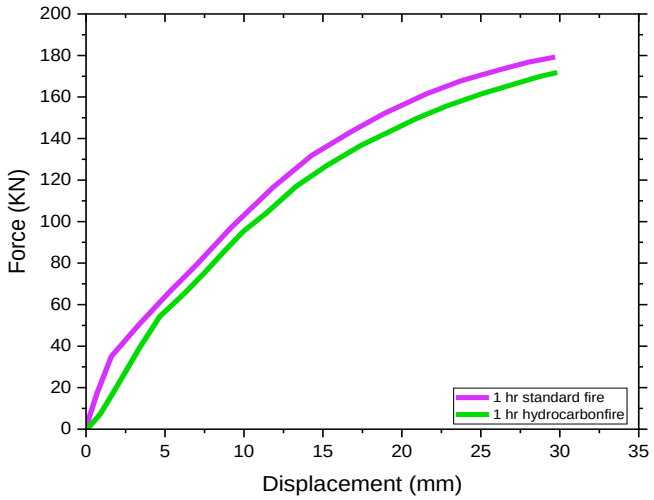

Figure 4.19: Effect of fire scenarios on the load-deflection response of the concrete deck

This reduction in load-carrying capacity was due to the rapid rise in temperature of pultruded GFRP and concrete, which leads to a significant loss in stiffness, strength, and load-carrying capacity of the concrete bridge deck.

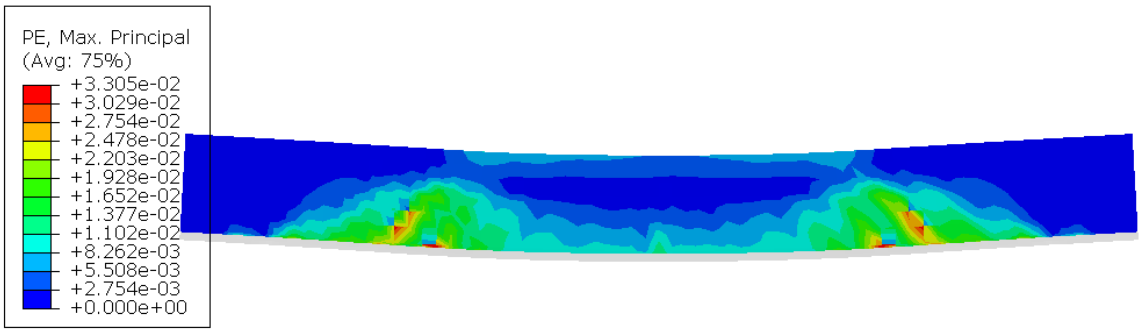

(a)Maximum plastic strain at 60 minutes of standard fire

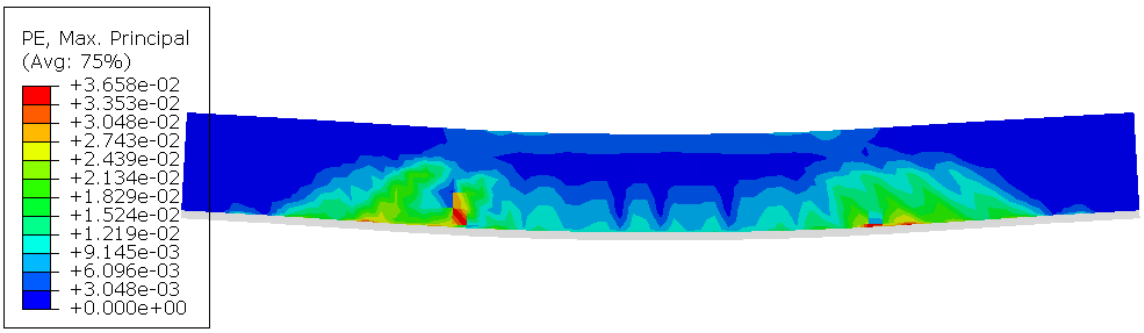

(b)Maximum plastic strain 60 minutes of a hydrocarbon fire

Figure 4.20: Effect of fire types on the maximum plastic strain and cracking failure pattern of the concrete bridge deck

Generally, the result indicates that the type of fire scenarios has a notable effect on the performance of concrete bridge decks subjected to fire.

Figures 4.20a and b show the maximum plastic deformation of the concrete bridge deck subjected to different fire types of the same duration. The concrete bridge deck subjected to hydrocarbon fire experienced the maximum value of plastic deformation than standard fire. As observed the shear crack in both cases was developed nearest to the supporting under the loading points, there difference is the initiation of the crack width. The width and growth of the cracks to the compression zone of the concrete deck are more developed on the concrete deck subjected to hydrocarbon fire. And also the flexural crack developed at mid-span of the deck between the two loading points with several cracks on concrete bridge deck subjected to hydrocarbon fire than standard fire. This is due to a rapid rise in the temperature of hydrocarbon fire with a short period.

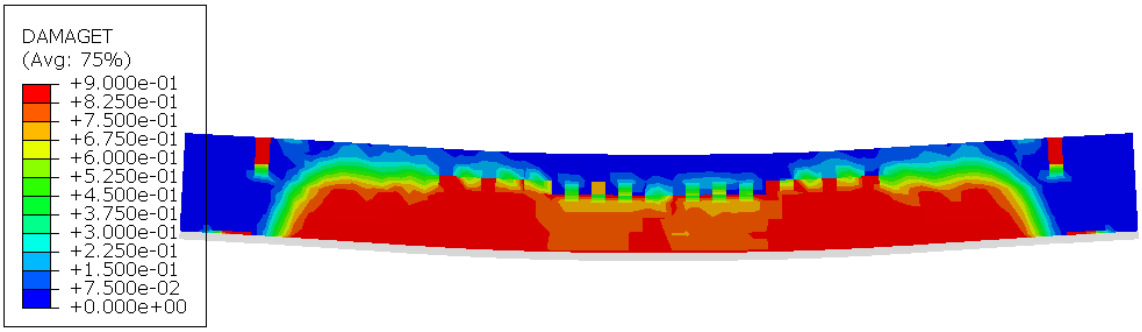

(a) Tension damage at 60 minutes of standard fire

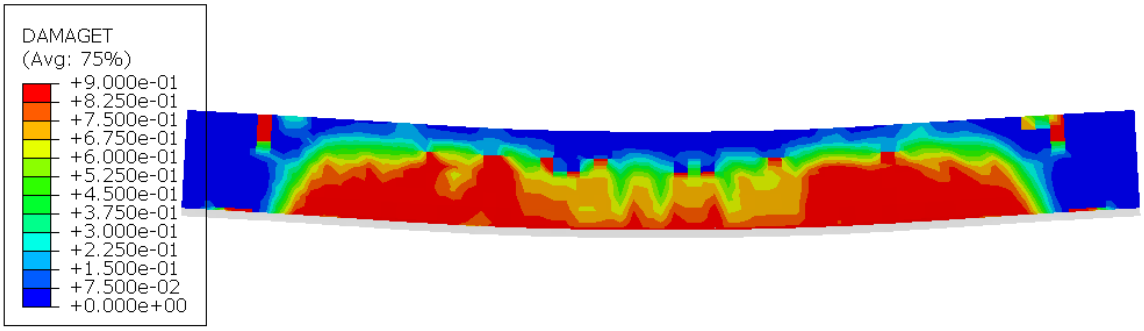

(b) Tension damage at 60 minutes of a hydrocarbon fire

Figure 4.21: Effect of fire types on tension damage of concrete bridge deck

The effect of fire types on tension damage of the deck was illustrated in Figures 4.21a and b. The fire types have a little effect on the tension damage of the concrete bridge deck with observed damage of the deck at the tension fiber. The concrete deck subject-

ed to hydrocarbon, fire shows a small degree of tension damage of the concrete deck above GFRP T-u ribs.

Figure 4.22 shows the pultruded GFRP mises stress when the concrete bridge deck is subjected to one-hour standard and hydrocarbon fire at the soffit of the deck between two supports. The concrete bridge deck exposed to fire at the soffit of the deck with different fire types of the same duration experiences different mises stress on pultruded GFRP and the Mises stress is more concentrated at the web of GFRP T-up ribs in both cases. However, the maximum mises stress due to a standard fire and hydrocarbon fire on pultruded GFRP are about 142.5 and 120.3 N/mm^2 respectively. This indicates the concrete bridge deck resists high ultimate load under standard fire experienced larger pultruded GFRP mises stress developed in the web of GFRP T-up ribs than stress developed at the soffit of GFRP base plate and flanges of GFRP T-up ribs. The mises stress used to determine the given material will yield or fracture. The GFRP did not the yield point, however, it can be rupture or fracture in which stress caused to separate the material. Therefore, based on the predicted mises stress of GFRP, higher Mises stress is required to rupture the GFRP under the short duration of standard fire than the longest duration of standard fire exposure.

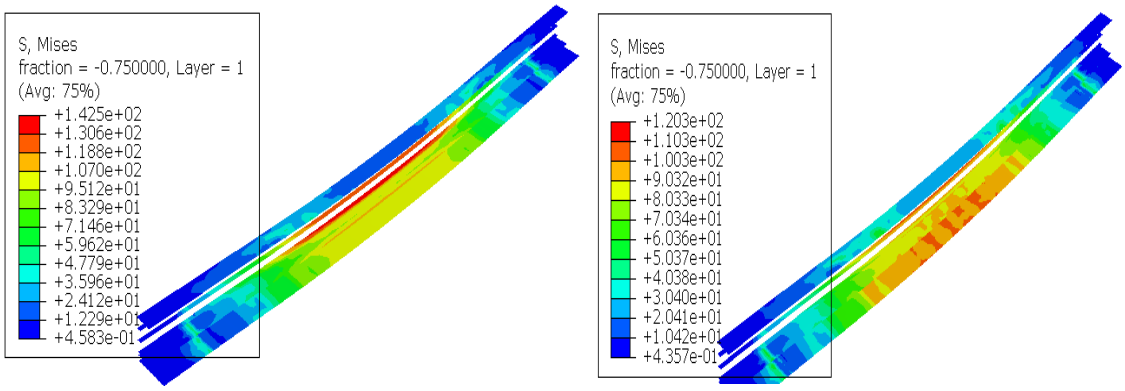

(a) One hour standard fire Mises stress (b) one-hour hydrocarbon fire Mises stress

Figure 4.22: Effect of fire types on Pultruded GFRP Mises stress

4.3.4 Effect of sustained load level on concrete deck

The sustained load level was investigated to evaluate its effect on temperature evolution, load-deformation response, damage, and crack pattern of concrete bridge deck subjected to pool fire. In the current study, two load levels were considered: 50% and 75% of the ultimate load-carrying capacity of the concrete deck at room temperature. The two-load level was subjected to the same fire duration of 2340 sec of pool fire load

in figure 3.8. The temperature evolution of concrete decks after sustained load of 50% and 75% applied at the top loading plate of the concrete deck; did not have any variation on the predicted temperature of pultruded GFRP and the concrete surface. The predicted temperature evolution of the internal temperature of pultruded GFRP at the soffit center had the same pattern as illustrated in figure 4.1. In this study, the effect of sustained load on predicted temperature evolution of concrete bridge deck did not illustrate graphically to avoid repetition. The reader may refer to figure 4.1 of this study. The effect of sustained load and deflection of the concrete deck is illustrated and compared in Figures 4.23a and b.

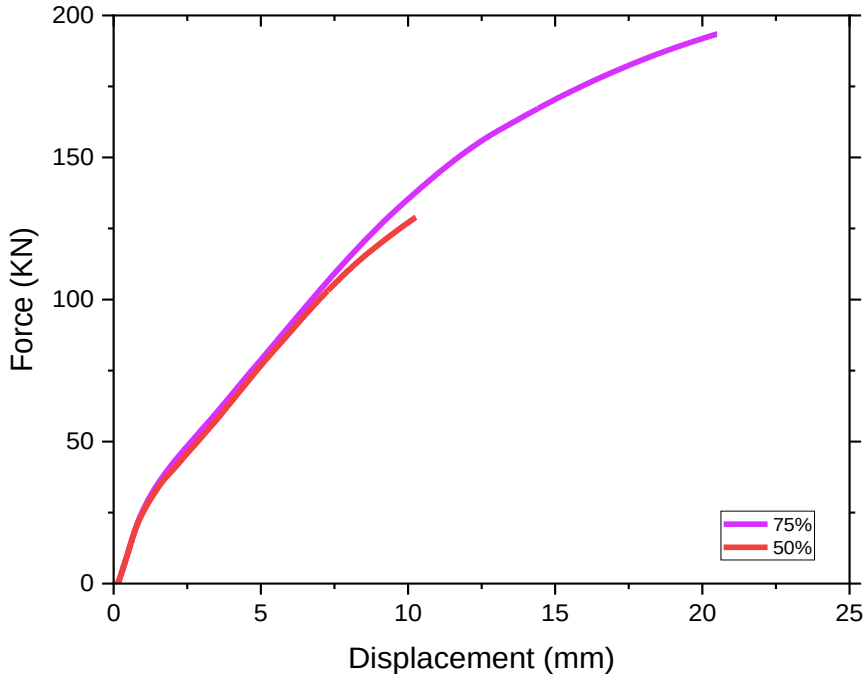

Figure 4.23: The effect of sustained load level on the load-deflection response of the concrete deck

It can be observed from figure 4.23a and b that with varying the sustained load level the deflection of the concrete deck increase with increasing the load level. As the sustained load increased from 50% to 75% the ultimate load-carrying capacity; the deflection of the deck increased from 129 to 193.5 KN and 10.3 to 20.5 mm respectively. This indicates the effect of the sustained load significantly influences the deformation of the concrete bridge deck subjected to fire. In general, the presence of sustained loading at elevated temperatures does not have a noticeable impact on the pultruded GFRP act as a bottom layer reinforcement and concrete temperature predicted. However, it leads to creep deflection.

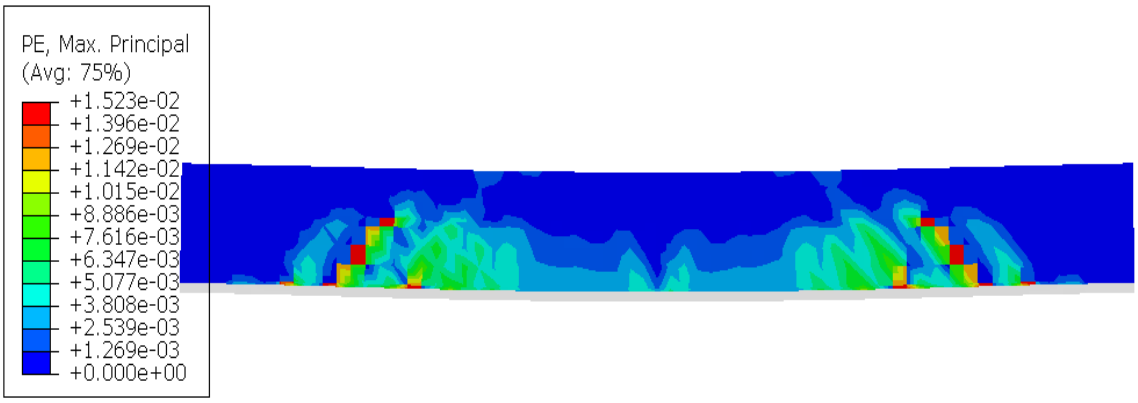

(a) Maximum principal plastic strain at 50% of sustained load

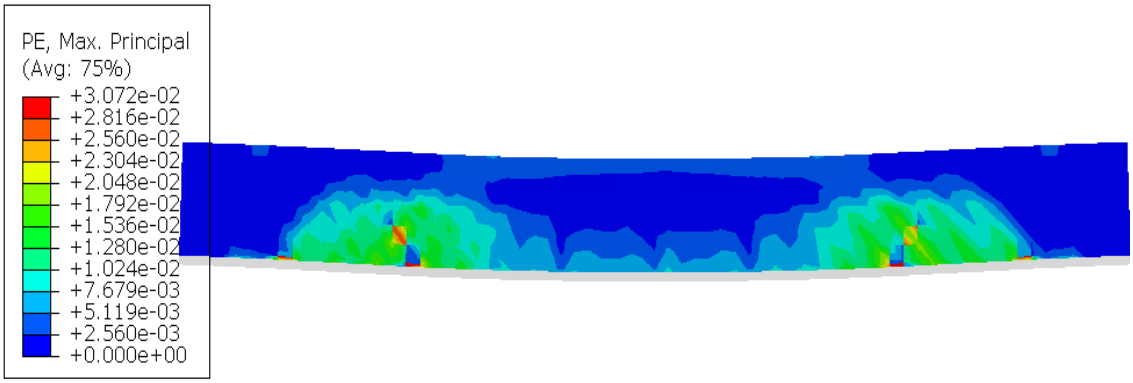

(b) Maximum principal plastic strain at 75% of sustained load

Figure 4.24: Effect of sustained load on maximum principal plastic strain and cracking of the concrete deck

The effect of sustained load on maximum principal plastic strain was illustrated in Figures 4.24a and b. The concrete bridge deck sustained with 75% of the ultimate load of undamaged deck experienced maximum plastic deformation than the 50% of the sustained load. At 50% of sustained load as illustrated in figure 4.24a, the small shear crack starts from the interface of concrete and GFRP SIP formwork concrete bridge deck, and further growth to the compression side of the deck while at 75% of sustained load around the loading points nearest to support the shear cracks more concentrated. Additionally, the flexural cracks also were developed at the tension side of the deck between two loading points. This result also indicates that the level of the sustained load has a significant effect on creep deformation, and the growth of shear and flexural cracks across the section of the deck.

Figure 4.25a and b present the effect of sustained load on tension damage of concrete bridge deck subjected to fire between two loading points. As the level of the sustained

load increase from 50 to 75 % the degree of tension damage of the deck increase. The interior concrete directly above the GFRP formwork sustained less damage as a result of an exposed fire at 50% of sustained load compared with the 75% sustained load. Furthermore, the concrete spalling due to thermal loading was more developed at the compression zone of the deck at 75% of the sustained load. This result indicates that the level of the sustained load has a notable effect on tension damage of the GFRP SIP formwork concrete bridge deck simultaneously subjected to fire and mechanical load.

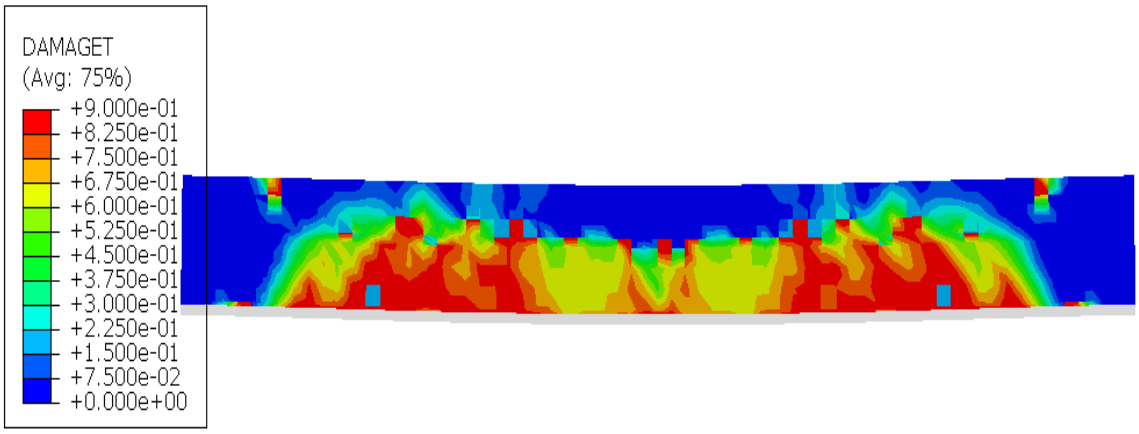

(a) Tension damage at 50% of sustained load

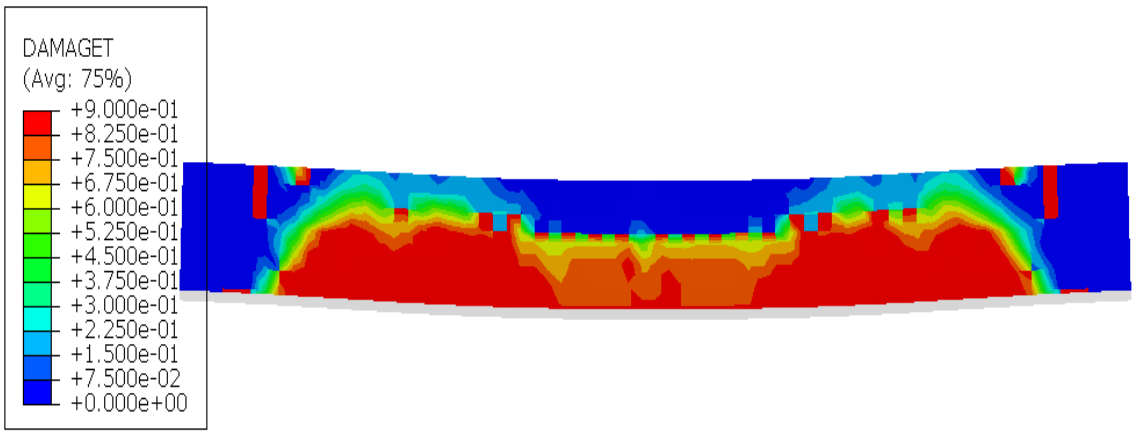

(b) Tension damage at 75% of sustained load

Figure 4.25: Effect of sustained load on tension damage of concrete bridge deck

The influence of the sustained load on predicted Mises stress of the pultruded GFRP Tup ribs was presented in Figures 4.26a and b. In both cases, the Mises stress is more concentrated at the bottom soffit of the deck rather than at the web of GFRP T-up ribs. The maximum value of the Mises stress on ribs increases from 78.58 to 135.6 N/mm^2 at 50 and 75% sustained load. This is because as the applied load increase the stress developed on the object also increase.

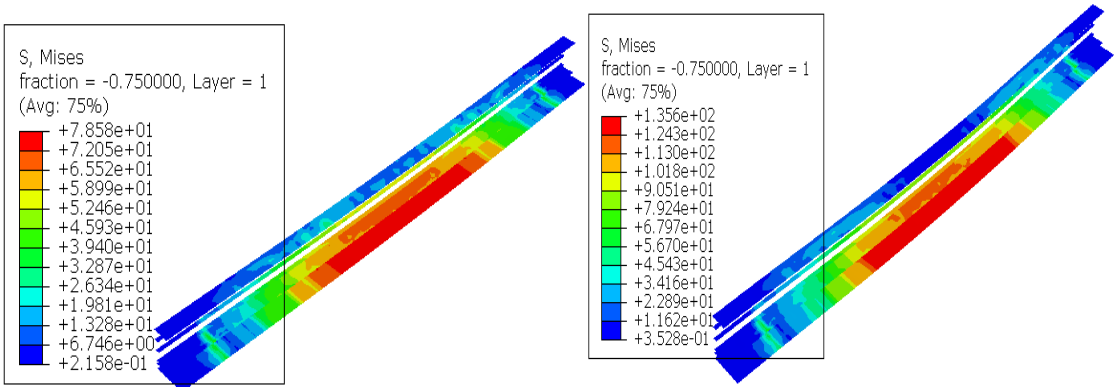

(a) Mises stress at 50% of sustained load (b) Mises stress at 75% of sustained load

Figure 4.26: Effect of sustained load on pultruded GFRP Mises stress

4.3.5 Effect of deck width on the concrete bridge deck

This parametric study was performed to investigate the size effect on temperature evaluation, the load-carrying capacity, damage, cracking, and Mises stress of the concrete bridge deck. To investigate the effect of deck width, two concrete deck sizes of 205×186×1425mm and 410×186×1425mm were investigated under fire damage state and had one and two GFRP T-up ribs along their length respectively. The reason behind varying the number of GFRP T-up ribs was to further study whether downscaling the GFRP T-up ribs had a proportional influence on the performance of the concrete bridge deck subjected to fire. Figure 4.27 illustrates the predicted temperature of internal temperature of pultruded GFRP in both cases.

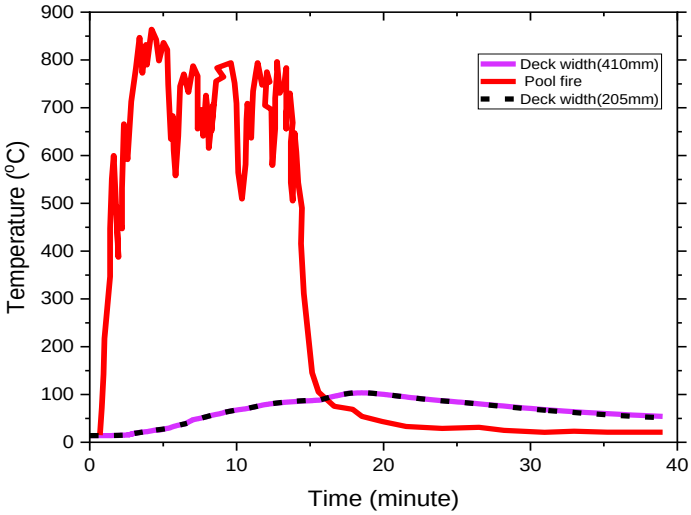

Figure 4.27: Effect of deck width on the predicted temperature

It is observed that in figure 4.27 the effect of deck width did not have a significant effect on the temperature evolution of the concrete bridge deck. The peak temperature predicted on pultruded GFRP for 205 and 410mm deck width were about 104 and 103

°C. This indicates that the deck width had a very smaller effect on the predicted temperature evolution of the concrete deck.

Figure 4.28 shows the effect of varying the concrete deck width and downscaling the pultruded GFRP stay-in-place formwork on a load-deflection response before the fire. The result indicates that the specimen with twice the width and GFRP top reinforcement area had about 52.6% ultimate carrying capacity than the deck had one GFRP T-up ribs. The increase in the ultimate carrying capacity of the deck consisting of two GFRP SIP formwork is due to concrete confinement as a result of two adjacent T-up ribs. In general, the result obtained by finite element analysis verifies that approximately the linear scaling the ultimate carrying capacity with member width.

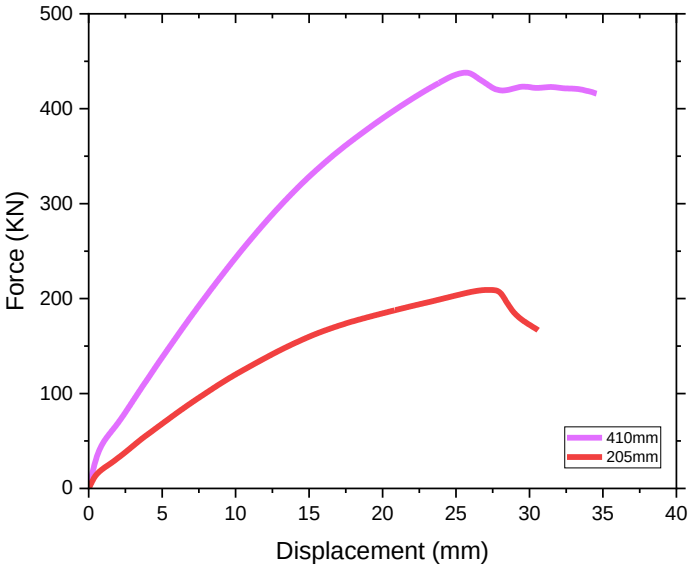

Figure 4.28: Effect of deck width on the load-deflection response of concrete bridge deck before exposed to fire

Figure 4.29 presents the effect of varying the concrete deck width and downscaling the pultruded GFRP stay-in-place formwork on the load-deflection response after the fire. The 410 mm deck width with twice the width and GFRP top reinforcement area than 205mm deck width had about 54.6% ultimate carrying capacity. Compared with the undamaged deck, the fire-damaged deck reinstates its peak load by 13.1 and 8.61% for specimens C2 and C1 respectively. The increase in the ultimate carrying capacity of the deck consisting of two GFRP SIP formwork is due to concrete confinement as a result of two adjacent T-up ribs and thermal expansion of the GFRP which result in pre-compression of concrete. In general, the result obtained by finite element analysis also

verifies an approximate linear scaling of the ultimate carrying capacity with member width of concrete bridge deck after exposure to fire.

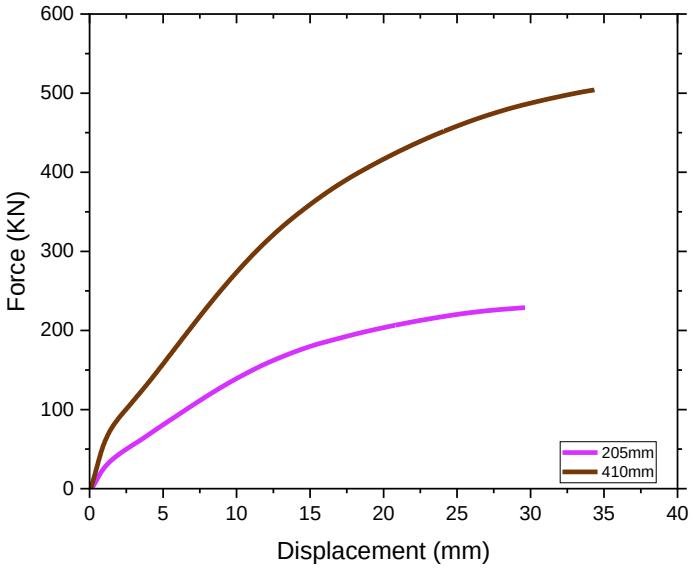

Figure 4.29: Effect of deck width on the load-deflection response of concrete bridge deck after exposed to fire

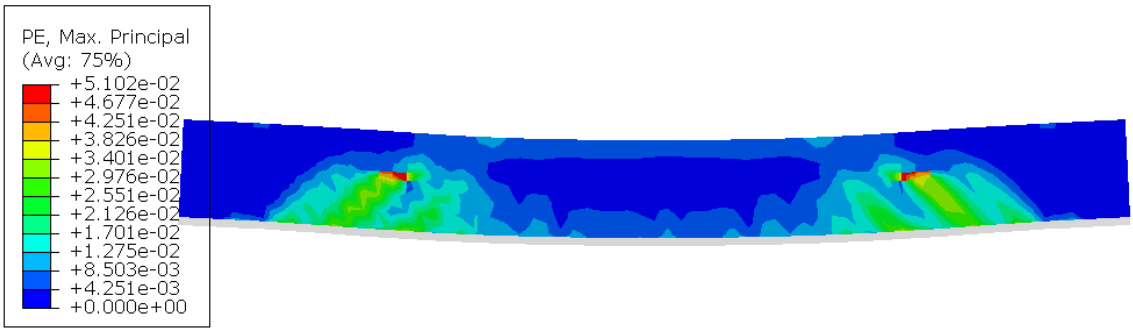

(a) Maximum principal plastic strain for 205 mm deck width

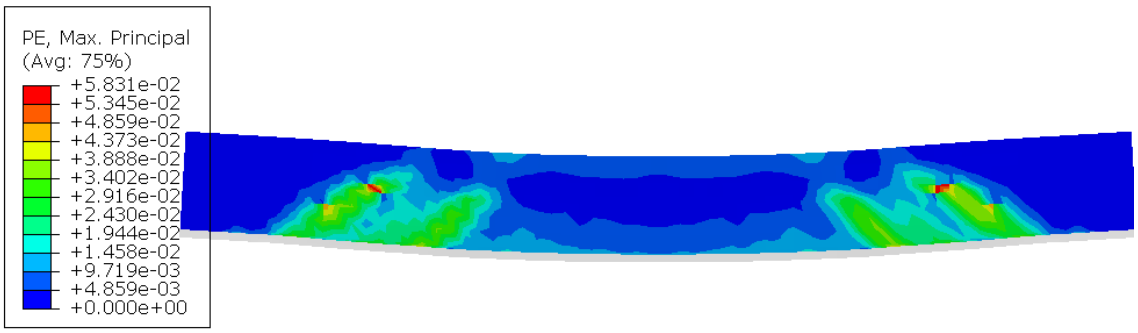

(b) Maximum principal plastic strain for 410 mm deck width

Figure 4.30: Effect of deck width on the maximum principal plastic strain and cracking failure of concrete bridge deck exposed to fire

The effect of concrete deck width on the mode of cracking failure was illustrated in 4.30a and b. Significant shear cracking was observed in specimens C1 and C2 in

regions nearest to the supporting point. Beyond the ultimate load, the shear crack further developed to the compression side of the deck. Due to the confinement of the concrete as a result of GFRP T-up rips in the case of specimen C2 the flexural crack developed at the mid-span of the deck between the loading points is improved compared with the specimen C1 where a small flexural crack observed at the mid-span area of the deck.

The contour plot of the tension damage of the concrete deck with varying deck width is illustrated in Figures 4.31a and b. In both specimens, C1 and C2 consisting of 205 and 410 mm deck width most severe tension damage was observed at the tension side of the deck nearest to the loading points. The spalling or concrete crushing due to thermal loading at the left and right side of the deck top fiber vertical extends up to the presence of the top reinforcement for specimen C1 while in the case of specimen C2 did not further extend to the tension side of the deck. This is due to the presence of twice the GFRP T-up ribs and top reinforcement area in specimen C2 enhanced the concrete confinement.

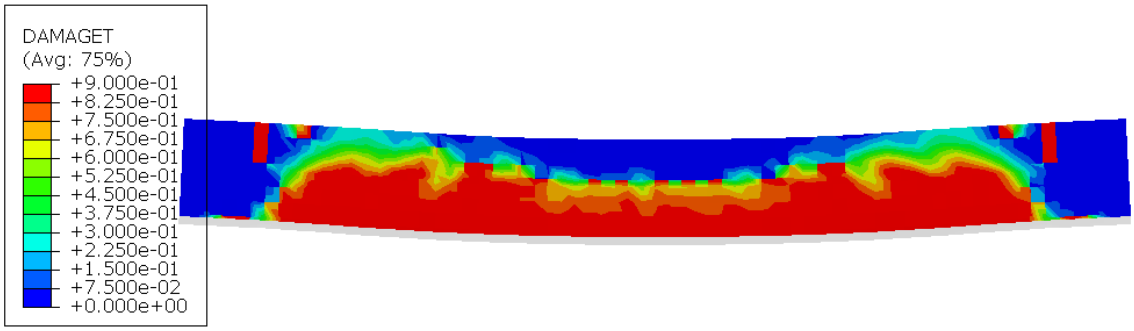

(a) Tension damage for 205 mm deck width

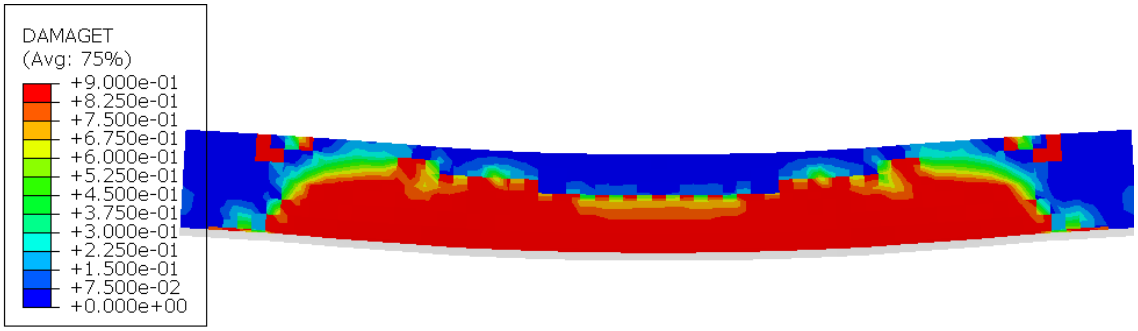

(b) Tension damage for 410 mm deck width

Figure 4.31: Effect of deck width on tension damage of concrete bridge deck exposed to fire

The effect of deck width on Mises stress of pultruded GFRP T-up ribs is presented in Figures 4.32a and b. The Mises stress was more concentrated at the interface between GFRP base plates and GFRP T-up ribs within the mid-span of the deck. This indicates that beyond the ultimate load the GFRP T-up ribs fracture at the mid-point of the concrete bridge deck. The pultruded GFRP for 205 and 410 mm deck width had the maximum Mises stress 172.7 and 211.5 N/mm^2 respectively. Therefore, the deck width has a significant effect on predicted Mises stress of pultruded GFRP.

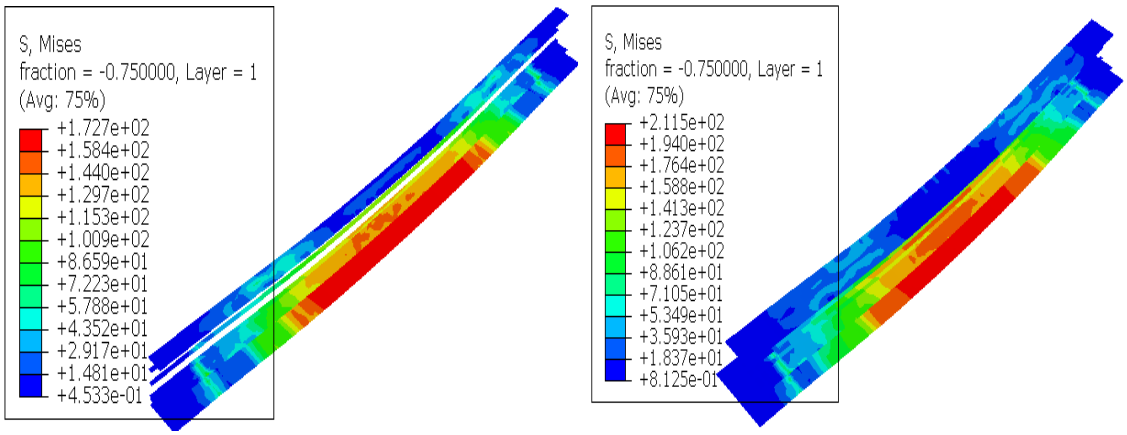

(a) Mises stress on pultruded GFRP for 205 mm deck (b) Mises stress on pultruded GFRP for 205 mm deck

Figure 4.32: Effect of deck width on Mises stress of pultruded GFRP

4.3.6 Effect of GFRP base plate length on concrete deck

This parametric study was conducted to investigate the effectiveness of strengthening the concrete bridge deck using a Glass fiber reinforced polymer base plate under room and elevated temperature. In this study, the GFRP base plate having lengths of 475 and 950 mm was used to study the effect of plate length on the performance of the concrete bridge deck. The GFRP base plate in two cases was extended from the mid-span length of the concrete deck to the two supports with their respective length. Figure 4.33 illustrates the effect of the GFRP base plate on the load-deflection response of the concrete bridge deck before being exposed to fire.

According to figure 4.33 extending the GFRP base plate to the two supports enhanced the ultimate strength of the undamaged concrete deck up to 49% compared to the control specimen SDF at room temperature. The concrete deck strengthened between the two loading points with the GFRP base plate having 14mm thickness and 450mm length reinstate the deflection of the concrete deck by 20% of the unstrengthened concrete deck and does not have any appreciable effect on the peak load of the concrete

deck. In both cases, the initiation of crack has occurred around a cracking load of 20KN and the concrete deck strengthened using GFRP base plates are stiffer than the un-strengthened deck. Further extending the GFRP base plate nearest to supports enhances the flexural response and stiffness of the concrete bridge deck at room temperature.

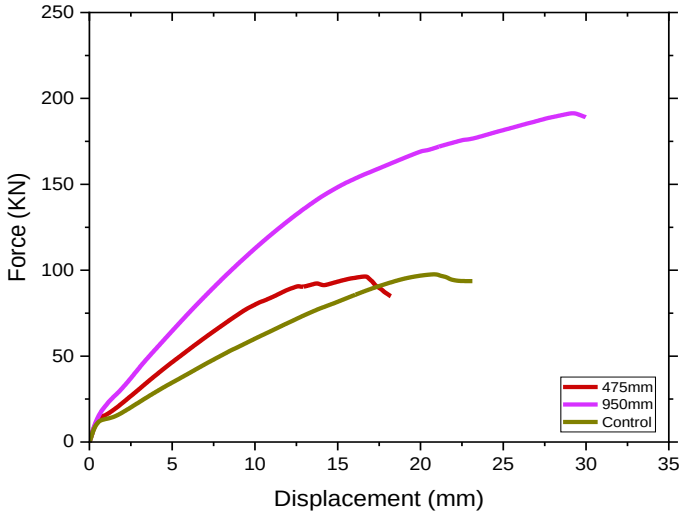

Figure 4.33: Effectiveness of GFRP base plate strengthening on the load-deflection response of concrete deck before the fire.

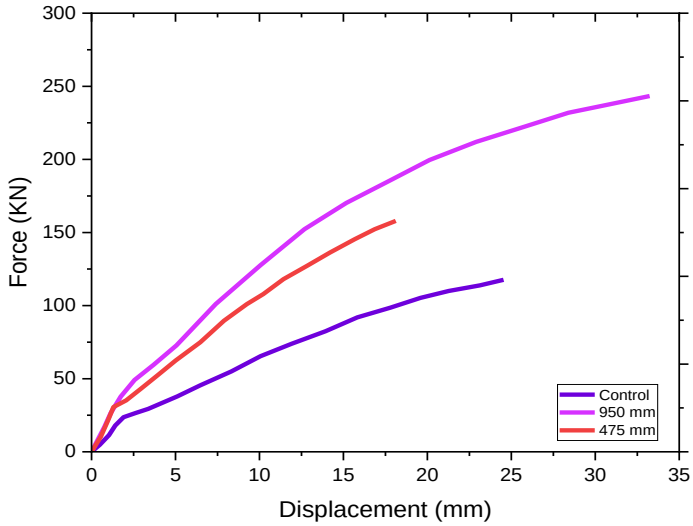

Figure 4.34: Effectiveness of GFRP base plate strengthening on the load-deflection response of concrete deck after the fire.

Figure 4.34 presents the effectiveness of GFRP base plate strengthening on the load-deflection response of the fire-damaged concrete bridge deck. Extending the GFRP base plate about 475 and 950mm length enhanced the ultimate strength of the fire-damaged concrete deck up to 10.94 and 50.6 % compared to the control specimen SDF in which full span GFRP base plate was removed. The initiation of the crack in un-strengthened fire damaged specimen C1 had a cracking load of about 25 KN while the

strengthened fire damaged specimen C1 between loading point and further extending to support the initiation of crack were occurred at around a cracking load of 28 KN. The fire-damaged strengthened concrete bridge deck is stiffer than the unstrengthened fire-damaged specimen SDF. Overall, further extending the GFRP base plate nearest to supports enhances the flexural response and stiffness of the concrete bridge deck after the fire. The level of strength enhancement for a fire-damaged concrete bridge deck subjected to the simulated fire and mechanical load was higher than an undamaged concrete deck. Beyond the cracking load of an undamaged concrete deck, the stiffness of the fire-damaged could be restored.

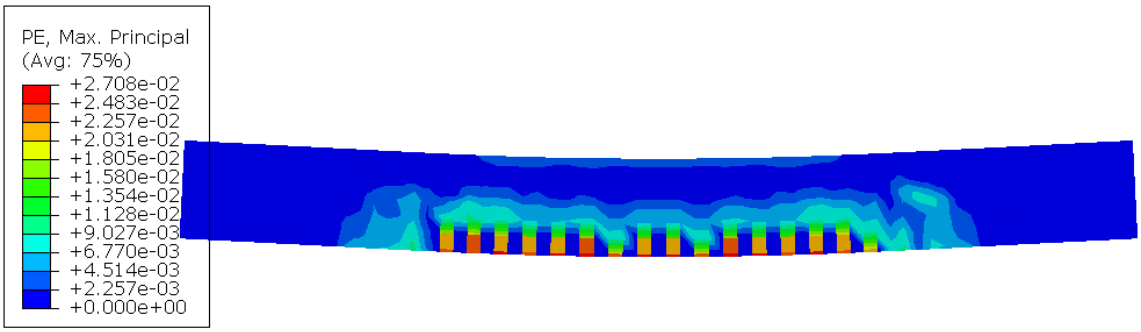

(a) Maximum principal plastic strain for control specimen SDF

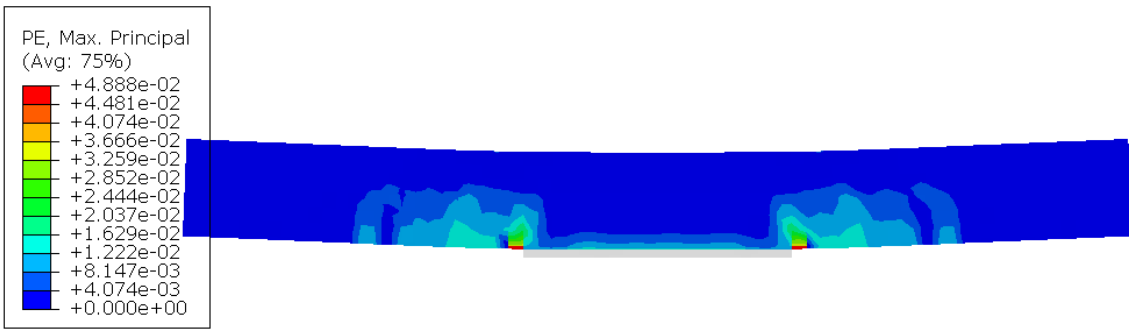

(b) Maximum principal plastic strain for 475 mm GFRP base plate length

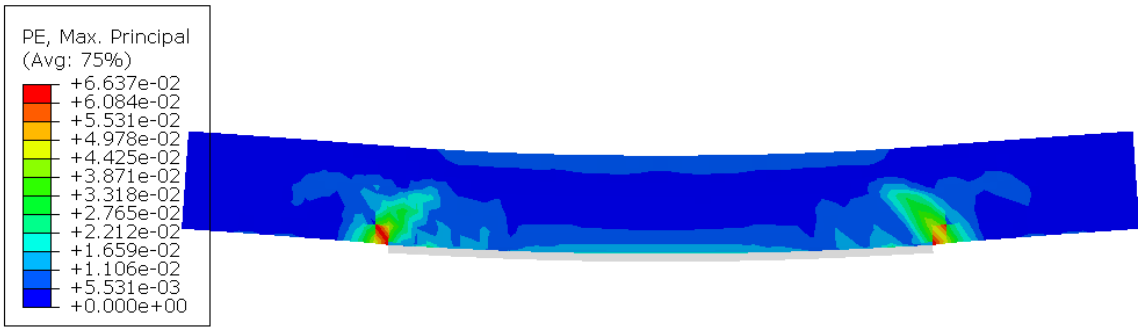

(c) Maximum principal plastic strain for 950 mm GFRP base plate length

Figure 4.35: Effectiveness of GFRP base plate strengthening on the maximum principal plastic strain and cracking failure of concrete deck subjected to fire

As observed from figure 4.35a significant flexural crack was observed in the SDF specimen in the region where full span GFRP base plate was removed. Strengthening the fire-damaged specimen SDF between the loading points with 450 mm plate length in figure 4.35b and further extending to support with 950 mm plate length in figure 4.35c improve the occurrence of the flexural crack between the loading points. However, the shear crack was observed at the interface of the end length of the GFRP base plate and concrete due to the weak composite action between the concrete and GFRP base plate. Therefore, strengthening the flexural area of the fire-damaged concrete deck using the GFRP base plate is effective to improve the cracking failure of the concrete decks.

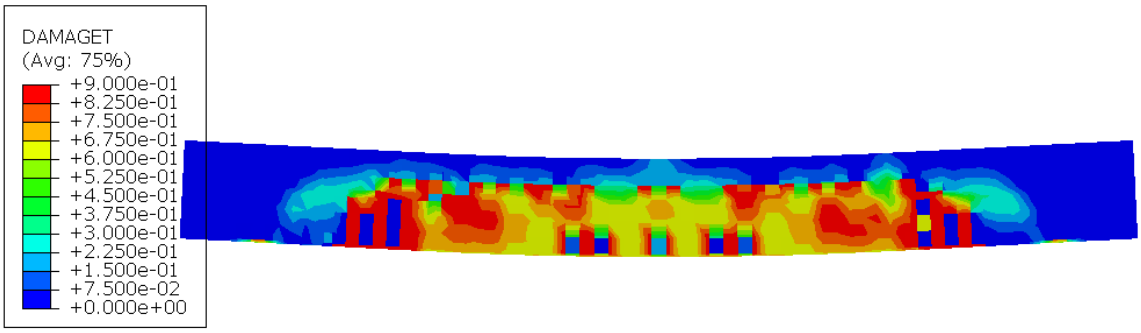

(a) Tension damage for control specimen SDF

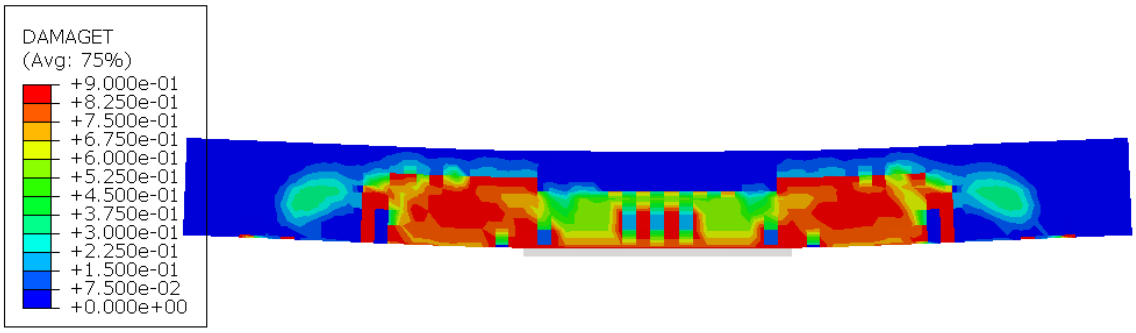

(b) Tension damage for 475 mm GFRP base plate length

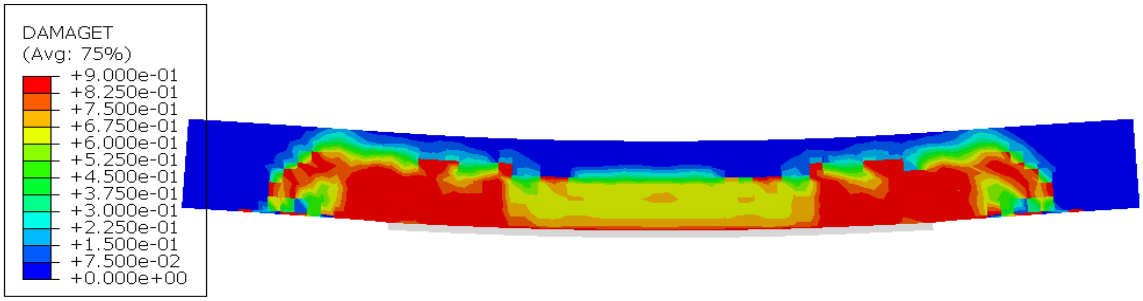

(c) Tension damage for 950 mm GFRP base plate length

Figure 4.36: Effectiveness of GFRP base plate strengthening on tension damage of concrete deck subjected to fire

The tension damage of the concrete bridge deck subjected to fire was occurred at the tension side in all fire damage concrete specimen SDF with and without GFRP base plate strengthened. But, the degree of the tension damage in all specimens shows different damage contour plots. As observed from figure 4.36a, removing the GFRP base plate from the full span length of the concrete deck, concrete tension damage between the loading points was extended up to the presence of the top reinforcement. For the fire-damaged strengthened concrete deck, similar to the unstrengthened fire damage the tension damage of the concrete occurred at the tension fiber of the concrete deck subjected to pure bending. The difference in tension damage of the strengthened and unstrengthened fire-damaged concrete deck is the strengthened fire damage using the 450 and 950 mm GFRP base plate length improves the damage of the concrete between the loading points above the GFRP T-up ribs as illustrated in figure 4.3b and 3 respectively. As the applied load increased in the specimen, SDF strengthened using a 950 mm GFRP base plate; the tension damage of the concrete becomes more concentrated around the loading points. As a result, its necessary to strengthen the fire-damaged concrete bridge deck using a GFRP base plate to improve the tension damage further extending to the compression zone.

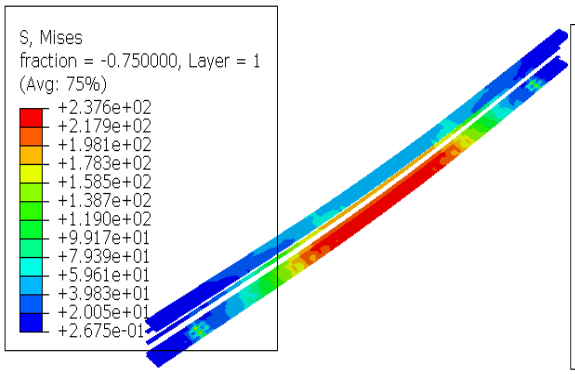

(a) Mises stress for full span GFRP base plate removed

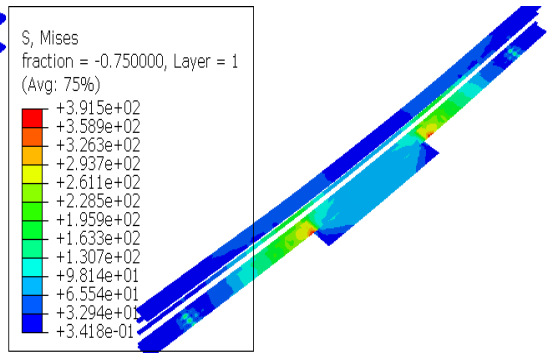

(b) Mises stress for 475 mm GFRP base plate length

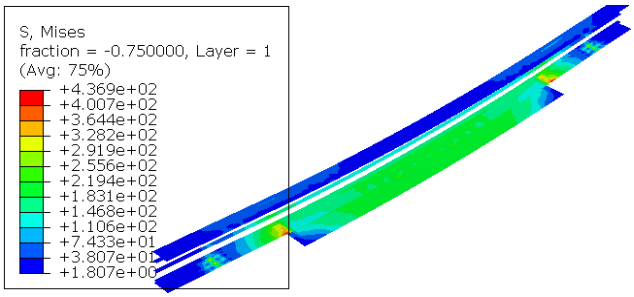

(b) Mises stress for 475 mm GFRP base plate length

Figure 4.37: Effectiveness of GFRP base plate strengthening on GFRP Mises stress

Figure 4.37a, b, and c present the effect of GFRP base plate length on Mises stress developed on pultruded GFRP. The Mises stress on pultruded GFRP of unstrengthened fire damaged specimen SDF in which full span GFRP base plate removed more concentrated at mid-span while for fire-damaged strengthened the concentration of the Mises stress observed at interface of the end length of the GFRP base plate and GFRP T-up ribs. This result indicates beyond the ultimate load of the concrete deck, for unstrengthened fire-damaged concrete deck, the fracture of the GFRP T-up ribs occurs at the midpoint while for the strengthened fire-damaged concrete deck it occurs at the interface of the GFRP base plate and GFRP T-up ribs. The maximum predicted Mises stress on pultruded GFRP for unstrengthened and strengthened fire-damaged concrete deck using 475, and 950 mm GFRP base plate length had 237.6, 391.5, and 436.9 N/mm^2 respectively.

4.3.7 Effect of GFRP base plate thickness on concrete deck

This parametric study was conducted to study the effect of GFRP base plate thickness on predicted temperature, load-deflection response, damage, Mises stress, and crack pattern of concrete bridge deck subjected to fire. Two GFRP base plates having 10 and 20 mm thickness were selected in this study based on the use of the fire resistance benefits associated with thermal thickness and select a GFRP structural form that was representative of a full-scale bridge deck in practice(M. Nelson & Fam, 2013). The effect of the GFRP base plate thickness on predicted temperature is illustrated in figure 4.38.

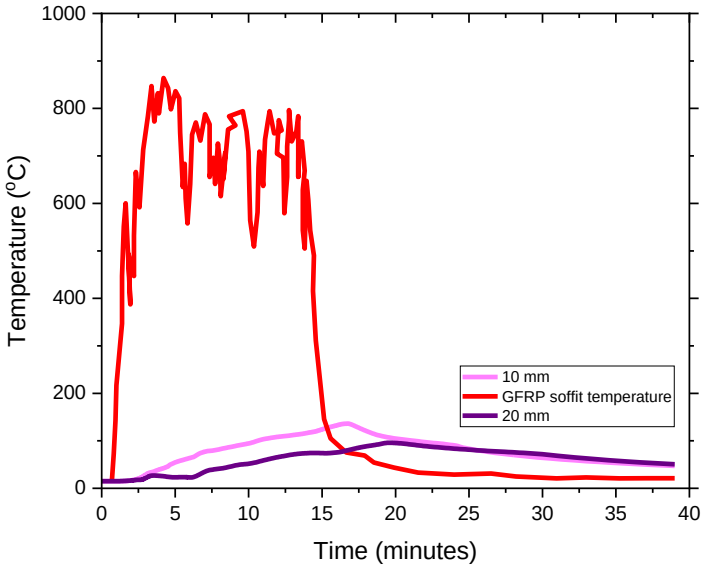

Figure 4.38: Effect of GFRP base plate thickness on the predicted temperature of the concrete deck

It can be observed in Figure 4.38 the GFRP base plate thickness significantly influences the predicted temperature of pultruded GFRP with a peak temperature of about 136 and 95 °C for 10 and 20 mm GFRP base plate thickness respectively. During the first heating rate of 150 seconds and the cooling phase, the GFRP base thickness did not influence the predicted temperature of the concrete bridge deck subjected to fire. This result indicates that the thickness of the GFRP base plate must be in consideration to improve the thermal load during a high heating rate than the cooling stage due to fire on the concrete bridge deck.

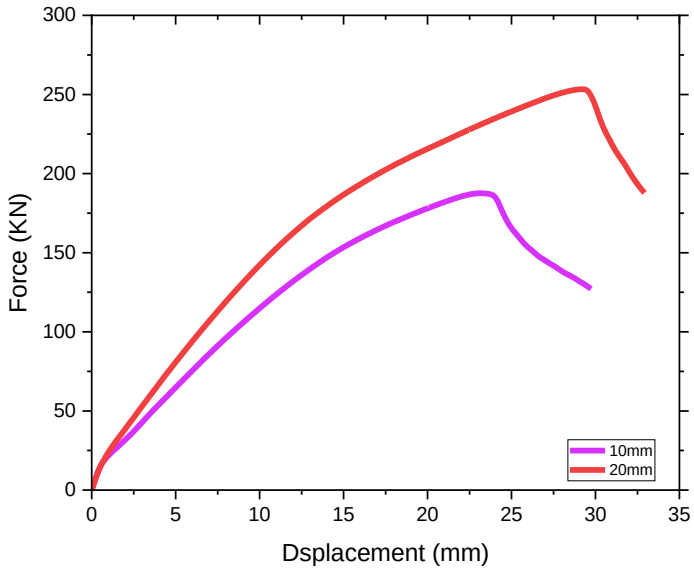

Figure 4.39: Effect of GFRP base plate thickness on the load-deflection response of concrete bridge deck before the fire

Figure 4.39 presents the load-deflection relationship of undamaged concrete bridge deck with control specimen C1 which has a 14mm thick GFRP base plate replaced with 10 and 20 mm thickness for further investigation on the ultimate carrying capacity of the concrete bridge deck before the fire. It can be observed from figure 4.39 that with different GFRP base thicknesses the failure mode of the concrete bridge is the same. However, increased GFRP base plate thickness enhances the ultimate load-carrying capacity of the concrete bridge deck. The ultimate load of the undamaged fire concrete bridge deck with 20mm GFRP base plate had 25.95% more than 10mm GFRP base plate thickness. The GFRP base thickness increases the stiffness of the undamaged concrete bridge deck and cannot influence the initiation of crack which occurred in both cases at a cracking load of about 25 KN. Therefore, the GFRP base plate thickness has a significant effect on ultimate load carrying capacity and the stiffness of concrete bridge decks before the fire.

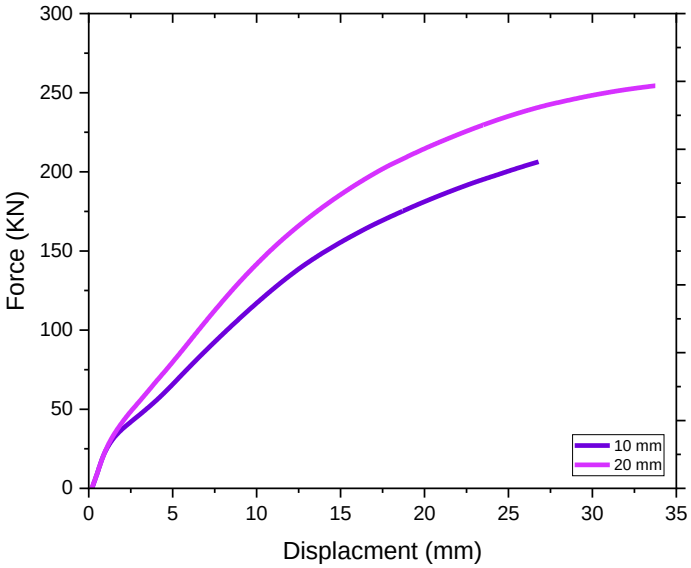

Figure 4.40: Effect of GFRP base plate thickness on the load-deflection response of concrete bridge deck after fire

It can be seen from figure 4.40 that with different GFRP base thickness the deflection mode of the fire-damaged concrete bridge deck behaves the same pattern. But, with increased GFRP base thickness; the peak load of the concrete bridge deck subjected to fire was enhanced. The ultimate load of the concrete bridge deck exposed to fire with 10 and 20mm GFRP base plate thickness experienced more ultimate load than the control concrete decks which are investigated without exposure to fire at room temperature. The enhanced ultimate load of the fire-damaged concrete bridge deck is about 9.09 and 14.65 % of the reference concrete deck with 10 and 20 mm GFRP base plate thickness respectively. After exposed to fire the GFRP base thickness also reinstates the occurrence of the initiation cracking of fire-damaged concrete deck from cracking load of about 25 to 30 KN. This is due to the thermal heating and cooling of the concrete bridge deck resulting in the pre-compression of concrete. Because of this, it is effective to increase the thickness of the GFRP base plate of concrete bridge deck.

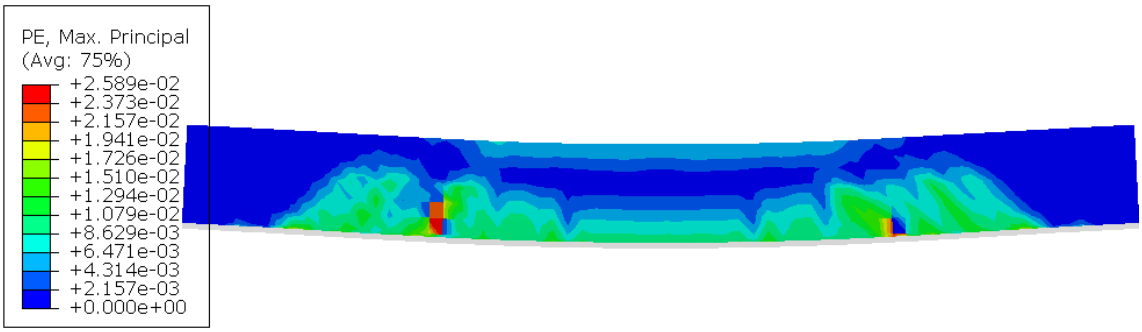

(a) Maximum principal plastic strain for 10 mm GFRP base plate thickness

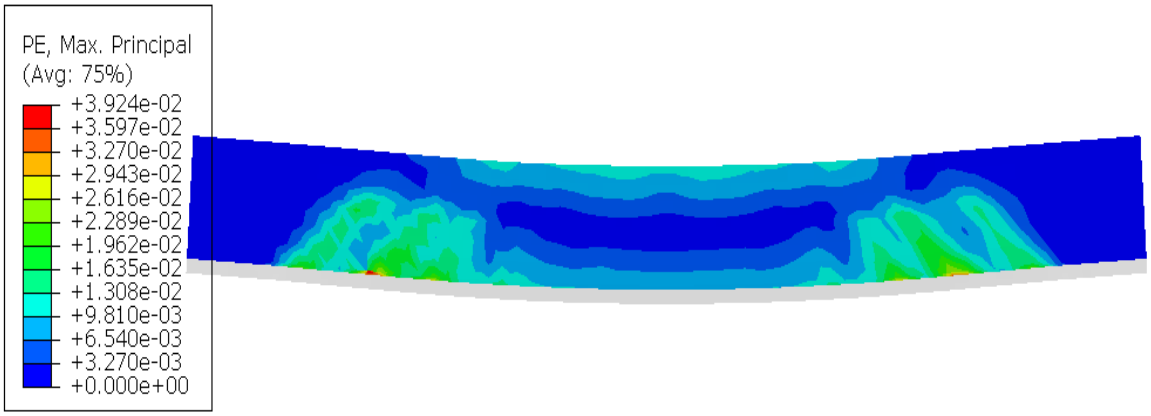

(b) Maximum principal plastic strain for 20 mm GFRP base plate thickness

Figure 4.41: Effect of GFRP base plate thickness on the maximum principal plastic strain and cracking failure pattern of concrete bridge deck after fire

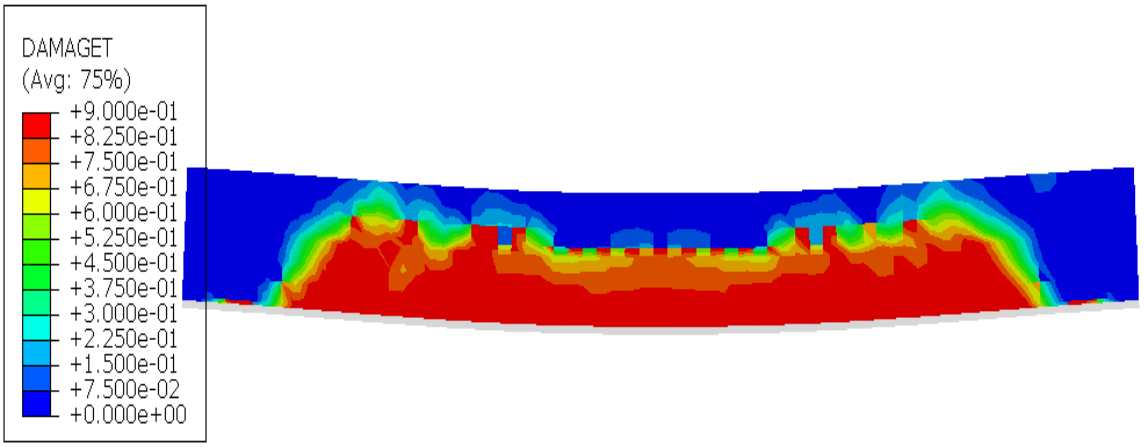

(a) Tension damage for 10 mm GFRP base plate thickness

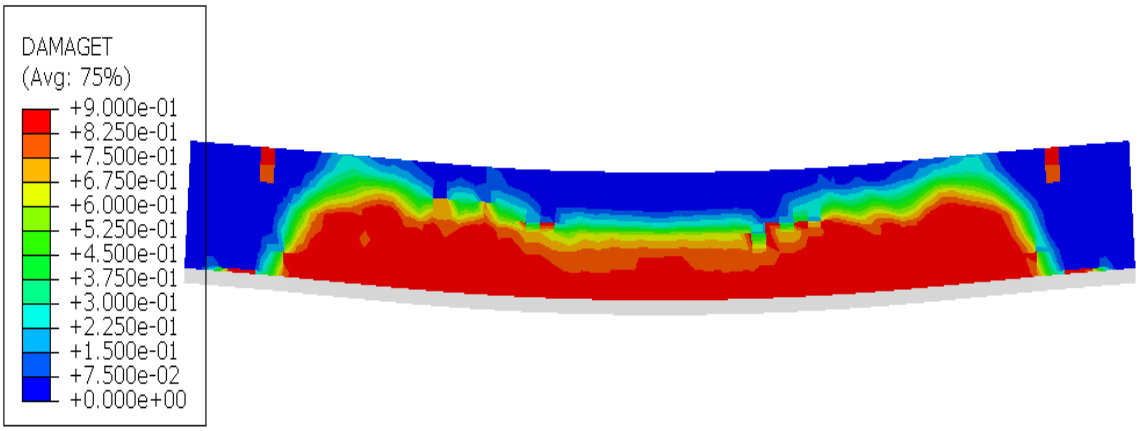

(b) Tension damage for 20 mm GFRP base plate thickness

Figure 4.42: Effect of GFRP base plate thickness on the maximum principal plastic strain and cracking failure pattern of concrete bridge deck after fire

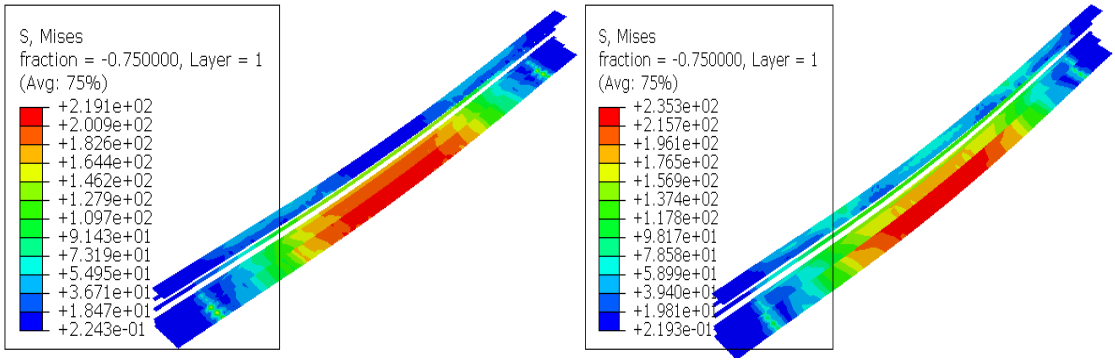

(a) Mises stress on 10 mm GFRP base thickness (b) Mises stress on 20 mm GFRP base thickness

Figure 4.43: Effect of GFRP base plate thickness on Mises stress of pultruded GFRP

4.3.8 Effect of span to depth ration

The effect of span to depth ratio on the performance of concrete bridge deck at room temperature and subjected to fire were examined. This was performed by varying the length and the depth of the concrete bridge deck with uniform deck width. Four concrete decks were used in this study with dimensional specimen detail given in table 4.2. The load-deflection response of the concrete deck is presented and compared in figures 4.44 to 4.49. Table 4.2 summarize the flexural properties of the concrete bridge deck of the undamaged and fire damage concrete decks, including peak load *(P_{max})* and displacement at maximum load(Δ_{max}).

Table 4. 2: Span to depth ratio used in the current study

Concrete deck size(mm)	Span to depth (-)	Maximum ultimate load (KN)		Maximum deflection(mm)	
		Room temperature	Elevated temperature	Room Temperature	Elevated temperature
1425×205×186	7	209.14	228.85	27.23	29.62
1425×205×172	8	97.6	117.64	20.82	24.6
1302×205×186	7	233.52	282.36	24	27.8
1488×205*186	8	198.61	240.97	29.52	34.2

Note: Concrete deck dimensions are given in c/c span × width × depth format

Figures 4.44 and 4.45 present's effect of span to depth ratio on the load-deflection relationship of undamaged concrete bridge deck before the fire with varying concrete deck depth and length respectively. It can be observed from figure 4.44 that with increasing span to depth ratio of the concrete deck from 7 to 8 varying the depth of deck; the ultimate load-carrying capacity significantly reduced by 53.3% while varying the length of the deck relatively influence the performance of the deck; that is reduced only by 14.95%. Therefore, the result indicates that it's the effect of span to depth ratio varying with a depth significantly influence the performance of concrete deck under normal condition.

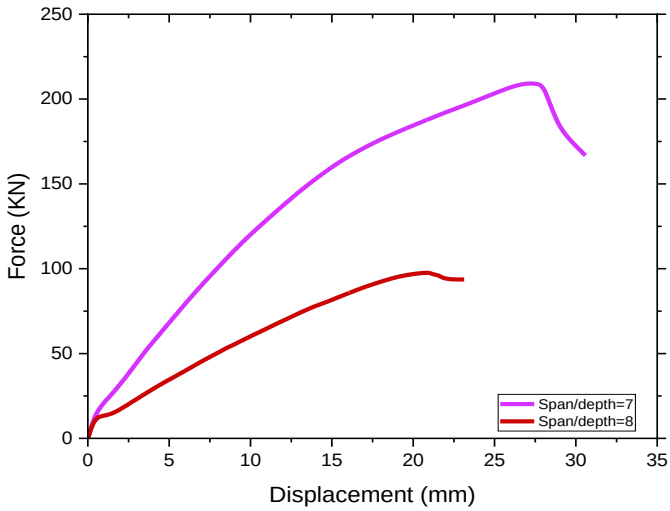

Figure 4.44: Effect of span to depth ratio on load deflection response of concrete deck varying deck depth before the fire

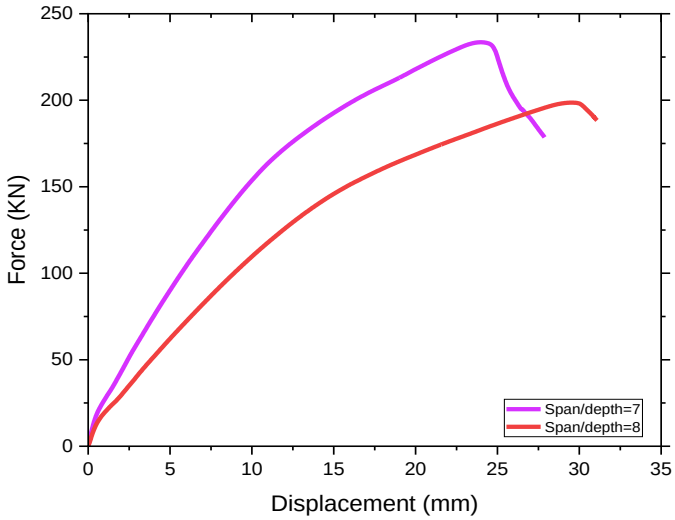

Figure 4.45: Effect of span to depth ratio on the load-deflection response of concrete deck varying deck length before the fire

Figure 4.46 and 4.47 illustrates the effect of span to depth ratio on the load-deflection relationship of fire-damaged concrete bridge decks with varying concrete deck depth and length respectively. It can be seen from figure 4.46 that with increasing span to depth ratio of the concrete deck from 7 to 8 varying the depth of deck; the ultimate load-carrying capacity of a fire-damaged concrete deck significantly reduced by 48.6% while varying the length of the deck relatively influence the performance of the fire-damaged deck; that is reduced only by 14.66%. Therefore, the finding also indicates that it's the effect of span to depth ratio varying with a depth significantly influences the performance of fire-damaged concrete deck subjected to fire.

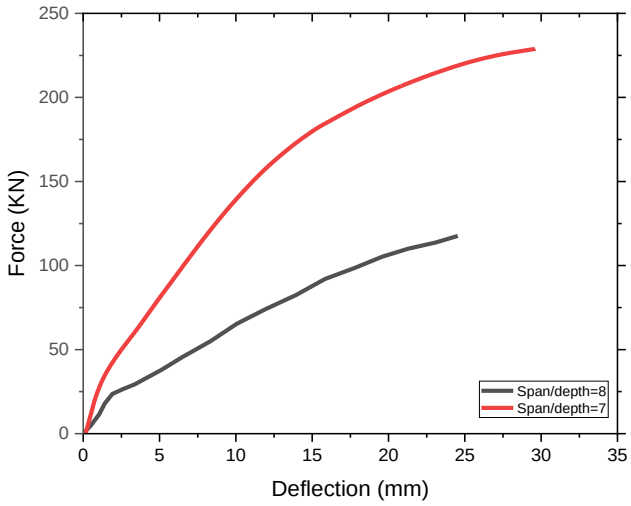

Figure 4.46: Effect of span to depth ratio on the load-deflection response of concrete deck varying deck depth after fire

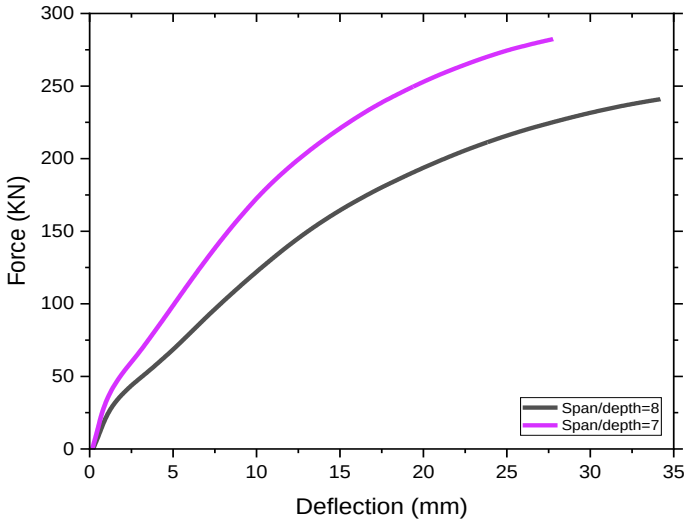

Figure 4.47: Effect of span to depth ratio on the load-deflection response of concrete deck with varying length

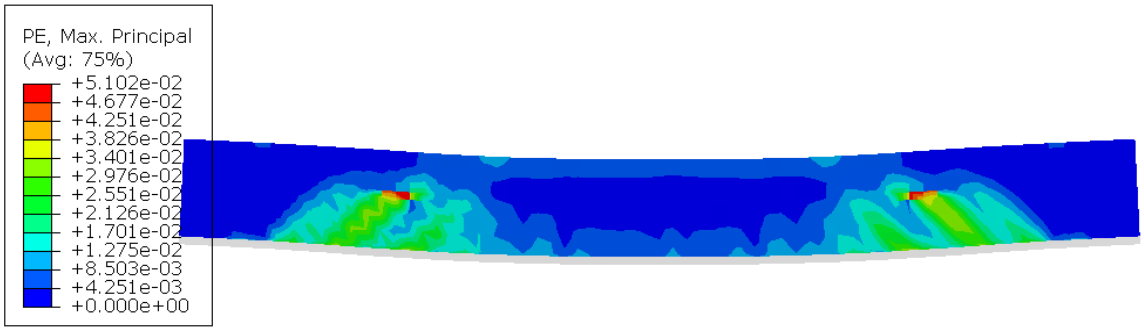

(a) Maximum principal plastic strain for span/depth = 7

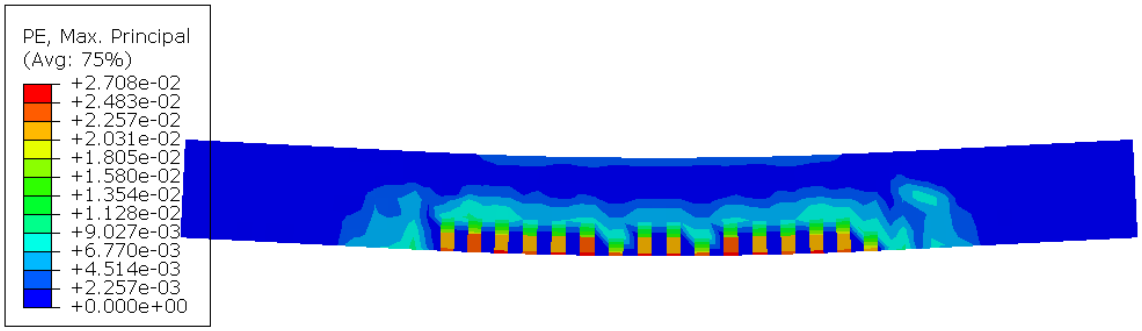

(b) Maximum principal plastic strain for span/depth = 8

Figure 4.48: Effect of span to depth ratio on the maximum principal plastic strain and cracking failure pattern of concrete bridge deck with varying depth after fire

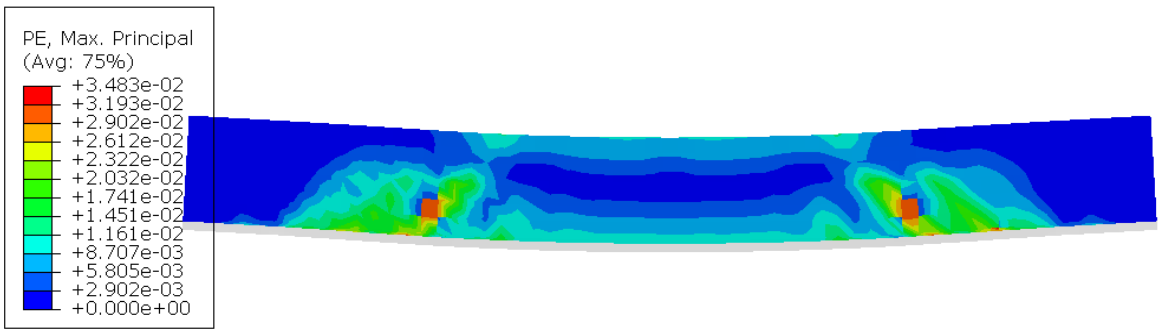

(a) Maximum principal plastic strain for span/depth = 7

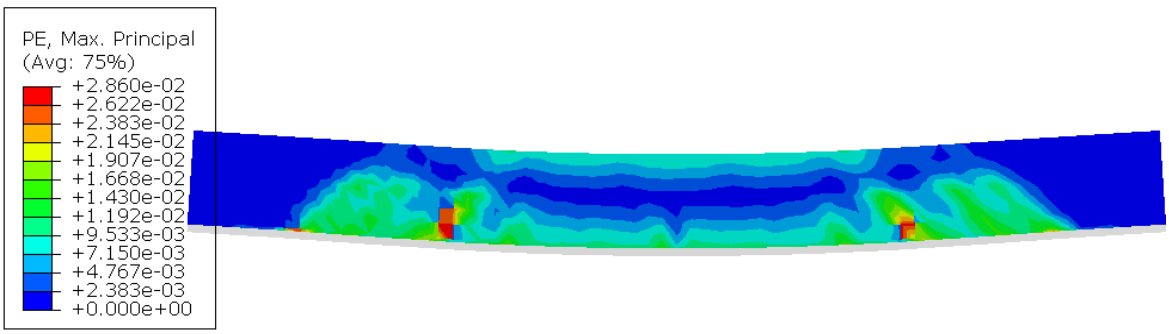

(b) Maximum principal plastic strain for span/depth = 8

Figure 4.49: Effect of span to depth ratio on the maximum principal plastic strain and cracking failure pattern of concrete bridge deck with varying length after fire

The effect of span to depth ratio on the maximum principal plastic strain and cracking failure pattern of concrete bridge deck with varying depth and length after the fire were presented in Figures 4.48 and 4.49 respectively. As observed from figure 4.48 b significant flexural crack was observed in the fire-damaged concrete deck with a span to depth ratio equal to 8 in which the full span GFRP base plate was removed. However, a significant shear crack was observed at the interface of the GFRP base plate and concrete on the rest of the fire-damaged concrete deck varying deck width and length. Therefore, increasing the span to depth ratio with varying depth have a significant effect on the cracking pattern of the concrete under fire condition.

4.3.9 Effect of heating and cooling phase

This parametric study was considered to investigate the effect of sustained load under simultaneously heating and cooling phases of the concrete bridge deck. In this study, one hour heating and cooling phase of standard fire with 100% of the sustained loads were considered. Figure 4.50 illustrates the predicted temperature of the concrete deck.

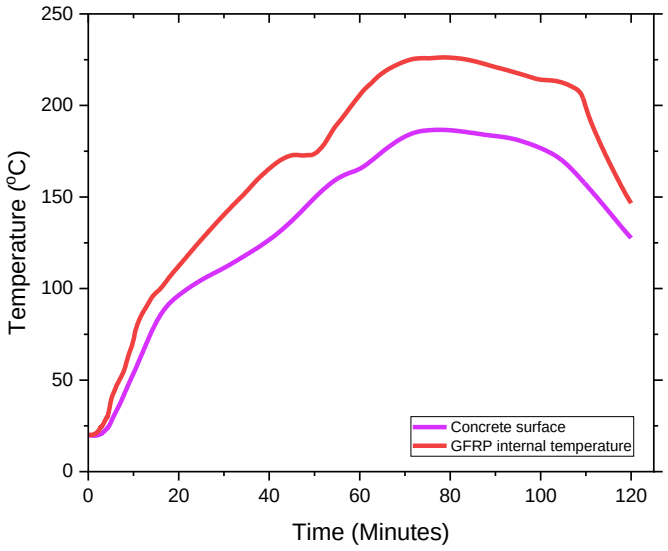

Figure 4.50: The predicted temperature at 1hour heating and cooling of standard fire

It can be observed from Figures 4.50a the heating and cooling phase significantly influences the predicted temperature of pultruded GFRP and concrete with a peak temperature of about 226 and 187 °C respectively exposing the fire for 1-hour heating and cooling phase according to standard fire (ISO 834) compared with the predicted temperature of 2-hour standard fire without cooling phase (see figure 4.13b). Above 60 minutes

of fire exposure, the temperature starts to decrease, unlike the standard fire without cooling phase linear increase.

Figure 4.51 presents the effect of the heating and cooling phase on the deflection mode of the fire-damaged concrete bridge deck. The ultimate load of the concrete bridge deck exposed to fire for 1-hour heating and cooling phase experienced more ultimate load than the concrete decks which are investigated without cooling phase of 2-hour standard fire. The enhanced ultimate load of the fire-damaged concrete bridge deck is about 3.56 and 21 % of the undamaged concrete deck and 2-hour fire-damaged concrete deck without cooling phase respectively. This is due to the thermal heating and cooling of the concrete bridge deck resulting in the pre-compression of concrete.

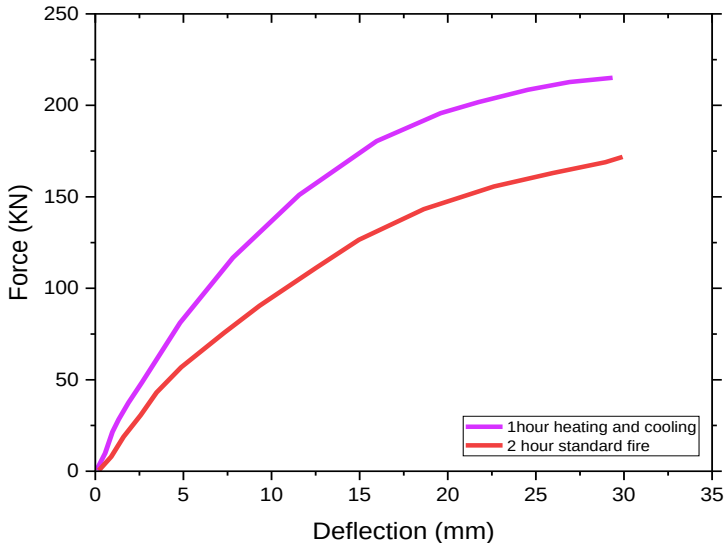

Figure 4.51: Effect of heating and cooling phase on the load-deflection response of the concrete deck

The cracking pattern was observed at the interface between pultruded GFRP and concrete in both concrete decks subjected to 1-hour heating and cooling phase, and 2-hour standard fire as presented in figure 4.52a and b. However, on the concrete deck subjected to 1hour heating and cooling phase, the flexural crack observed at the mid-span of the deck improved due to the heating and cooling of the concrete.

The tensile damage contours are illustrated in Figures 4.53a and b for 1hour heating and cooling phase, and 2-hour standard fire without cooling phase. In both cases, the tensile damage was initiated at extreme tension fiber of the concrete deck in zones subjected to pure bending. There was a wider spread of tensile damage around the loading point and shear span supports in the case of the concrete deck subjected to a 2-hour standard fire without a cooling phase. The tensile damage of the concrete deck was

more concentrated under the loading points in both cases. It's observed that at the top of concrete around supporting points there is more crushing of concrete occurred on concrete deck subjected to fire with cooling phase. This is due to the heating and cooling of the concrete resulting in spalling of the concrete under thermal loading.

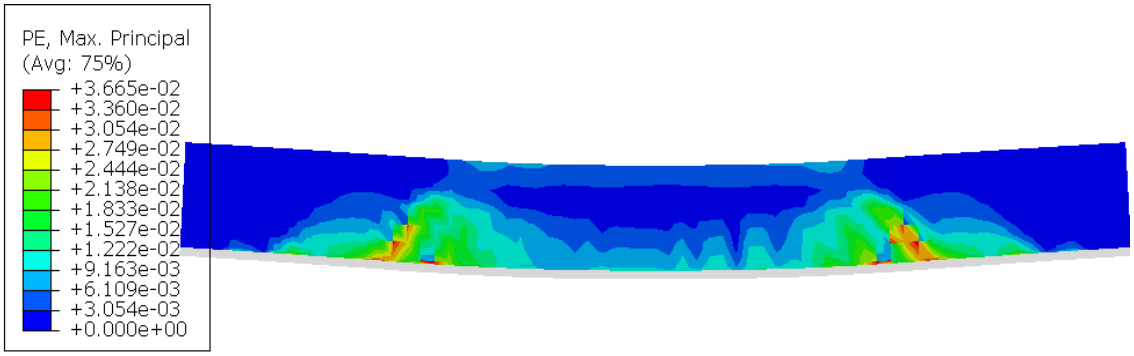

(a) Maximum principal plastic strain at 120 minutes of standard fire without cooling phase

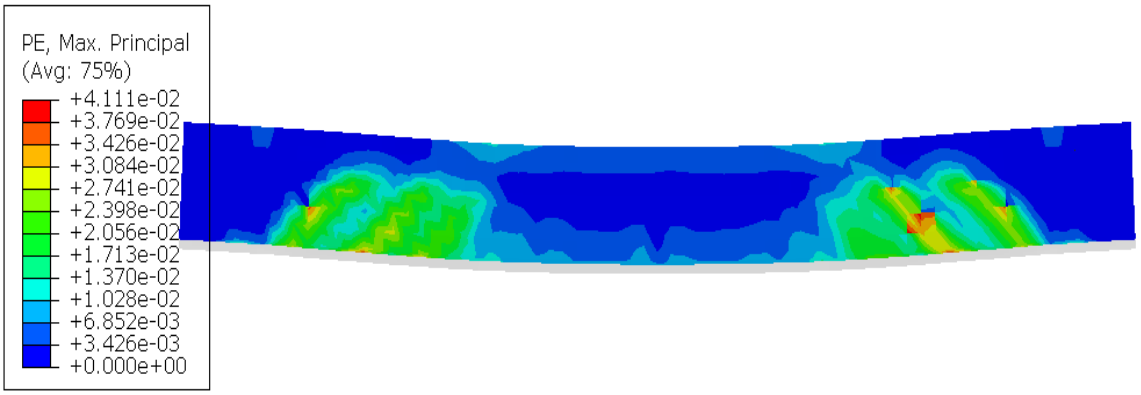

(c) Maximum principal plastic strain at 1hour heating and cooling of standard fire

Figure 4.52: Effect of heating and cooling phase on the maximum principal plastic strain and cracking failure pattern of concrete bridge deck after fire

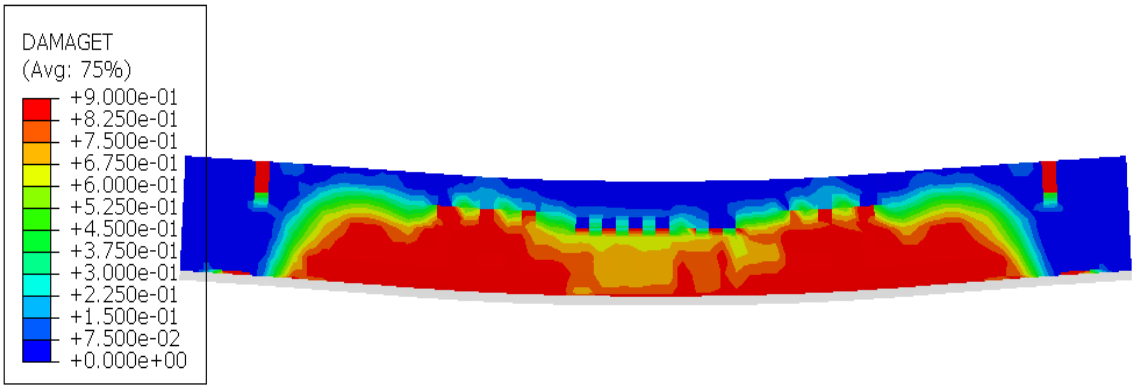

(a) Tension damage at 120 minutes of standard fire with no cooling phase

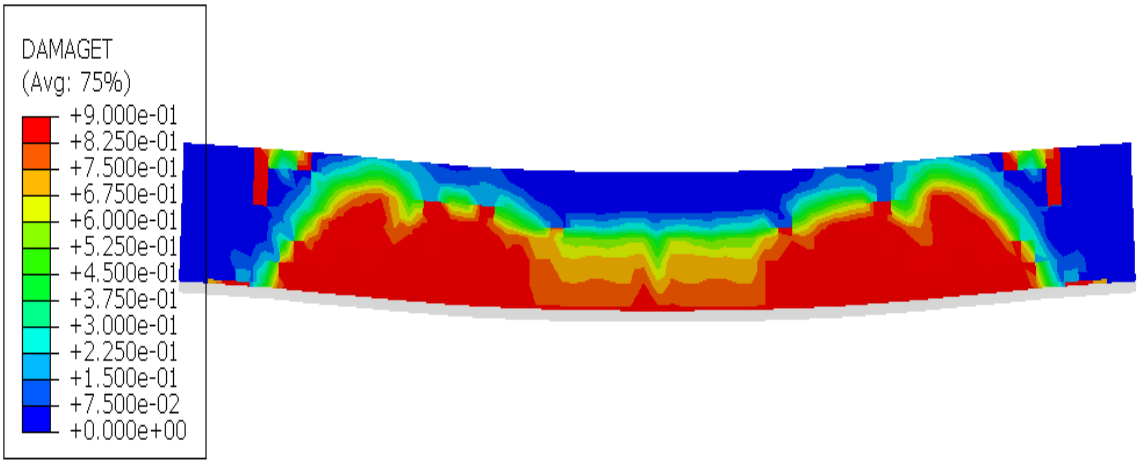

(b) Tension damage at 1 hour heating and cooling of standard fire

Figure 4.53: Effect of heating and cooling phase on tension damage of concrete bridge deck after fire

The effect of the heating and cooling phase on the Mises stress distribution of pultruded GFRP is illustrated in Figures 4.54a and b for 1hour heating and cooling phase, and 2 hour heating without cooling phase. As illustrated on the contour plot; the concrete bridge deck is subjected to fire for 1-hour heating and cooling of standard fire experienced more the Mises stress on pultruded GFRP. This is due to the thermal expansion of the GFRP under the heating and cooling phase resulting in pre-compression of the concrete. The peak Mises stress obtained on the GFRP base plate is 171.3 N/mm^2.

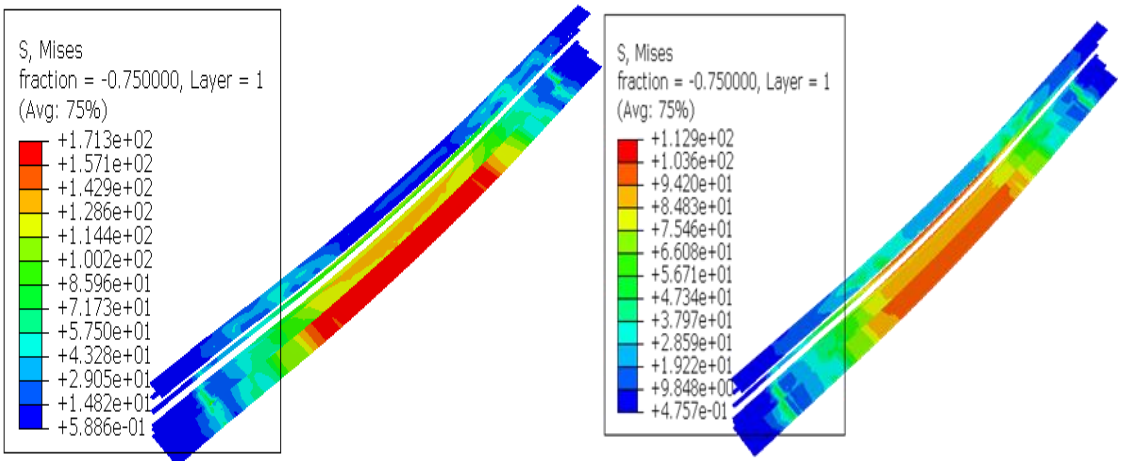

(a) Mises stress on GFRP with cooling phase (b) Mises stress on GFRP without cooling phase

Figure 4.54: Effect of heating and cooling phase on Mises stress of concrete bridge deck after fire

CHAPTER FIVE
CONCLUSIONS AND RECOMMENDATIONS

5.1 General

In the current study, the post-fire performance of the concrete bridge deck has been investigated through numerical finite element modeling using commercially available software ABAQUS (Version.2020). An extensive parametric study has been conducted to investigate the effect of aggregates types, fire duration, fire types, sustained load, deck width, GFRP plate length, GFRP plate thickness, and span to depth ratio on post-fire performance of concrete bridge deck subjected to fire. The response of the concrete bridge deck under fire such as time-temperature evolution, load-deflection response, tensile damage, cracking pattern, and Mises stress is predicted and discussed. Finally, based on the finding indicates the conclusions and recommendations are drawn.

5.2 Conclusions

This study has suggested and validated the numerical model to simulate the post-fire performance of GFRP SIP formwork for concrete bridge deck subjected to the fire using the non-linear finite element software ABAQUS standard. A further parametric study was conducted on the validated numerical model to investigate the influence of very essential parameters on the performance and failure of concrete bridge decks at elevated temperatures. For the geometrical and material properties of concrete bridge deck components considered in the numerical model suggested in this study, and for the type and arrangement of the applied loading used, the following conclusions can be drawn.

1. The finite element software ABAQUS can predict both the thermal(temperature evolution) and mechanical response(load-deflection response, crack pattern, and damage) of the undamaged and fire-damaged concrete bridge deck.

2. The peak temperature predicted on concrete surface for carbonate and siliceous aggregate is about 82 and 91 ^{o}C respectively. The ultimate load of the concrete bridge deck consists of siliceous aggregate is less than carbonate aggregates with a peak load of 226 and 230 KN respectively. This result indicates aggregate types have little effect on both predicted temperature and ultimate load-carrying capacity of concrete bridge deck subjected to fire.

3. The fire duration significantly influences the predicted temperature of pultruded GFRP and concrete with a peak temperature of about 205 and 165 °C, 346 and 289 °C for 60 and 120 minutes standard fire (ISO 834) respectively. The reduction in ultimate load of the fire-damaged concrete bridge deck had 15 and 19% respectively. This is due to high thermal load resulting in excessive deflection, loss in strength, and stiffness of concrete bridge decks.

4. The effect of fire scenarios becomes more significant on the temperature evolution and fire performance of concrete decks. About 352 and 206 °C maximum temperature was predicted on pultruded GFRP and the concrete surface under hydrocarbon and standard fire respectively. Compared to undamaged fire specimen C1 the reduction in ultimate load of fire-damaged specimen C1 was 13.9 and 17.7 % under standard and hydrocarbon fire respectively.

5. The presence of sustained loading at elevated temperatures does not have a noticeable impact on the pultruded GFRP act as a bottom layer reinforcement and concrete temperature predicted. However, it leads to excessive deflection. Since, as the sustained load increased from 50% to 75% of the ultimate load-carrying capacity and the deflection of the deck increased from 129 to 193.5 KN and 10.3 to 20.5 mm respectively.

6. The peak temperature predicted on pultruded GFRP for 205 and 410mm deck width had about 104 and 103 °C. This indicates that the deck width had a very smaller effect on the predicted temperature evolution of the concrete deck. Specimen C2 with twice the width and GFRP top reinforcement area than specimen C1 had about 54.6% ultimate carrying capacity. The fire-damaged deck reinstates its peak load by 13.1 and 8.61% for specimens C2 and C1 respectively. This is due to concrete confinement as a result of two adjacent T-up ribs and thermal expansion of the GFRP which result in pre-compression of concrete.

7. Extending the GFRP base plate about 475 and 950mm length enhanced the ultimate strength of the fire-damaged concrete deck up to 10.94 and 50.6 % compared to the control specimen SDF. Therefore, further extending the GFRP base plate nearest to supports enhances the flexural response and stiffness of the concrete bridge deck after the fire.

8. The GFRP base plate thickness significantly influences the predicted temperature of pultruded GFRP with a peak temperature of about 136 and 95 °C for 10 and 20 mm GFRP base plate thickness respectively. And enhanced the ultimate load of the fire-damaged concrete bridge deck from 9.09 to 14.65 %. After exposed to fire the GFRP base thickness also reinstates the occurrence of the initiation cracking of fire-damaged concrete deck from cracking load of about 25 to 30 KN.

9. With increase the span to depth ratio of the undamaged concrete deck from 7 to 8 varying the depth of deck; the ultimate load-carrying capacity significantly reduced by 53.3% while varying the length of the deck relatively influence the performance of the deck; that is reduced only by 14.95% while for fire-damaged concrete deck reduced by 48.6 and 14.66% respectively. Therefore, the finding indicates that the effect of span to depth ratio varying with a depth significantly influences the performance of concrete decks.

10. The ultimate load of the concrete bridge deck exposed to fire for the 1-hour heating and cooling phase experienced more ultimate load. The enhanced ultimate load of the fire-damaged concrete bridge deck is about 3.56 and 21 % of the undamaged concrete deck and 2-hour fire-damaged concrete deck without cooling phase respectively. This is due to the thermal heating and cooling of the concrete bridge deck resulting in the pre-compression of concrete.

5.3 Recommendations and future works

During this study, urgent areas of research needed for further investigation on the post-fire performance of GFRP SIP formwork for concrete bridge decks are addressed. Depending on the current work carried out in this study the following areas of research can be recommended for future work.

- In this study, the experimental specimen used for numerical validations used is small-scale testing which cannot fully represent bridge decks in existing structures, which are always subject to vehicular live loads and heavy sustained loads. Further investigation needs on large scale GFRP SIP formwork for concrete bridge deck both experimental and numerical.
- A perfect bond is assumed between concrete and GFRP SIP formwork in this study due to the lack of information on bond-slip between the two materials at

elevated temperatures. Therefore, an experimental investigation is needed on the bond performance of GFRP SIP formwork and concrete.

- Based on parameters investigated in this study; a simple model for evaluating the fire-resistant of GFRP SIP formwork concrete bridge deck which would account for major factors influencing the fire performance of concrete deck exposed to fire must be developed.
- The mechanical properties of GFRP such as compressive, tensile and shear strength above 250 ^{o}C needs further investigation to model the accurate response of composite materials at elevated temperature in finite element.

REFERENCE

ABAQUS. (2020). *ABAQUS Analysis User's Manual 6.20-EF,Dassault Systèmes Simulia Corp.,Providence, RI, USA*.

ACI 318-95. (1995). Building Code Requirements for Structural Concrete (ACI 318-95) and Commentary (ACI 318R-95). In *American Concrete Institute*.

ACI 4401.1R-15. (2015). *ACI 440.1R-15: Guide for the Design and Construction of Structural Concrete Reinforced with FRP Bars*.

Al-Salloum, Y. A., Almusallam, T. H., Elsanadedy, H. M., & Iqbal, R. A. (2016). Effect of elevated temperature environments on the residual axial capacity of RC columns strengthened with different techniques. *Construction and Building Materials*, *115*, 345–361. https://doi.org/10.1016/j.conbuildmat.2016.04.041

Alconpat, R. (2020). *A numerical approach for evaluating residual capacity of fire damaged concrete members*. *10*(2), 230–242.

Alsayed, S., Al-Salloum, Y., Almusallam, T., El-Gamal, S., & Aqel, M. (2012). Performance of glass fiber reinforced polymer bars under elevated temperatures. *Composites Part B: Engineering*, *43*(5), 2265–2271. https://doi.org/10.1016/j.compositesb.2012.01.034

Alshannag, M. J., & Alshenawy, A. (2020). Effective strengthening schemes for heat damaged reinforced concrete beams. *Journal of King Saud University - Engineering Sciences*, *32*(4), 236–245. https://doi.org/10.1016/j.jksues.2019.10.003

Anderberg, Y., & Thelandersson, S. (1976). Stress and deformation characteristics of concrete: experimental investigation and material behaviour model. *University of Lund, Sweden, Bulletin54*, 86.

Annu, & Ahmed, S. (2021). Advanced green materials: An overview. In S. Ahmed (Ed.), *Advanced Green Materials* (pp. 1–13). Woodhead Publishing. https://doi.org/https://doi.org/10.1016/B978-0-12-819988-6.00001-X

ASCE. (1992). *Structural Fire Protectio American Society of Civil Engineering Structural Fire Protection* (Issue 78). American Society of Civil Engineers.

ASTM E1530. (2013). *Standard Test Method for Evaluating the Resistance to Thermal Transmission of Materials by the Guarded Heat Flow Meter Technique 1*. https://doi.org/10.1520/E1530-11.2

Ayman, S., Xin, H., Liu, Y., Mosallam, A. S., He, J., & Du, A. (2017). Evaluation on material behaviors of pultruded glass fiber reinforced polymer (GFRP) laminates. *Composite Structures*. https://doi.org/10.1016/j.compstruct.2017.09.006

Aziz, E., & Kodur, V. (2013). An approach for evaluating the residual strength of fire

exposed bridge girders. *Journal of Constructional Steel Research*, *88*, 34–42. https://doi.org/10.1016/j.jcsr.2013.04.007

Bai, Y., Keller, T., & Vallée, T. (2008). Modeling of stiffness of FRP composites under elevated and high temperatures. *Composites Science and Technology*, *68*(15–16), 3099–3106. https://doi.org/10.1016/j.compscitech.2008.07.005

Bai, Y., Post, N. L., Lesko, J. J., & Keller, T. (2008). Experimental investigations on temperature-dependent thermo-physical and mechanical properties of pultruded GFRP composites. *Elsevier*, *469*, 28–35. https://doi.org/10.1016/j.tca.2008.01.002

Barbero, E. J., Cosso, F. A., Roman, R., Weadon, T. L., & Engineering, A. (2013). Determination of Material Parameters for Abaqus Progressive Damage Analysis of E-Glass Epoxy Laminates. *Journal of Bridge Engineering*, 211–220.

Bellakehal, H., Zaidi, A., Masmoudi, R., & Bouhicha, M. (2014). Behavior of FRP Bars-Reinforced Concrete Slabs under Temperature and Sustained Load Effects. *Polymers, March*, 874–888. https://doi.org/10.3390/polym6030873

Bhuvaneshwari, P., & Mohan, K. S. R. (2020). Strengthening of Fire-Damaged Reinforced Concrete Short Columns Using GFPPECC Composites. *Arabian Journal for Science and Engineering*, *45*(10), 8619–8632. https://doi.org/10.1007/s13369-020-04795-x

Boles, R., Nelson, M., & Fam, A. (2015). Durability of Bridge Deck with FRP Stay-in-Place Structural Forms under Freeze-Thaw Cycles. *Journal of Composites for Construction*, *19*(4), 04014070. https://doi.org/10.1061/(asce)cc.1943-5614.0000531

Cai, B., Li, B., & Fu, F. (2020). Finite Element Analysis and Calculation Method of Residual Flexural Capacity of Post-fire RC Beams. *International Journal of Concrete Structures and Materials*, *14*(1). https://doi.org/10.1186/s40069-020-00428-7

Correia, J. R., Bai, Y., & Keller, T. (2015). A review of the fire behaviour of pultruded GFRP structural profiles for civil engineering applications. *Composite Structures*, *127*, 267–287. https://doi.org/10.1016/j.compstruct.2015.03.006

Correia, J. R., Bai, Y., Keller, T., Gomes, M. M., Pires, J. M., Branco, F. A., Sousa, J. M., Correia, J. R., Cabral-Fonseca, S., & Diogo, A. C. (2015). A review of the fire behaviour of pultruded GFRP structural profiles for civil engineering applications. *Composite Structures*, *116*(1), 267–287. https://doi.org/10.1016/j.compstruct.2015.03.006

Correia, J. R., Gomes, M. M., Pires, J. M., & Branco, F. A. (2013). Mechanical behaviour of pultruded glass fibre reinforced polymer composites at elevated temperature: Experiments and model assessment. *Composite Structures*, *98*, 303–313. https://doi.org/10.1016/j.compstruct.2012.10.051

Dai, J., Gao, W., Teng, J. G., & Asce, M. (2014). Finite Element Modeling of Insulated FRP-Strengthened RC Beams Exposed to Fire. *Journal of Composites for Con-Struction(ASCE)*, 1–15. https://doi.org/10.1061/(ASCE)CC.1943-5614.0000509.

Dassault system. (2012). *Abaqus Analyisis users manual*.

Elbahy, Y. I., Youssef, M. A., & Meshaly, M. (2021). Numerical investigation of reinforced-concrete beam-column joints retrofitted using external superelastic shape memory alloy bars. *Journal of Materials Science*, *8*(July), 716–738. https://doi.org/10.3934/matersci.2021043

Ellis, D. S., Tabatabai, H., & Nabizadeh, A. (2018). Residual tensile strength and bond properties of GFRP bars after exposure to elevated temperatures. *Materials*, *11*(3), 1–14. https://doi.org/10.3390/ma11030346

EN 1991-1-2. (2011). *Eurocode 1: Actions on structures - Part 1-2: General actions - Actions on structures exposed to fire.* (Vol. 1, Issue 2005).

EN 1992-1-1. (2011). *Eurocode 2: Design of concrete structures - Part 1-1: General rules and rules for buildings* (Vol. 1, Issue 2005).

EN 1992-1-2). (2011). *Eurocode 2: Design of concrete structures - Part 1-2: General rules - Structural fire design Eurocode* (Vol. 1, Issue 2005).

Espinos, A., Romero, M. L., & Hospitaler, A. (2010). Advanced model for predicting the fire response of concrete filled tubular columns. *Journal of Constructional Steel Research*, *66*(8–9), 1030–1046. https://doi.org/10.1016/j.jcsr.2010.03.002

fib. (2010). *fib bulletin 55:model code 2010,frist complte draft,volume 1*.

Foster, S. K., Bisby, L. A., & Eng, P. (2008). Fire Survivability of Externally Bonded FRP Strengthening Systems. *ASCE*, *12*(October), 553–561. https://doi.org/10.1061/(ASCE)1090-0268(2008)12:5(553) CE

Garlock, M., Paya-Zaforteza, I., Kodur, V., & Gu, L. (2012). Fire hazard in bridges: Review, assessment and repair strategies. *Engineering Structures*, *35*, 89–98. https://doi.org/10.1016/j.engstruct.2011.11.002

Genikomsou, A. S., & Polak, M. A. (2015). Finite element analysis of punching shear of concrete slabs using damaged plasticity model in ABAQUS. *ENGINEERING STRUCTURES*, *98*, 38–48. https://doi.org/10.1016/j.engstruct.2015.04.016

Ghannam, M. (2019). Proposed models for concrete thermal expansion with different aggregate types and saturation conditions. *SN Applied Sciences*, *1*(5), 1–13. https://doi.org/10.1007/s42452-019-0452-1

Giuliani, L., Crosti, C., & Gentili, F. (2012). Vulnerability of bridges to fire. *Bridge*

Maintenance, Safety, Management, Resilience and Sustainability - Proceedings of the Sixth International Conference on Bridge Maintenance, Safety and Management, May 2014, 1565–1572. https://doi.org/10.1201/b12352-225

Goertzen, W. K., & Kessler, M. R. (2007). Dynamic mechanical analysis of carbon / epoxy composites for structural pipeline repair. *Journal of Composites, 38*, 1–9. https://doi.org/10.1016/j.compositesb.2006.06.002

Gooranorimi, O., Claure, G., De Caso, F., Suaris, W., & Nanni, A. (2018). Post-Fire Behavior of GFRP Bars and GFRP-RC Slabs. *Journal of Materials in Civil Engineering, 30*(3), 04017296. https://doi.org/10.1061/(asce)mt.1943-5533.0002168

Hafezolghorani, M., Hejazi, F., Vaghei, R., Jaafar, M. S. Bin, & Karimzade, K. (2017). Simplified damage plasticity model for concrete. *Structural Engineering International, 27*(1), 68–78. https://doi.org/10.2749/101686616X1081

Hajiloo, H., & Green, M. F. (2018a). Post- fi re residual properties of GFRP reinforced concrete slabs : A holistic investigation. *Composite Structures, 201*(June), 398–413. https://doi.org/10.1016/j.compstruct.2018.06.047

Hajiloo, H., & Green, M. F. (2018b). Post-fire residual properties of GFRP reinforced concrete slabs: A holistic investigation. *Composite Structures, 201*(May), 398–413. https://doi.org/10.1016/j.compstruct.2018.06.047

Hajiloo, H., & Green, M. F. (2019). GFRP reinforced concrete slabs in fire : Finite element modelling. *Engineering Structures, 183*(November 2017), 1109–1120. https://doi.org/10.1016/j.engstruct.2019.01.028

Hashim, A. M., & Kadhum, M. M. (2021). Numerical and experimental study of postfire behavior of concentrically loaded SIFCON columns. *ACI Structural Journal, 118*(1), 73–86. https://doi.org/10.14359/51728078

Hawileh, R. A., & Rasheed, H. A. (2017). Thermal analysis of GFRP-reinforced continuous concrete decks subjected to top fire. *International Journal of Advanced Structural Engineering, 9*(4), 315–323. https://doi.org/10.1007/s40091-017-0168-7

Helmi, A. A. (2019). Prediction of Lateral Confinement Stress for Concrete Filled Steel Tube Column. *Current Trends in Civil & Structural Engineering, 4*(2). https://doi.org/10.33552/ctcse.2019.04.000581

Henderson, J. B., Wiebelt, J. A., & Tant, M. R. (1982). A method for the determination of the specific. *Thermochimica Acta, 57*, 161–171.

Hollaway, L. C. (2010). A review of the present and future utilisation of FRP composites in the civil infrastructure with reference to their important in-service properties.

Construction and Building Materials, *24*(12), 2419–2445. https://doi.org/10.1016/j.conbuildmat.2010.04.062

Hosseini, S. A., Zeinoddini, M., & Darian, A. S. (2014). *Modelling of I-Shaped Beam-to-Tubular Column Connection Subjected to Post-Fire Conditions*. *August 2018*. https://doi.org/10.1007/s13296-014-3008-7

Hussien, N., & Al-thairy, H. (2020). Numerical Study on the Performance of GFRP RC Beams Exposed to High Temperature. *Al-Qadisiyah Journal for Engineering Sciences*, *13*, 136–143. https://doi.org/https://doi.org/10.30772/qjes.v13i2.635

Jadooe, A., Al-Mahaidi, R., & Abdouka, K. (2017). Bond Behavior between NSM CFRP Strips and Concrete Exposed to Elevated Temperature Using Cement-Based and Epoxy Adhesives. *Journal of Composites for Construction*, *21*(5), 04017033. https://doi.org/10.1061/(asce)cc.1943-5614.0000812

Jadooe, A., Al-Mahaidi, R., & Abdouka, K. (2018). Behaviour of heat-damaged partially-insulated RC beams using NSM systems. *Construction and Building Materials*, *180*, 211–228. https://doi.org/10.1016/j.conbuildmat.2018.05.279

Kai, X., Guo-hui, W., Ting, Z., & Zhou-dao, L. U. (2011). Experiment and Analysis of CFRP Strengthened Fire-damaged Reinforced Concrete Continuous T-Beams. *Sciencedirect*, *11*, 541–549. https://doi.org/10.1016/j.proeng.2011.04.694

Karadeniz, Z. H., & Kumlutas, D. (2007). A numerical study on the coefficients of thermal expansion of fiber reinforced composite materials. *Journal of Composites Structures*, *78*, 1–10. https://doi.org/10.1016/j.compstruct.2005.11.034

Keller, B. and. (2009). Modeling of Strength Degradation for Fiber-reinforced Polymer Composites in Fire. *Journal of Composites Materials*, *43*(21). https://doi.org/10.1177/0021998309344642

Keller, T., Tracy, C., & Zhou, A. (2006a). Structural response of liquid-cooled GFRP slabs subjected to fire – Part I : Material and post-fire modeling. *Journal of Composites*, *37*, 1286–1295. https://doi.org/10.1016/j.compositesa.2005.08.006

Keller, T., Tracy, C., & Zhou, A. (2006b). *Structural response of liquid-cooled GFRP slabs subjected to fire – Part I : Material and post-fire modeling*. *37*, 1286–1295. https://doi.org/10.1016/j.compositesa.2005.08.006

Keller, T., Zhou, A., Tracy, C., Hugi, E., & Schnewlin, P. (2005). Experimental study on the concept of liquid cooling for improving fire resistance of FRP structures for construction. *Journal of Composites for Construction*, *36*, 1569–1580. https://doi.org/10.1016/j.compositesa.2004.10.032

Ki-Yeol Shin, S.-B. K. (1999). *Thermophysical Properties and Transient Heat Transfer of Concrete at elevated temperature*. *212*, 233–241.

Kodur, K. R., Dwaikat, M. M. S., & Dwaikat, M. B. (2009). High-temperature properties of concrete for fire resistance modeling of structures. *ACI Materials Journal*, *106*(4), 390.

Kodur, V. (2014a). Properties of concrete at elevated temperatures. *ISRN Civil Engineering*, *2014*. https://doi.org/10.1155/2014/468510

Kodur, V. (2014b). Properties of concrete at elevated temperatures. *ISRN Civil Engineering*, *2014*, 1–15. https://doi.org/10.1155/2014/468510

Kodur, V. K. R., Wang, T. C., & Cheng, F. P. (2004). Predicting the fire resistance behaviour of high strength concrete columns. *Cement and Concrete Composite*, *26*, 141–153. https://doi.org/10.1016/S0958-9465(03)00089-1

Kong, F. K., & Kaplan, M. F. (1991). Concrete at High Temperatures : In *Concrete Design and Construction Series SERIES*.

Krishna, D., Infante, V., & Krishna, D. (2019a). Effect of Elevated Temperatures on the Mechanical Properties of Concrete. *Procedia Structural Integrity*, *14*, 384–394. https://doi.org/10.1016/j.prostr.2019.05.047

Krishna, D., Infante, V., & Krishna, D. (2019b). ScienceDirect ScienceDirect ScienceDirect Effect of Elevated Temperatures on the Mechanical Properties of Concrete Thermo-mechanical modeling of a high turbine Effect of Elevated on the Mechanical of an Anupama Temperatures R pressure * blade of airplane . *Procedia Structural Integrity*, *14*, 384–394. https://doi.org/10.1016/j.prostr.2019.05.047

Lapczyk, I., & Hurtado, J. A. (2007). Progressive damage modeling in fiber-reinforced materials. *Journal of Composites*, *38*, 2333–2341. https://doi.org/10.1016/j.compositesa.2007.01.017

Lennon, T., Moore, D. B., Wang, Y. C., & Bailey, C. G. (2007). *Designers ' guide to EN1991-1-2, EN1992-1-2, 1993-1-2 and 1994-1-2, Handbook for the fire design of steel, composite and concrete structures to the eurocodes*.

Lenwari, A., Thongchom, C., & Aboutaha, R. S. (2020). *Cyclic Flexural Performance of Fire-Damaged Reinforced Concrete Beams Strengthened with Carbon Fiber-Reinforced Polymer Plates*. *117*. https://doi.org/10.14359/51728064

Li, M., Qian, C. X., & Sun, W. (2004). Mechanical properties of high-strength concrete after fire. *Cement and Concrete Research*, *34*(6), 1001–1005. https://doi.org/10.1016/j.cemconres.2003.11.007

Liao, F., & Huang, Z. (2018). Modeling Cracks of Reinforced Concrete Slabs under Fire

Conditions. *Journal of Structural Engineering*, *144*(5), 04018030. https://doi.org/10.1061/(asce)st.1943-541x.0001996

Madandoust, R., Kazemi, M., & Moghadam, S. Y. (2017). Analytical study on tensile strength of concrete. *Revista Romana de Materiale*, *2*(2), 204–209.

Mago, N., Hicks, S., & Simms, W. I. (2014). Sequentially coupled thermal-stress analysis of a new steel-concrete composite slab under fire. *2014 SIMULIA Customer Conference, January 2015*. https://doi.org/10.13140/RG.2.2.26406.93763

Martinez, J., & Jeffers, A. E. (2018). Elevated-Temperature Tension Stiffening Model for Reinforced Concrete Structures under Fire. *The 10th International Conference on Structures in Fire SIF'18, June 2018*, 463–470. http://www.structuresinfire.com/corpo/conferences/sif18.pdf

Morgado, T., Correia, J. R., Silvestre, N., & Branco, F. A. (2018). Experimental study on the fire resistance of GFRP pultruded tubular beams. *Composites Part B: Engineering*, *139*, 106–116. https://doi.org/10.1016/j.compositesb.2017.11.036

Morgado, T., Silvestre, N., & Correia, J. R. (2018). Simulation of fire resistance behaviour of pultruded GFRP beams – Part I: Models description and kinematic issues. *Composite Structures*, *187*, 269–280. https://doi.org/10.1016/j.compstruct.2017.12.063

Nayal, R., & Rasheed, H. A. (2006). Tension stiffening model for concrete beams reinforced with steel and FRP bars. *Journal of Materials in Civil Engineering*, *18*, 831–841. https://doi.org/DOI:10.1061/(ASCE)0899-1561(2006)18:6(831)

Nelson, M., & Fam, A. (2013). Structural GFRP Permanent Forms with T-Shape Ribs for Bridge Decks Supported by Precast Concrete Girders. *Journal of Bridge Engineering*, *18*(9), 813–826. https://doi.org/10.1061/(asce)be.1943-5592.0000418

Nelson, M., & Fam, A. (2014). Full bridge testing at scale constructed with novel FRP stay-in-place structural forms for concrete deck. *Construction and Building Materials*, *50*, 368–376. https://doi.org/10.1016/j.conbuildmat.2013.09.056

Nelson, M. S., Fam, A. Z., Busel, J. P., Bakis, C. E., Nanni, A., Bank, L. C., Henderson, M., & Hanus, J. (2014). Fiber-reinforced polymer stay-in-place structural forms for concrete bridge decks: State-of-the-art review. *ACI Structural Journal*, *111*(5), 1069–1080. https://doi.org/10.14359/51686810

Nicoletta, B., Woods, J., Gales, J., & Fam, A. (2019). Postfire Performance of GFRP Stay-in-Place Formwork for Concrete Bridge Decks. *Journal of Composites for Construction*, *23*(3), 04019015. https://doi.org/10.1061/(asce)cc.1943-5614.0000941

Othuman Mydin, M. A., & Wang, Y. C. (2012). Thermal and mechanical properties of

lightweight foamed concrete at elevated temperatures. *Magazine of Concrete Research*, *64*(3), 213–224. https://doi.org/10.1680/macr.10.00162

Ou, Y., & Zhu, D. (2015). Tensile behavior of glass fiber reinforced composite at different strain rates and temperatures. *Construction and Building Materials*, *96*, 648–656. https://doi.org/10.1016/j.conbuildmat.2015.08.044

Papanikolaou, V. K., & Kappos, A. J. (2007). Confinement-sensitive plasticity constitutive model for concrete in triaxial compression. *International Journal of Solids and Structures*, *44*, 7021–7048. https://doi.org/10.1016/j.ijsolstr.2007.03.022

Peris-Sayol, G., Paya-Zaforteza, I., Balasch-Parisi, S., & Alós-Moya, J. (2017). Detailed Analysis of the Causes of Bridge Fires and Their Associated Damage Levels. *Journal of Performance of Constructed Facilities*, *31*(3), 04016108. https://doi.org/10.1061/(asce)cf.1943-5509.0000977

Poudel and yadav. (2021). Study of Crack Pattern in RCC Beam Using ABAQUS. *Saudi Journal of Civil Engineering*, *2657*, 116–123. https://doi.org/10.36348/sjce.2021.v05i05.003

R. Ian Gilbert and Robert F. Warner. (1978). Tension Stiffening in Reinforced Concrete Slabs. *American Society of Civil Engineers*, *Vol. 104*(Issue 12). https://doi.org/https://doi.org/10.1061/JSDEAG.0005054

R.M. Jones. (1999). *Mechanics of Composite Materials* (2nd edition (ed.)). Taylor & Francis,.

Raza, A., Khan, Q. U. Z., & Ahmad, A. (2019). Numerical investigation of load-carrying capacity of GFRP-reinforced rectangular concrete members using CDP model in abaqus. *Advances in Civil Engineering*, *2019*. https://doi.org/10.1155/2019/1745341

Reshma Merin Roy, & Jeena B Edayadiyil. (2016). Transient Thermal Analysis of Steel, CFRP GFRP Reinforced Beams. *International Journal of Engineering Research And*, *V5*(07), 454–456. https://doi.org/10.17577/ijertv5is070389

Saafi, M. (2002). Effect of fire on FRP reinforced concrete members. *Composite Structures*, *58*, 11–20.

Sandberg, M., Yuksel, O., Comminal, R. B., Sonne, M. R., Jabbari, M., Larsen, M., Salling, F. B., Baran, I., Spangenberg, J., & Hattel, J. H. (2020). Numerical modeling of the mechanics of pultrusion. *Mechanics of Materials in Modern Manufacturing Methods and Processing Techniques*, 173–195. https://doi.org/10.1016/b978-0-12-818232-1.00006-0

Schmidt, D. G., & d'Almeida, J. R. M. (2018). Effect of Temperature Exposure on the

Flexural Mechanical Behavior of Two Pultruded Composites. *Fire Technology*, *54*(6), 1565–1583. https://doi.org/10.1007/s10694-018-0754-7

Schneider, U. (1988). Concrete at high temperatures - A general review. *Fire Safety Journal*, *13*(1), 55–68. https://doi.org/10.1016/0379-7112(88)90033-1

Sideris, K. K. (2007). Mechanical Characteristics of Self-Consolidating Concretes Exposed to Elevated Temperatures. *Journal of Materials in Civil Engineering*, *19*(8), 648–654. https://doi.org/10.1061/(asce)0899-1561(2007)19:8(648)

Sidney Mindess and J. Francis Young, D. D. (2003). Concrete SECOND EDITION. In *Pearson Education, Inc. Upper Saddle River, NJ 07458* (Vol. 1, Issue, pp. 1–476).

Sousa, J. M., Correia, J. R., Cabral-Fonseca, S., & Diogo, A. C. (2014). Effects of thermal cycles on the mechanical response of pultruded GFRP profiles used in civil engineering applications. *Composite Structures*, *116*(1), 720–731. https://doi.org/10.1016/j.compstruct.2014.06.008

Talebi, H. R., Kayan, B. A., Asadi, I., & Hassan, Z. F. B. A. (2020). Investigation of thermal properties of normal weight concrete for different strength classes. *Journal of Environmental Treatment Techniques*, *8*(3), 908–914.

Tang, W. C., & Lo, T. Y. (2009). Mechanical and fracture properties of normal-and high-strength concretes with fly ash after exposure to high temperatures. *Magazine of Concrete Research*, *61*(5), 323–330. https://doi.org/10.1680/macr.2008.00084

Thomas, K., & Yu, B. (2007). Modeling of thermo-physical properties for FRP composites under elevated and high temperature. *Composite Science and Technology*, *67*, 3098–3109. https://doi.org/10.1016/j.compscitech.2007.04.019

Thongchom, C., Lenwari, A., & Aboutaha, R. S. (2019). Effect of Sustained Service Loading on Post-Fire Flexural Response of Reinforced Concrete T-Beams Tested beams. *ACI Structural Journal*, *116*, 243–254. https://doi.org/10.14359/51714477

Tracy, C. D. (2005). *fire endurance of multicellular panels in an frp building system* (Vol. 3235).

Wahalathantri, B. L., Thambiratnam, D. P., Chan, T. H. T., & Fawzia, S. (2021). A Material Model for Flexural Crack Simulation in Reinforced Concrete Elements using Abaqus. *In Proceedings of the First International Confer- Ence on Engineering, Designing AndDeveloping the Built Environment for SustainableWellbeing, Queensland University of Technology, Queensland University of Technology, Brisbane, Qld, Pp. 260-264. This*, *2657*(June 2015), 260–264. https://doi.org/10.36348/sjce.2021.v05i05.003

Wahid, N., & Bisby, L. A. (2019). High temperature modelling of reinforced concrete flat

slabs calibration of concrete damage plasticity model parameters for high temperature modelling of. *Applications of Structural Fire Engineering*, *June*.

Xin, H., Mosallam, A., Liu, Y., Wang, C., & Zhang, Y. (2017). Analytical and experimental evaluation of flexural behavior of FRP pultruded composite profiles for bridge deck structural design. *Construction and Building Materials*, *150*, 123–149. https://doi.org/10.1016/j.conbuildmat.2017.05.212

Xu, L., Wang, M. T., Bao, Y. H., & Wang, W. Da. (2017). Numerical analysis on structural behaviors of concrete filled steel tube reinforced concrete (CFSTRC) columns subjected to 3-side fire. *International Journal of Steel Structures*, *17*(4), 1515–1528. https://doi.org/10.1007/s13296-017-1219-4

Yaqub, M., Bailey, C. G., Nedwell, P., Khan, Q. U. Z., & Javed, I. (2013). Strength and stiffness of post-heated columns repaired with ferrocement and fibre reinforced polymer jackets. *Composites Part B: Engineering*, *44*(1), 200–211. https://doi.org/10.1016/j.compositesb.2012.05.041

Yimer, m. a. (2019). *Finite Element Investigation of Reinforced Concrete and Steel Fiber Reinforced Concrete Exterior Beam-Column Joints Under Cyclic Loading a Master ' s thesis*,Addis Ababa Science and Technology University.

Yu, B., & Kodur, V. K. R. (2013). Factors governing the fire response of concrete beams reinforced with FRP rebars. *Journal of Composites Structures*, *100*, 257–269. https://doi.org/10.1016/j.compstruct.2012.12.028

Z. Hashin. (2016). Failure Criteria for Unidirectional Fiber Composite. *Journal of Applied Mechanics*, *47*(June 1980), 329–334.